



TECHNISCHE  
UNIVERSITÄT  
WIEN

Vienna University of Technology

MASTER THESIS

# **Experiments and simulation of piezoceramic transducers for a new FTIR testing probe**

ausgeführt zum Zwecke der Erlangung des akademischen Grades eines Diplom-Ingenieurs  
unter der Leitung von

Ass.Prof. Dipl.-Ing. Dr.techn. Michael Harasek

und

Dr. Stefan Radel

E166

Institut für Verfahrenstechnik, Umwelttechnik und Technische Biowissenschaften

der

Technischen Universität Wien

eingereicht an der Technischen Universität Wien

**Fakultät für Maschinenwesen und Betriebswissenschaften**

von

Diana Viktoria Strutzenberger, B.Sc.

Matr. Nr.: 0925732

Pernerstorferweg 16, 2392 Sulz/ Stangau

Wien, am 18.02.2016

## Abstract

For many processes it is a big advantage to be able to do a real-time online and/or inline qualitative analysis of particles during the procedure. Examples include bioprocesses as fermentation or crystallisation processes. For bioprocesses, qualitative analysis of microorganisms provides information used to optimize monitoring and controlling. For this purpose a new ATR (attenuated total reflection) FTIR testing probe was developed. Ultrasound is used for particle manipulation, FTIR spectroscopy for analysis. In the host liquid the particles are entrained by the flow and caught in the nodal plains of a standing ultrasonic wave as soon as they pass the probe's gateway. After the FTIR spectroscopy is finished the particles are set free to continue participating in the process. As transducer a piezoceramic disc is used and built into the probe's head. The three parts of this thesis deal with vibration analysis of the piezoceramic element and the review of FEM models built in *ANSYS Workbench*. To get an idea of the discs' oscillation behaviour their vibration modes and maxima of displacement are measured using a vibrometer. In the last part of the thesis possible ways to evaluate a significant FEM model of the testing probe are presented. The model consists of the fundamental parts of the probe. In *ANSYS Workbench* the complex acoustic admittance is calculated and prepared for comparison. Further the measurement of the complex electric admittance is performed under laboratory conditions. Both, measurement of the electric admittance and the simulation of the acoustic admittance are done for the same frequency range with similar variations in the size of the fluid body and its composition. For validation of the FEM model further investigation may include a corresponding simulation of the electric admittance and the measurement of the acoustic admittance respectively. Those results could be compared and discussed in future works using the basis described in this thesis. Eventually these models should provide most realistic results to be able to predict consequences of parameter modification for future development. At a later stage, they shall be used to predict the probe's performance under different process conditions. The results of the measurements and the simulation for the single piezoelectric disc are compared and show several compliances. Further detailing of the simulation model could be part of future works as well as the finalisation of the last part of this thesis.

## Kurzfassung

Für verschiedene verfahrenstechnische Anwendungen ist es von Vorteil, eine möglichst zeitnahe Online- bzw. Inline-Messmethode für die qualitative Analyse von Partikeln zur Verfügung zu haben. Beispiele hierfür sind bioverfahrenstechnische Prozesse wie Fermentation oder Kristallisationsverfahren. Bei Bioprozessen liefert die qualitative Analyse von Mikroorganismen Informationen, mit deren Hilfe der Prozess nach Bedarf überwacht und geregelt werden kann. Für diesen Zweck wurde ein neues Modell einer ATR-Sonde entwickelt. Es werden Ultraschall für die Partikelmanipulation und FTIR-Spektroskopie für die Analyse eingesetzt. Die Partikel strömen mit dem jeweiligen Prozessmedium mit und werden durch den Ultraschall in den Knotenebenen der stehenden Welle im Kanal der Sonde gefangen. Sobald die IR-Analyse abgeschlossen ist, können die Partikel wieder an das Medium freigelassen werden und weiter am Prozess teilnehmen. Als Schallgeber dient ein Piezoelement in Form einer Scheibe, die in die Sonde eingebaut ist. Die drei Teile dieser Arbeit beschäftigen sich mit der Schwingungsanalyse des Piezoelements und mit der Bewertung von FEM-Modellen, die mit *ANSYS Workbench* erstellt werden. Mithilfe eines Vibrometers werden die Piezoscheiben auf ihre Schwingungsmodi und Momentanwerte untersucht. Der letzte Teil der Arbeit behandelt mögliche Varianten für die Bewertung eines FEM-Modells einer kompletten Messsonde. Dieses Modell umfasst die wichtigsten Teile der Sonde. Mithilfe von *ANSYS Workbench* wird die komplexe akustische Admittanz berechnet und für Vergleiche vorbereitet. Weiters wird die komplexe elektrische Admittanz unter Laborbedingungen gemessen. Die Simulation der akustischen Admittanz und die Messung der elektrischen Admittanz werden beide für den gleichen Frequenzbereich mit verschiedenen Variationen in der Höhe des Fluids und dessen Zusammensetzung durchgeführt. Für die Validierung des Modells können zukünftige Untersuchungen Simulationen für die elektrische Admittanz bzw. Messungen der akustischen Admittanz umfassen. Diese Ergebnisse können in Zukunft mithilfe der Grundlage, die in dieser Arbeit präsentiert wird, evaluiert werden. Die FEM-Modelle sollten möglichst realitätsnahe Berechnungsergebnisse liefern und dazu genutzt werden, das Verhalten der Sonde und Auswirkungen von Parameteränderungen für weitere Entwicklungsschritte vorherzusagen. Die Ergebnisse der Messung für die einzelnen Schwingungsgeber zeigen Übereinstimmungen mit der Simulationen. Eine detailliertere Ausarbeitung des Modells kann das Thema zukünftiger Arbeiten sein, ebenso wie die Fertigstellung der letzten Teils dieser Arbeit.

# Table of contents

<b>Abstract</b> .....	<b>i</b>
<b>Kurzfassung</b> .....	<b>ii</b>
<b>Table of contents</b> .....	<b>iii</b>
<b>Abbreviations</b> .....	<b>v</b>
<b>1 Motivation</b> .....	<b>1</b>
1.1 Ultrasound in industry .....	2
1.2 Infrared spectroscopy in industry .....	5
1.3 Applications for an ultrasound enhanced vibrational spectroscopy probe.....	6
<b>2 Scope of work</b> .....	<b>8</b>
<b>3 Fundamentals</b> .....	<b>9</b>
3.1 Sound waves and ultrasonic particle manipulation .....	9
3.2 Electric admittance .....	14
3.3 ATR FTIR spectroscopy .....	15
3.4 Piezoelectric effect and ultrasonic transducer .....	15
<b>4 Materials and methods</b> .....	<b>19</b>
4.1 Vibrometer measurements.....	19
4.2 Stand for vibrometer measurements.....	21
4.3 Finite Element Method (FEM).....	23
4.4 Piezoceramic elements .....	27
4.5 Testing probe prototype .....	29
<b>5 Experimental</b> .....	<b>31</b>
5.1 Modal analysis of a single piezoceramic disc.....	31
5.1.1 Measurement.....	31
5.1.2 FEM simulation of the piezoelectric ceramic.....	38
5.1.3 Comparison of the experimental results and FEM simulation of the modal analysis of a single piezoelectric disc.....	47
5.2 Instantaneous values at individual surface points of a single piezoceramic disc .....	52
5.2.1 Measurement.....	52
5.2.2 Simulation .....	54

5.2.3 Results .....56

5.3 Possible ways for evaluation of a significant FEM model of the testing probe .....62

5.3.1 Proposal for measurement .....63

5.3.2 Proposal for simulation .....69

**6 Summary and Conclusion..... 76**

**7 Perspective ..... 78**

**References.....80**

**Appendix.....84**

## Abbreviations

$\alpha$	phase angle of oscillating disc	°
$\Delta\alpha$	phase shift	°
$\epsilon^S$	permittivity at constant strain	F/m
$\theta_i$	angle of incident sound wave	°
$\theta_r$	angle of reflected sound wave	°
$\theta_t$	angle of transmitted sound wave	°
$\lambda$	wave length	m
$\rho$	density	kg/m <sup>3</sup>
$\varphi$	velocity potential	m <sup>2</sup> /s
$X$	ratio of two deflections	-
$\omega$	angular frequency	1/s
$\theta$	incident angle of sound wave	°
$A$	instantaneous value	m/s
$B_a$	acoustic susceptance	m/Pa.s
$B_e$	electric susceptance	S
$c$	speed of sound or sound speed	m/s
$c^E$	stiffness or anisotropic elasticity at constant electric field	Pa
$D$	electric flux density	A.s/m <sup>2</sup>
$d$	piezoelectric charge coefficient	m/V
$E$	electric field	V/m
$e$	piezoelectric matrix relating stress/electric field	N/V.m
$f$	frequency	Hz
$f_s$	series resonance frequency	Hz
$G_a$	acoustic conductance	m/Pa.s
$G_e$	electric conductance	S
$N_p$	frequency coefficient of planar oscillation	Hz.m

$N_t$	frequency coefficient of thickness oscillation	Hz.m
$OD$	diameter of piezoceramic disc	m
$p$	sound pressure	Pa
$P_i$	pressure of incident sound wave	Pa
$P_r$	pressure of reflected sound wave	Pa
$P_t$	pressure of transmitted sound wave	Pa
$R_c$	reflection coefficient	-
$R_a$	acoustic resistance	Pa.s/m
$R_e$	electric resistance	$\Omega$
$S$	mechanical strain	-
$s^E$	compliance or elasticity coefficient at constant electric field	m <sup>2</sup> /N
$T$	mechanical stress	N/m <sup>2</sup>
$T_c$	transmission coefficient	-
$TH$	thickness of piezoceramic disc	m
$u$	sound variable for pressure or velocity	Pa or m/s
$v$	sound particle velocity	m/s
$v_s$	velocity of surface	m/s
$X_a$	acoustic reactance	Pa.s/m
$X_e$	electric reactance	$\Omega$
$Y_a$	acoustic admittance	m/Pa.s
$Y_e$	electric admittance	S
$Z_a$	acoustic impedance	Pa.s/m
$Z_e$	electric impedance	$\Omega$

# 1 Motivation

In the field of bioprocesses new innovative analytical methods for process monitoring are in demand. Those need to correlate with requirements such as reliability and speed. Measurements for process monitoring often cost too much time to enable efficient intervention. This leads to insufficient product quality or increased discard. Due to their direct integration into the facility inline measurement methods provide potential for development. Inline measurements enable direct and real-time data acquisition. Process control systems can access process data without time delay and initiate appropriate measures.

This work is part in the advancement of a new ultrasound enhanced vibrational spectroscopy probe developed by Markus Brandstetter, Bernhard Lendl and Stefan Radel. [1, 2] It allows to perform ATR FTIR spectroscopy on particles in a flowing medium by trapping them with an ultrasonic standing wave. This innovative procedure shows high economic potential as it decreases discard and response time of process control in industry.

The testing probe consists of an ultrasonic transducer and a measurement system for Fourier Transform Infrared (FTIR) spectroscopy. For example the progress in bioreactors can be found by observing the current state of cells or microorganisms which are being processed. As analysing method attenuated total reflection FTIR spectroscopy is applied. This method implies the ability to hold samples in a certain range. Particles, microorganisms or cells dispersed in a moving medium need to be trapped during measurement time without disturbance of their characteristics. Ultrasonic particle manipulation proved to be an adequate solution for this task. An ultrasonic transducer emits ultrasonic waves into the process medium. The waves are reflected and form a standing wave with nodal and anti-nodal planes. The particles are trapped in the nodal planes and can be manipulated by modifying the wavelength. It is the first time this procedure is dealt with this explicitly in combination of measurements and FEM simulation. The simulation provides the opportunity to develop a model as realistic as possible that can be used for the calculation of different application cases under various conditions. A significant FEM model of the testing probe would provide advantages in the optimisation of design and operational performance.

This method for particle manipulation can also be applied for other analysis methods as microscopy and determination of index of refraction. Below industrial applications of ultrasound and IR spectroscopy as well as the finalised testing probe are discussed.

## 1.1 Ultrasound in industry

For chemical engineering processes economy and sustainability are values which are gaining importance increasingly. Production companies not only have to customize their process cycles but are also in need of monitoring and controlling facilities to stay competitive. Leonelli et al. [3] explains in his work, that the development of new process technologies is, for example, motivated by the goal to achieve environmentally friendlier production in chemical industry. This leads to rising requirements for industrial sensors and measuring systems. Ultrasound measurements offer a wide range of applications and are used for measuring filling levels, flow rate, concentration, density and mass flow rate. [4] Ultrasound cannot only be used for analysis but also to influence technical processes directly. As mentioned by Cai et al. [5] ultrasound can be used for various technical applications and processes as drying, cleaning and degassing. Especially sonochemistry plays an important role and needs to be mentioned here.

**Table 1: Examples for technical applications of ultrasound [6]**

<b>Applications</b>	<b>Examples</b>
Machining of Materials	Welding, cutting, soldering
Cleaning	General surface cleaning, washing of soil and ores
Homogenisation/Spraying	Emulsification and atomisation of liquids
Separation	Crystallisation, filtration
Water treatment	Removal of chemical and biological pollution
Biological uses	Cell disruption
Medical uses	Dental descaling, scalpels, nebulisers

Sonochemistry deals with effects of ultrasound on chemical reactions and processes. It describes how sound is used to activate certain chemical reactions- as it is possible with temperature or light. In order to come into action the sound waves have to be able to propagate through the medium which also applies for liquids. [6] Since the 1960s this topic has been researched intensively. Ultrasonic cleaning baths and cell disruptors started to appear in laboratories.

Modern fields of development in sonochemistry are synthesis, electrochemistry, materials and medical applications such as the treatment of cancer. In food technology it supports procedures like freezing, drying, mixing and homogenisation but also cooking and frying. Most of these effects base on the same physical phenomenon- cavitation. [3, 7]

Cavitation describes the creation and collapse of vapour bubbles when exposed to instantaneous negative pressure. [8] This creates high-powered shock waves and so-called microjets which can cause- when close to solid surfaces- serious material damage. Whether the shock waves or the microjets alone are the cause of such damage has been discussed for a while. The collapse of a single bubble can lead to a microjet and the creation of more smaller bubbles which would continue the reaction. [9] Some papers discuss the use of cavitation for membrane cleaning in filtration processes. [5, 10–14] Dealing with this technique one will encounter the problem of fouling. It has been recognised as a massive issue for separation processes. [11] Other methods using chemical reagents are described as being time consuming, unsafe or expensive by Maaskooki et al. [15] Here ultrasound offers a non-destructive, hazard-free method for cleaning but also for monitoring and controlling membrane fouling. [11, 12] Li et al. [16] examined the effectiveness of three different cleaning procedures on microfiltration membranes used for wastewater reclamation. They compared ultrasonic cleaning, forwardflushing and the two combined. Online ultrasonic irradiation alone would be too cost intensive with low efficiency. Temperature and viscosity can decrease the effect of cavitation. The combination of ultrasound and flushing showed the most promising results. Another research on ultrasound as a supporting cleaning method was done by Loderer et al. [17] with less impressive results concerning the impact of ultrasound. A new way to clean membranes using sound waves is introduced by Krinks et al. [18]. Instead of an external device for sound generation a piezoelectric membrane is produced. The drawbacks of common cleaning techniques like chemical cleaning are replaced by a self-cleaning PZT membrane. They point out that a lot more needs to be done in this field like performance optimisation and production cost analysis. Some further examples for applications of ultrasound in industry are extraction, crystallisation and particle manipulation.

Compared to common techniques ultrasound helps to extract solvents of natural products like essential oils, sugars, and acids much quicker and with higher yield. Microjets and intense turbulence caused fractures in cell walls and enabled easy access to the inner parts. As described by Shirsath et al. [19] due to difficult requirements on this process up-scaling turns out to be challenging. Besides finding suitable configurations for the reactor, parameters like temperature and solvent type have to be optimised.

Physical properties of the solvent like viscosity and surface tension highly influence the result. Again ultrasound combined with another extracting method proves to be an economical alternative. [19]

In crystallisation processes ultrasound is a common tool to control factors like crystal size and morphology. Primarily, important are the improved reproducibility of results and improving the yield. Further it is possible to control agglomeration and crystal size distribution. [20] The size distribution - especially the percentage of smaller particles- plays an important role for processes including solid-liquid separation and drying. [21] Narducci et al. [22] applied ultrasound irradiation during continuous cooling crystallisation. This quickly led to uniform values in the particle size distribution. [22] Louhikultanen, Karjalainen et al. [21] mention that ultrasound can be applied to raise the crystallisation point to higher temperatures.

In this thesis the last example for application of ultrasound in industrial environment is particle manipulation. Mracek et al. [23] suggested a powder feeding device actuated by a piezoelectric actuator. It is an acrylic pipe which forwards the powder through oscillations as seen in Figure 1.

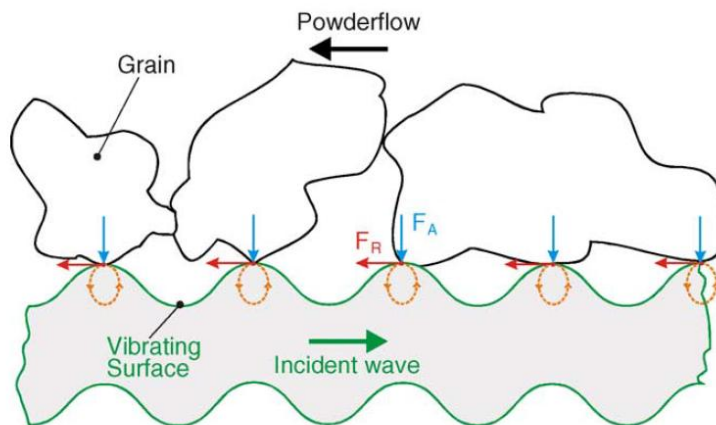


**Figure 1: Force and movement scheme of vibrating pipe and particles [23]**

It proved to be an accurate method for powder feeding even for very small amounts. For loose material transport vibrating surfaces or lines are used frequently. This shall serve as an example for indirect action of ultrasound. A more immediate way is particle manipulation by acoustic radiation forces. [24]

Noncontact manipulating techniques are crucial for micromachine technology, biotechnology and some more fields as stated by Kozuka et al. [25] Particles suspended in a liquid are caught in nodal planes of a standing ultrasonic wave or simply controlled in movement. This principle is used for ultrasonic separators as Benes et al. [26] describe them. This acoustic trapping is a gentle way to hold cells and other sensitive particles. Another practical application is the h-shape resonator (Figure 2). It separates areas of high particle concentration from areas with a lower quantity.

There are several advantages in using this kind of separator for example in bioreactors. The cells do not have to go through a more invasive treatment demanding higher pressures and therefore risking ruptures in the cell walls. [27] This way the intervention is kept in moderate boundaries. There will be a more accurate explanation given in the following chapters.

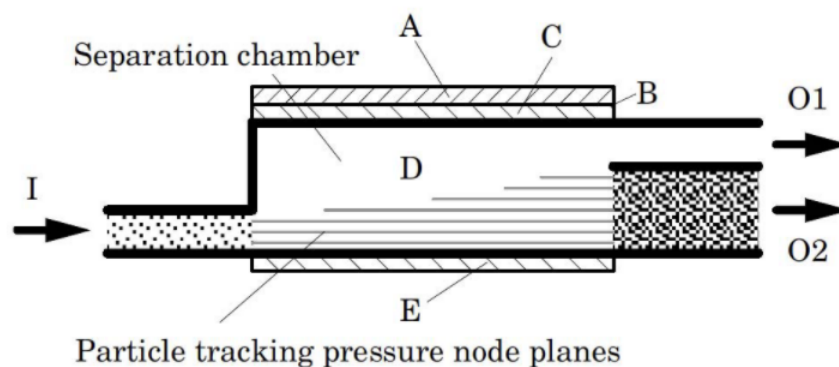


Figure 2: Scheme of an h-shape resonator, PZT transducer (A), Glue (B), glass carriers (C,E), filtrate outlet (O1), retentate outlet (O2) [27]

## 1.2 Infrared spectroscopy in industry

IR spectroscopy will only be treated shortly in this chapter as the focus of the analysis and simulation lies on the piezoelectric transducer and ultrasonic waves.

This analysing method is often used in food industry. The standards in food production have increased heavily. People pay more attention to their health and therefore are more aware of their nutrition. The industry has to adapt to these high standards and improve its controlling system. [28] To keep the good quality in production lines on the same level a non-destructive qualitative and quantitative analysing method is needed. Hashimoto et al. [29] survey FTIR spectroscopy for quantitative inspection- even for the development of a tasting robot. In wine production FTIR spectroscopy is applied for the determination of ingredients. [30, 31]

Not for tasting but for quality control IR spectroscopy is used to determine if the analysed sample of crops is contaminated by fungus. [32] Another paper discussing IR spectroscopy as a tool to detect contamination is done by Petryk et al. [33] Here applications for more hazardous substances are researched and divided into in situ and "standoff detection".

Interesting and yet partially unclear processes are found on solid/liquid interfaces and solid/liquid/gas interfaces in electrochemistry and heterogeneous catalysis. FTIR spectroscopy is used to investigate those processes. Anderson, Baiker et al. [34] describe ATR FTIR spectroscopy as suitable for in situ analysis of solid/liquid and solid/liquid/gas interfaces. Combined with an ATR cell the measuring unit can touch the medium directly. This is also the case for the probe described in this work.

Most important for this thesis and the final example given here is the application in cytology and cell research. FTIR spectroscopy is widely used for analysing single cells. Advantages are simple sample preparation, direct access to information and imaging of cells. The methods find increasing usage in food production and healthcare. Additional newer areas would be bioprocessing and biopharmaceuticals. [35]

### **1.3 Applications for an ultrasound enhanced vibrational spectroscopy probe**

The testing probe discussed here was developed by Markus Brandstetter, Bernhard Lendl and Stefan Radel. The main application intended is monitoring and controlling of bioprocesses. The probe enables in-line and on-line measurement. The cells can be examined during the process which enables quasi real-time analysis of their current state. ATR FTIR spectroscopy provides molecular specific information. [2] For the measurement the cells are fixed and held in single-layer aggregations by an ultrasonic standing wave (Figure 6). [2, 35] Depending on the adjusted wavelength particles can be moved axial in direction of sound propagation. As mentioned by Radel et al. [2] the probe is able to clean itself and prevent biofouling. As tests with different types of particles and liquids have shown there are many possibilities for usage. It presents a good possibility to analyse living cells without causing damage or changes of chemical attributes. Another application could be monitoring of crystallisation processes. Crystal growth can be adapted so that optimal yeast and quality are achieved.

The pressure on industries increases regarding requirements for production yield and quality. For processes in chemical engineering, especially biochemical engineering, it is of great importance to know about the exact status of the reactants, cells, etc. to react early enough and prevent losses. Therefore the ultrasound enhanced vibrational spectroscopy probe offers several advantages [2]:

- In-situ and quasi real-time measurements
- Insensitive for fouling effects
- FTIR spectroscopy for specific information about the sample (particles or host liquid)
- Non-invasive analysing method
- Fit for measurements of particles in aqueous environments

## 2 Scope of work

The aim of this work is to be able to predict the performance of the testing probe in the field - especially considering the oscillation behaviour of the ultrasonic transducer by comparing real measurements with FEM simulations. For further researches additional methods of analysis, which are covering the significant parts of the testing probe, are presented. These analysis include a FEM simulation of the complex acoustic admittance and measurements of the complex electric admittance.

This thesis consists of three parts: The first two are dealing with vibration analysis of the piezoceramic discs used in a prototype of the testing probe as ultrasonic transducers. The discs are analysed with a vibrometer and tested for their vibration behaviour. Graphical and numerical data are used to compare the real measurement results with those of a simulation done in *ANSYS Workbench*. First, the vibration modes of the piezoceramic elements will be reviewed alone. Therefore the measurement is done with three separate subjects to ensure the generality of the data. For the comparison a standard model of a piezoceramic disc is built and analysed using the material data of the real discs. For the vibrometer the devices are actuated with different frequencies in a range from 0 to 300 kHz. As results we obtain frequency bands with peaks which mark the natural frequencies and thus the oscillation modes of the discs. *ANSYS Workbench* is able to perform modal and harmonic analysis- the first tool provides the theoretical modes, the second shows the vibration behaviour of the discs when actuated at their natural frequencies by providing instantaneous values measured at the discs' surface. The instantaneous values are subject of the second part of the thesis, in which the results of a harmonic analysis again are compared and discussed in comparison to the results obtained by using the vibrometer.

The third part of the thesis presents options for further development of the testing probe. Real measurements of the electric admittance are performed with variation of the composition of the process medium and the gateway width between the carrier for the transducer and the reflector. In *ANSYS Workbench* the acoustic admittance has been calculated again with the variation of the gap size and the water-ethanol mixture used as fluid medium. In the end of each part the results of measurements and simulations are compared and discussed.

## 3 Fundamentals

### 3.1 Sound waves and ultrasonic particle manipulation

According to Lerch et al. [36] sound appears as mechanical oscillations of elastic media. These oscillations spread through gases, liquids and solids in the form of sound waves. Another approach is the depiction of sound as pressure perturbation propagating as a wave. [37] Sound waves are defined by their intensity and frequency. The human ear can hear tones between 16 Hz and 20 kHz. Ultrasound is found at frequencies from 20 kHz to 1 GHz. The characteristics of sound waves depend on the physical condition and properties of the medium. For example density and temperature can influence the speed of sound immensely. Further, damping effects can occur which are caused by internal friction, heat conduction effects and molecular absorption. [36]

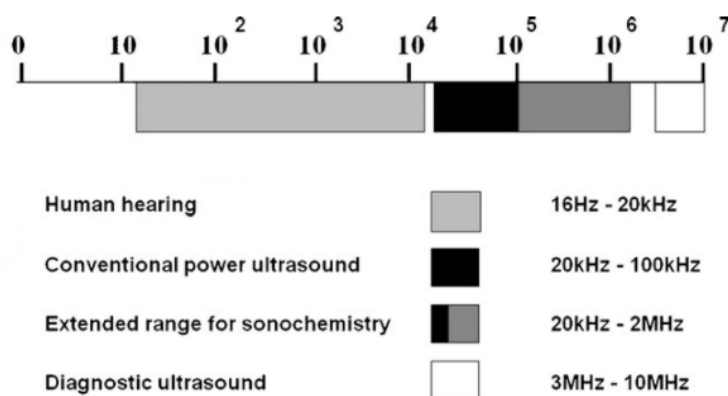


Figure 3: Detailed overview of ultrasonic frequencies [3]

For trapping particles a standing acoustic wave is needed. For the creation of a standing wave a transducer emits a wave which is reflected by a parallel wall. The emitted wave and the reflected wave superpose and form a quasi-standing wave (Figure 4). At the nodes the amplitude has a zero crossing point. In a three-dimensional model this is where the nodal planes lie. [38]

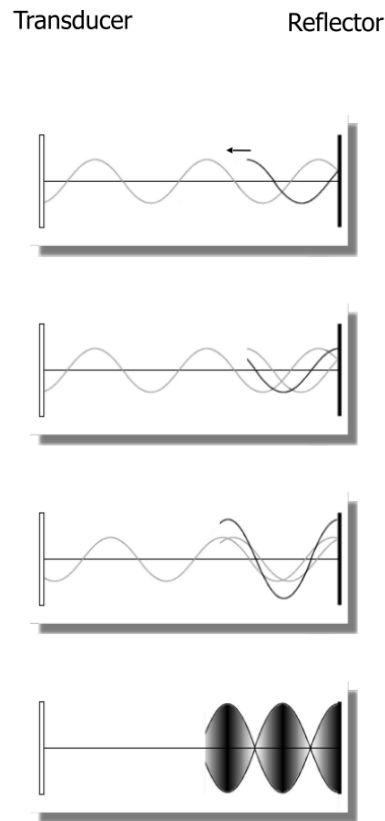


Figure 4: Formation of a standing wave [38]

To understand the forming process of a standing wave we first look at the one-dimensional wave equation seen in Equation 1. The variable  $u$  in Equation 1 can be replaced by the acoustic parameters sound pressure  $p$  (Eq. 2) or sound particle velocity  $v$  (Eq. 3). [39]

$$\frac{\partial^2 u}{\partial x^2} = \frac{1}{c^2} \frac{\partial^2 u}{\partial t^2} \quad (1)$$

$$\frac{\partial^2 p}{\partial x^2} = \frac{1}{c^2} \frac{\partial^2 p}{\partial t^2} \quad (2)$$

$$\frac{\partial^2 v}{\partial x^2} = \frac{1}{c^2} \frac{\partial^2 v}{\partial t^2} \quad (3)$$

According to Sinambari, Sentpali et al. [39] the propagation of sound waves in three-dimensional space can be described by the one-dimensional equations above in case of the sound wave being a planar wave propagating in x-direction after a disturbance in the medium. Following this assumption the wave equations for  $p$  and  $v$  would not change.

The sound waves are now longitudinal waves with acoustic parameters  $p$  and  $v$  being steady in  $y$ - and  $z$ -direction. An approach to the solution of the equations using the velocity potential  $\varphi$  is presented in the following form with respective complex notation (Eq. 4).

$$\text{With } p = -\rho \frac{\partial \varphi}{\partial t} \quad \text{and} \quad v = \frac{\partial \varphi}{\partial x}$$

$$\varphi = \phi * \cos(\omega t \pm kx) \quad (4) \quad \underline{\varphi} = -\phi * e^{i(\omega t \pm kx)} \quad (7)$$

$$p = P * \sin(\omega t \pm kx) \quad (5) \quad \underline{p} = \pm iP * e^{i(\omega t \pm kx)} \quad (8)$$

$$v = V * \sin(\omega t \pm kx) \quad (6) \quad \underline{v} = \pm iV * e^{i(\omega t \pm kx)} \quad (9)$$

Here  $\phi$ ,  $P = \phi * \omega * \rho$  and  $V = \phi * \omega / c$  are the amplitudes of the respective waves. The angular frequency is depicted by  $\omega$  and speed of sound by  $c$ . Speed of sound is a parameter depending on material properties and can be calculated by multiplying wave length  $\lambda$  by frequency  $f$  (Eq. 10). The variable  $k$  stands for the wave number and can be calculated according to Equation 11.

$$c = \lambda * f \quad (10) \quad k = \frac{\omega}{c} = \frac{2\pi}{\lambda} \quad (11)$$

A standing wave is the product of two plane waves of similar amplitude and the same wave length, running in opposite directions and interfering each other. Due to the linearity of the equation addition leads to the formation of a new solution - the waves superimpose. [40] Mathematically, for sound particle velocity  $v$  this is represented as follows [39]:

$$\text{With } e^x + e^{-x} = 2\cosh(x)$$

$$\sum \underline{v} = 2V * \frac{e^{+ikx} + e^{-ikx}}{2} e^{i\omega t} = 2V * \cosh(ikx) * e^{i\omega t} = 2V * \cos(kx) * e^{i\omega t} \quad (12)$$

The new wave has twice the amplitude as the original ones in case the phase shift is 0 or  $\lambda/2$  as seen in Equation 12. The nodal planes are half a wave length apart. A standing wave can be formed, for example, when an incident wave encounters a boundary between two mediums and gets reflected.

For this the two mediums must have different sound velocities  $c_1 \neq c_2$ . An important physical quantity to determine the reflection of sound is the characteristic acoustic impedance  $Z_a$ . It describes the ratio of sound pressure  $p$  to particle velocity  $v$ . Its reciprocal value is the characteristic acoustic admittance  $Y_a$ , which is calculated in the simulations described in Chapter 5.3.2.

The acoustic admittance is the ratio of particle velocity  $v$  to sound pressure  $p$ . Like the electric admittance the acoustic admittance  $Y_a$  is a complex physical quantity with a real part  $G_a$  called conductance and an imaginary part  $B_a$  called susceptance (Eq. 13). For the impedance  $Z_a$  the real part is called resistance  $R_a$  and the imaginary part is called reactance  $X_a$  (Eq. 15) equal to the notation for electric impedance and admittance described in Chapter 3.2. [41]

Acoustic admittance

Acoustic impedance

$$Z_a = R_a + iX_a \quad (13) \quad Y_a = G_a + iB_a \quad (15)$$

$$Z_a = \frac{p}{v} = \frac{1}{Y_a} \quad (14)$$

From the impedances of the two mediums the reflection coefficient  $R_c$  and transmission coefficient  $T_c$  for the sound wave as seen in Figure 5 can be determined. The reflection coefficient  $R_c$  can also be depicted as ratio of reflected pressure and incident pressure (Eq. 16). Same applies for the transmission factor: Here the reflected pressure is replaced by the transmitted pressure (Eq. 17) [40].

$$R_c = \frac{p_r}{p_i} = \frac{Z_2 \cos \theta_i - Z_1 \cos \theta_t}{Z_2 \cos \theta_i + Z_1 \cos \theta_t} \quad (16) \quad T_c = \frac{p_t}{p_i} = \frac{2Z_2 \cos \theta_i}{Z_2 \cos \theta_i + Z_1 \cos \theta_t} \quad (17)$$

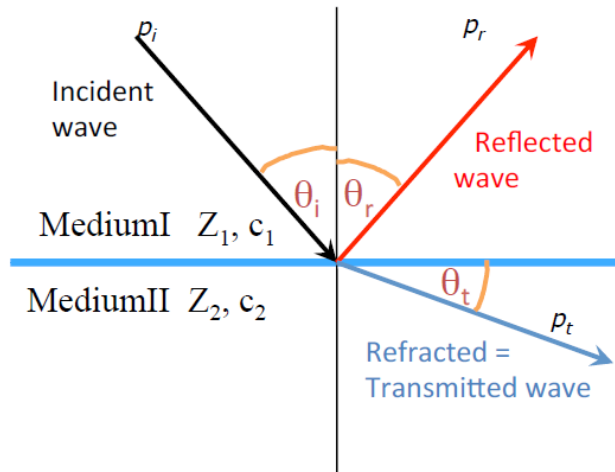


**Figure 5: Reflection and Transmission of sound waves,  $c_1 > c_2$  [40]**

At the interface between an acoustically soft and dense medium the reflection coefficient increases.

Particles suspended in a liquid flowing through a standing wave are manipulated by radiation forces. These forces can be divided into three types: Axial primary radiation force, transverse primary radiation force and secondary radiation force (Figure 6). [38] Primary radiation forces act in two directions- axial and transversal- and are induced by the interaction between the acoustic field and the single particles. Secondary radiation forces designate the interaction between two or more particles. [26]

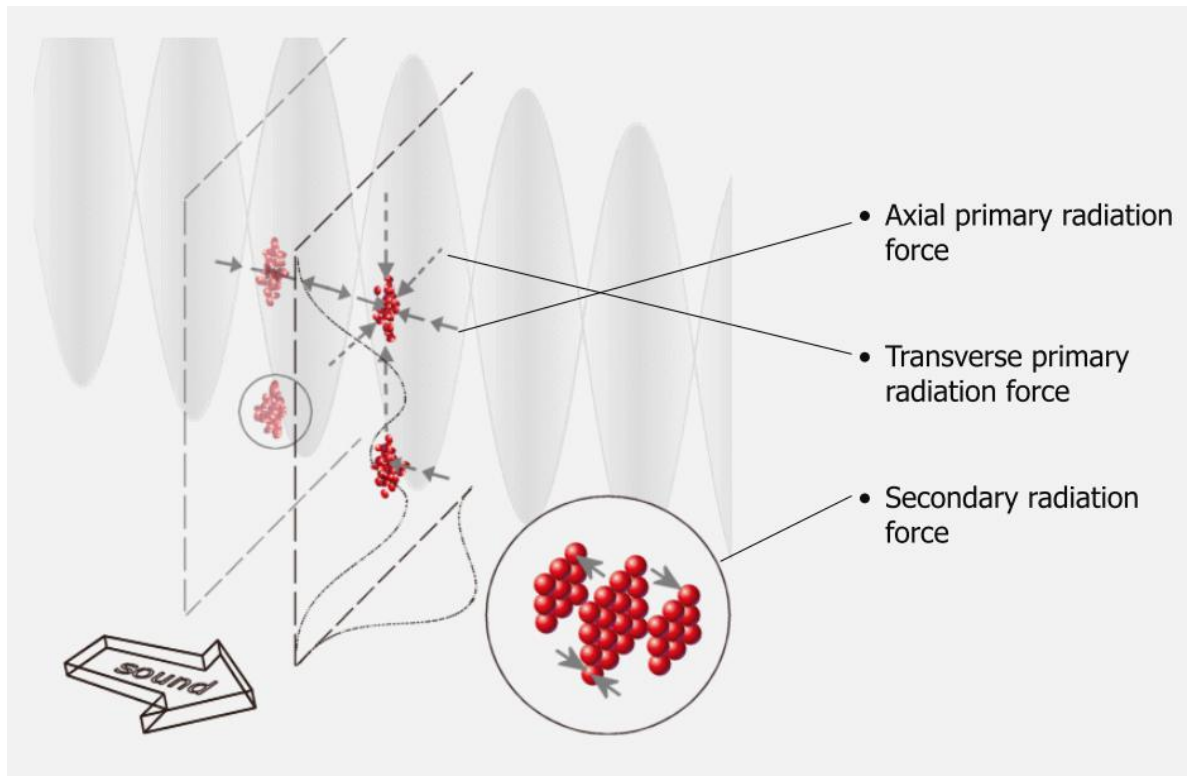


**Figure 6: Acoustic radiation forces [38]**

The forces result in formation of planes which are half of a wavelength apart- the nodal planes at the pressure nodes (zero crossing point) and the anti-nodal planes at the pressure maximum. According to Lendl, Radel et al. [1] whether the particles are driven into the nodal or the anti-nodal planes depends on the difference between the sound speeds and mass densities of the particles and the medium. When the particles reach the acoustic field the axial primary radiation forces push them into the planes. They come closer and the transversal and the secondary radiation force support further accumulation. [26] The offset of the planes can be controlled by varying the wavelength. This way particles can be moved to an exact position for ATR FTIR spectroscopy.

### 3.2 Electric admittance

The electric admittance  $Y_e$  is the inverse of the electric impedance  $Z_e$ . The impedance describes how much current gets impeded in a system, the admittance indicates how much current is admitted in a conductive system or circuit. The electric impedance, being a complex quantity, describes the effects of resistance  $R_e$  and reactance  $X_e$  (Eq. 19). Electric admittance being the reciprocal value of the impedance  $Y_e = 1/Z_e$  includes the effects of conductance  $G_e$  and susceptance  $B_e$  (Eq. 18) with conductance corresponding to electric resistance and susceptance to reactance. [42]

Electric admittance

$$Y_e = G_e + jB_e \quad (18)$$

Electric impedance

$$Z_e = R_e + jX_e \quad (19)$$

### 3.3 ATR FTIR spectroscopy

Andanson et al. [34] describes the usage of ATR FTIR spectroscopy for analysing processes at solid/liquid interfaces. IR spectroscopy provides information about the structure of molecules (e.g. in bioreactors the biochemical composition of cells [1]) and their environment but only if located on the surface and near to the surface in the sample. By measuring concentrations of products a method for reaction monitoring is given. The sample is irradiated and absorbs wavelengths from the spectrum of the light source. These are characteristics for the sample's chemical structure and environment. [43]

One can differ between three IR regions: near, mid and far infrared. In the far IR region (3-400  $\text{cm}^{-1}$ ) lattice oscillations cause the absorption of IR radiation, in the mid IR region intra molecular movements are responsible. [43]

### 3.4 Piezoelectric effect and ultrasonic transducer

When an external force affects piezoelectric materials an electric charge is produced because of displacements within the lattice structure. This is called the piezoelectric effect. Mechanical energy is converted into electric energy. [44] The production of elastic strain caused by applying an external electric field is called the converse piezoelectric effect.

This is used in transducers to create ultrasonic waves. Some natural examples for those materials are quartz crystal, ammonium dihydrogen phosphate and Rochelle salt. Further common piezoelectric materials are man-made aluminium nitride (AlN) and artificially produced lead zirconate titanate (PZT). [45, 46] The samples used for this research are made from a piezoceramic material called PIC181 which is a modified PZT.

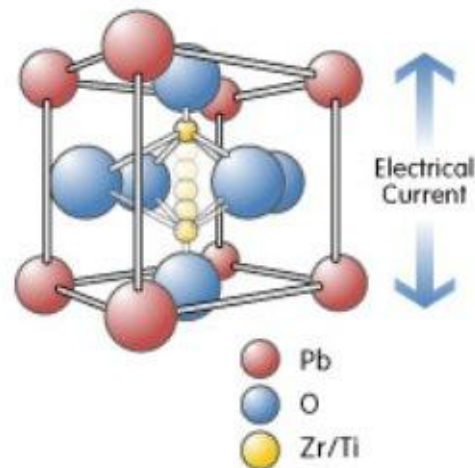


**Figure 7: Piezoelectricity in PZT [47]**

In a relaxed piezoelectric crystal the focuses of positive and negative load lie close together- no charge is produced. External stress or strain cause a displacement and thereby a charge. Precondition for piezoelectricity is an noncentrosymmetric crystal structure. [48] PZT belongs to the kind of ceramics which show piezoelectricity. Some ceramics have unordered dipoles and therefore show no piezoelectric effect. They can be poled by heating them to above their Curie temperature. At this point the lattice changes to a symmetric structure without polarisation. An electric field is applied while the temperature decreases. This way an ordered polarisation is forced upon the materials. [46] PZT is known for inducing larger electric voltages when mechanical stress is applied and showing larger displacements when voltage is applied. [44]

The parameters and coefficients used to define the polarised piezoelectric material in this thesis are stiffness or anisotropic elasticity  $c^E$  (matrix in Figure 14 for constant electric field), piezoelectric matrix relating stress/electric field  $e$  and relative permittivity  $\epsilon^S$  (constant deformation or strain). Further important piezoelectric coefficients are the piezoelectric charge coefficient  $d$  and compliance or elasticity coefficient  $s^E$  (for constant electric field).

The relative permittivity  $\epsilon$  is defined as the ratio of the absolute permittivity of the material and the permittivity in vacuum  $\epsilon_0$  which is  $8.85 \times 10^{-12}$  F/m. For  $\epsilon$  indices are defined which correspond to how the permittivity coefficient depends on the orientation of the electric field and the dielectric displacement. The letters  $T$  and  $S$  indicate whether the coefficient applies for constant mechanical stress  $T$  or strain  $S$ . [44]

The ratio of mechanical stress  $T$  and mechanical strain  $S$  is depicted by the compliance or elasticity coefficient  $s$ . As for  $\epsilon$  similar indices are applied for constant mechanical stress  $T$  and strain  $S$  as well as their spatial orientation. The compliance coefficient  $s$  and anisotropic elasticity  $c$  are used for the two different ways to define stress and strain properties for piezoelectric materials in a FEM program as *ANSYS Workbench* (see Chapter 4.3). Their mathematical relation is  $[s^E] = [c^E]^{-1}$ . [49]

The piezoelectric charge coefficient  $d$  describes the ratio of induced electric charge to mechanical stress. Contrary the piezoelectric matrix relating stress/electric field  $e$  describes the relation between mechanical stress  $T$  and electric field  $E$ . Their relationship can be depicted as follows: [49]

$$[e] = [s^E]^{-1}[d]$$

The electric and mechanical properties can be interrelated mathematically in the following two Equations 20 and 21: [44]

$$D = d \times T + \epsilon^T \times E \quad (20)$$

$$S = s^E \times T + d \times E \quad (21)$$

Where

$\epsilon^T$	Permittivity or dielectric matrix for $T = \text{const.}$
$D$	Electric flux density
$d$	Piezoelectric charge coefficient
$E$	Electric field
$S$	Mechanical strain
$s^E$	Compliance or elasticity coefficient for $E = \text{const.}$
$T$	Mechanical stress

The pendants to the equations above are the following two which are required by *ANSYS Workbench*. [44, 49]

$$D = e^t x S + \varepsilon^S x E \quad (22)$$

$$T = c^E x - e x E \quad (23)$$

Where

$\varepsilon^S$	Permittivity or dielectric matrix for S = const.
$c^E$	Stiffness or anisotropic elasticity matrix for E = const.
$D$	Electric flux density
$E$	Electric field
$e$	Piezoelectric matrix relating stress/electric field
$e^t$	Piezoelectric matrix relating stress/electric field transposed
$S$	Mechanical strain
$T$	Mechanical stress

Both equation pairs Eq. 20, 21 and Eq. 22,23 can be converted into each other as demonstrated by Imaoka in his work [49].

## 4 Materials and methods

To succeed in creating a functional tool for further development of the testing probe the simulation model needs to be verified by analysing its resemblance to reality. For this purpose experiments and corresponding FEM simulations are compared. For the future performance of the testing probe the vibration behaviour of the ultrasonic transducers are significant. The experiments were performed with the aid of a vibrometer. This way vibration modes and instantaneous values were obtained. The results are displayed as frequency bands, vibration modes and instantaneous values. For unaltered measurement conditions a stand for the fixation of the discs was constructed. The FEM simulation consists of a modal and harmonic analysis. Both methods are described below.

For the last part of the thesis a prototype of the testing probe was used to measure the complex electric admittance. The other analysing method for further development of a FEM model and its verification is based on the calculation of complex acoustic admittance. This can be done in the *Harmonic Response* simulation by using a special command.

### 4.1 Vibrometer measurements

The Laser Doppler Vibrometer presents an alternative to laser interferometers for the capture of surface oscillations. During the analysis of moving surfaces the relative movement of reflector and detector causes a frequency shift of the light due to the optical Doppler effect. This can be seen especially at the absorption and reemission of the light by the surface. Equation 24 shows the relation between the velocity of the surface  $v_s$ , the wave length  $\lambda$  and the frequency shift  $\Delta f$ . [36]

$$\Delta f = \frac{2v_s}{\lambda} \quad (24)$$

Equation 24 can be applied for a laser beam at the right angle to the surface. For a deviating incident angle  $\vartheta$  the equation needs to be modified to include the angle to Equation 25:

$$\Delta f = \frac{2v_s}{\lambda} \cos \vartheta \quad (25)$$

The frequency shift can be evaluated using an interferometer. Lerch, Sessler et al. [36] describe this process for a Mach-Zehnder interferometer. Here a light beam for reference and one for measurement superpose on a detector and create a light and dark pattern.

This pattern bases on the movement of the sample's surface, by which the measurement beam is reflected before, and the constant way of the reference beam. Every repetition of the pattern indicates the movement of the sample representing half a wave length depending on the light source. This variation in the path length of the light beam correlates to the frequency shift. To be able to determine the direction of the oscillation, a Bragg cell is used to modulate the reference beam.

The vibrometer, used for measurement in this thesis is manufactured by Polytec GmbH, Waldbronn, Germany, and can be seen in Figure 8. The Polytec Scanning Vibrometer, short PSV, includes an OFV552 Fiber Vibrometer, a MSA400 Micro System Analyzer, a MSA400 Junction Box and an OFV5000 Vibrometer Controller. All measurements in this thesis were taken with the PSV software version 9.0. To receive an accurate result for the examined piezoelectric element three subjects from the same batch were analysed- Sample 1, Sample 2 and Sample 3. There were three testing rows done for every sample, each containing 10 snap-shots of the surface from the centre to the edge of the disc. The rows were separated by an angle between 70 to 90 degrees to cover all possible results symmetrically. For defining the scanning points a grid with 35 nodes was chosen. For arranging the subject at a certain position and adjusting the scanning points the shots had to show an overlapping area. This area was arranged by hand as uniform as possible between every shot what is also true for the positioning of the rows.



**Figure 8: Polytec Scanning Vibrometer (PSV) and oscilloscope**

A handmade support was used as a stand to keep the discs in a flat position. The stand is described in detail in the following chapter below. It also includes the contacts for the transmission of the signal.

The signal was applied via an internal source and visualised by an oscilloscope. In the software one defines a trigger to unify the starting points of the measuring and an interval for the frequencies which you want to analyse. Basically the following settings were used for all measurements:

**Table 2: Vibrometer settings**

Bandwidth	500
Range	0 - 300 kHz
Digital Velocity Decoder	VD-06, 50 mm/s/V
Trigger / Waiting for Trigger	On / 0,3 s
Generator	1,36 V

These settings can be saved as a default setting package with the result that for each measurement the same preconditions can be applied. The first results received are frequency bands showing peaks from which the natural frequencies of the recordings can be read. At each peak the oscillation of the surface is examined in all three spatial directions. The values of the instantaneous can be displayed numerically for further analysis at each node of the defined grid. It has been shown that an air-conditioned measuring environment is necessary for consistent results. At the first attempts at similar settings but different temperatures the values have fluctuated distinctly.

## **4.2 Stand for vibrometer measurements**

For the measurements done with the vibrometer it was necessary to fix the piezoceramic discs. For this purpose a stand was constructed. The base of the stand is made from two wooden plates glued together. The wires for the pins run through a channel cut into the top plate. Wires as well as samples are fixed by plastic sheets and screws mounted to the wooden base. The sheets vertically and horizontally hold the disc in place. As seen in there are two holes for the pins in lowest plastic sheet. On top omissions are cut into the second and the third sheet where the discs can be loaded as seen in Figure 9.

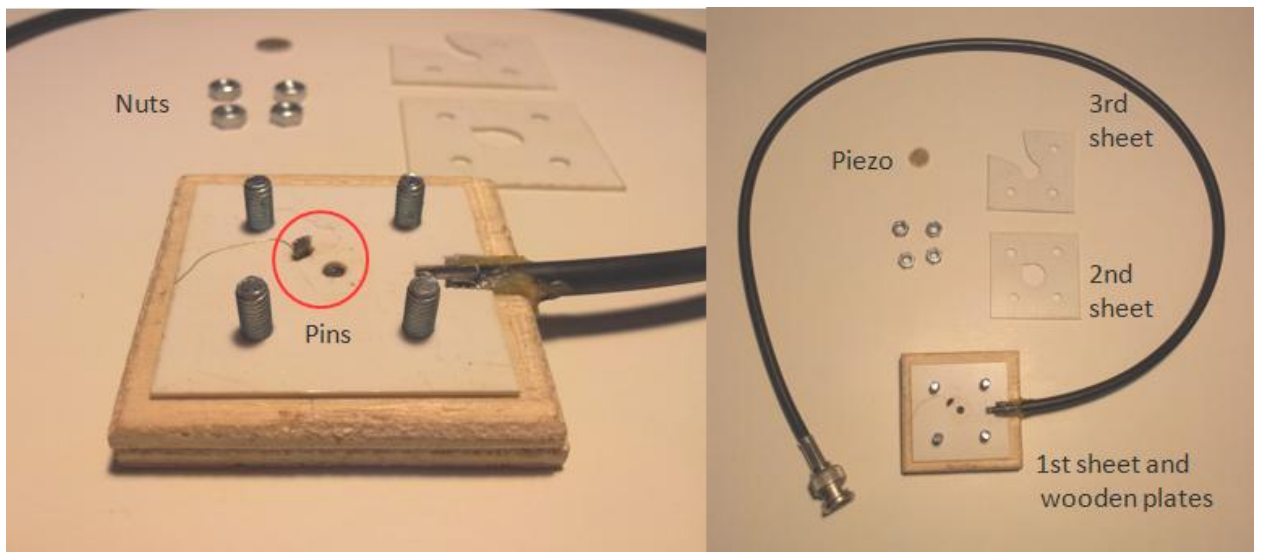


**Figure 9: Components of the stand**

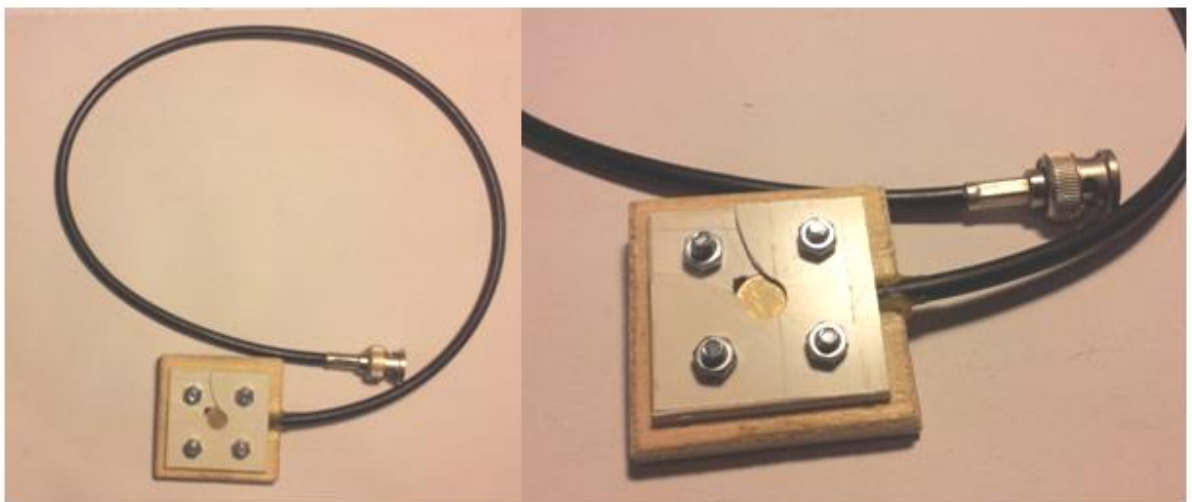


**Figure 10: Stand for vibrometer measurements, assembled with piezoceramic sample**

In Figure 10 we see the completely assembled stand and a piezoceramic disc clamped in the centre. On the downside of the disc the two electrodes are separated by a ring. The pins are situated accordingly on the lowest plastic sheet.

### 4.3 Finite Element Method (FEM)

Finite element method is a common numerical solution method based upon the segmentation of the concerning problem into smaller sections or finite elements.

Fröhlich [50] gives a significant summary of FEM and its application in his work. FEM is a solution method applicable for problems concerning connected structures. Splitting those structures into smaller elements enables the characterisation and calculation of this individual parts in a simpler way. Adjoining elements are coupled through nodes. By defining boundary conditions at the elements' nodes equations can be passed from one to other adjoining elements continuing through the whole structure. With this method static and dynamic analysis can be done- a dynamic analysis discussed in this work is the modal analysis of the piezoceramic discs. The element size and form have great influence on the precision of the simulation and its approximation to reality. Calculations like this can only provide an approach to reality but no exact results. This is caused by the fact that the calculation is done for discrete nodes and not a continuous structure. Furthermore boundary conditions and parameters cannot be set in the model the exact same way as they apply for real conditions. With the aid of FEM programs different technical problems can be described and solved without greater effort for the user. However a basic understanding of the scientific context and the methods used for the simulation is necessary for a professional evaluation of the results. [50]

Before the simulation is started one needs to know how to approach the problem. The real model needs to be converted into a physical, mathematical and numerical model. For the physical model the effective physical laws are displayed in form of equations. Conditions as dimension and negligible effects are determined. In the following mathematical model further settings as time dependence, type of differential equations and boundary conditions are defined. The numerical model is responsible for the discrete specification of the elements and algorithms for the calculation. [50] The simulation itself splits into three parts: Pre-processing, solution and post-processing. [50, 51] Pre-processing includes the acquisition of the geometry for the simulation model as well as definition of material data and the meshing process. Boundary conditions need to be set for the solution of the equations defined by the mathematical model. The quality of the mesh affects the calculation process and precision of results. In post-processing the display of results and further processing can be chosen individually. Most commonly used FEM programs are built after the same modular principle seen in Figure 11 as described by Fröhlich [50] and Westermann [51].

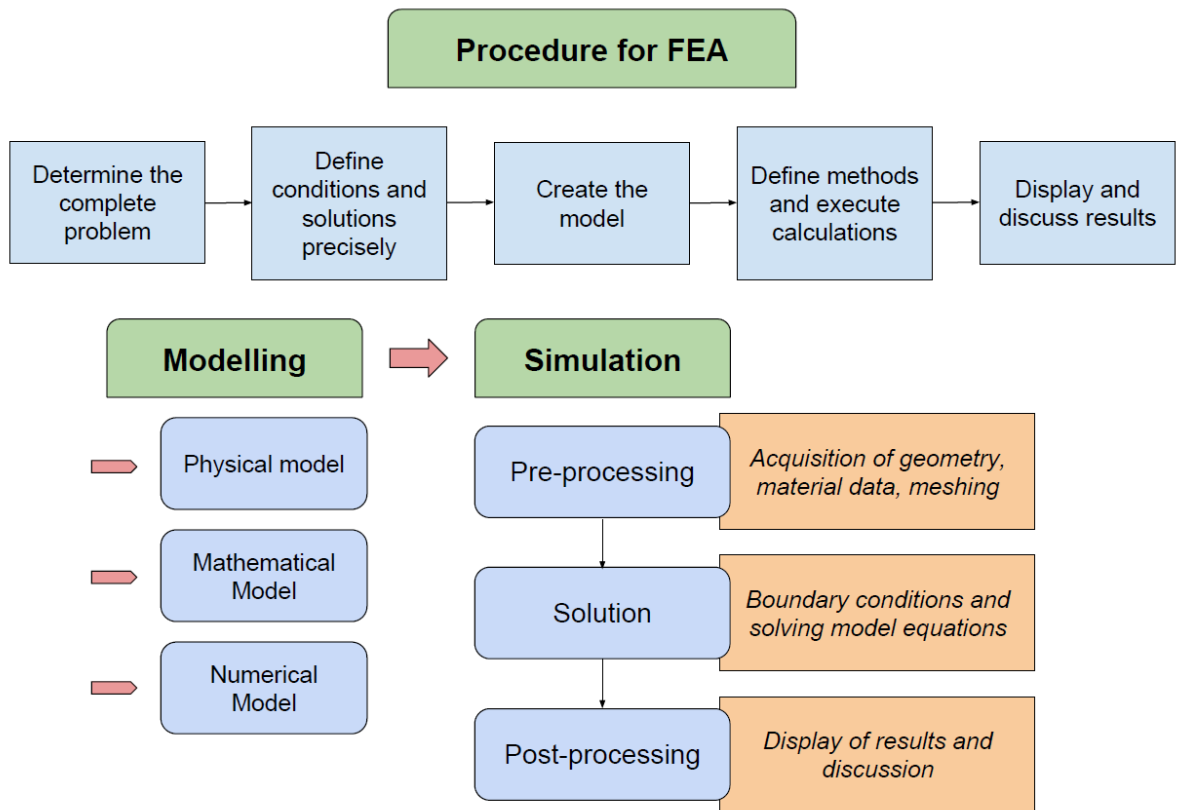


**Figure 11: Basic procedure and modular workflow of Finite Element Analysis**

The simulations for this thesis are done in *ANSYS Workbench 15.0*. Additional extensions used are the *ACT\_Acoustics\_Extension\_R145\_v8* and the *ACT\_Piezo\_R150\_v8*. The different models are built in *ANSYS DesignModeler* and meshed with *ANSYS Meshing*. The analysis systems used are *Modal Analysis* and *Harmonic Response*.

Acoustic simulations examine the acoustic medium and its surroundings. Mostly the acoustic medium is a fluid like air or water adjoining a solid body. The results of such analyses are usually based on the parameters pressure, velocity, temperature and density. Furthermore the behaviour of sound waves can be observed under various conditions. In acoustic simulations effects as sloshing as well as attenuation, transmission and dispersion of acoustic waves can be calculated. The interaction between the acoustic medium (mostly fluid) and a solid structure is defined by using coupled or uncoupled models. Coupled models allow specific settings for the fluid-solid interface. Uncoupled models ignore the fluid-structure interaction completely. For this purpose, the adjacent phase is provided with an appropriate boundary condition. The absorption coefficient can be adjusted depending on the material properties.

Two basic assumptions for acoustic analysis are the characterisation of the fluid as compressible and non-flowing. The second one presents a great disadvantage for further researches regarding the application of the FTIR testing probe for particle manipulation. In this case it is necessary to include the influence of fluid flow since the forces resulting from the flow should be compared to the radiation forces generated by the sound waves. The ratio of these two is indicative for the effectiveness of the probe's performance in particle manipulation. One can try to bypass this issue by coupling *ANSYS Mechanical* with *ANSYS Fluent*. [41]

Piezoelectric analysis done with FEM programs differ depending on whether static or dynamic issues are solved. In case of static analysis the user needs to set specific properties to define the piezoelectric material such as structural elasticity, piezoelectric coupling and dielectric permittivity. For dynamic analysis additional information as density, structural damping, dielectric damping, stiffness under constant electric field, the piezoelectric stress matrix and relative permittivity under constant strain is required. The orientation of the crystal structure of a piezoceramic needs to be considered when entering material data. Properties for boundary conditions can be mechanical loads, voltage and charge. As results for piezoelectric applications one is able to display electric field, electric flux density and voltage among others. [52]

The user interface in *ANSYS Workbench* is divided into several windows. One of them is called *Project Manager*. Here constraints and parameters for calculations are managed. It can be used to link the tools for analysis together so that previous results can be used for the next calculation. The tools consist of several component systems including *Engineering Data*, *Geometry*, *Model*, *Setup*, *Solution* and *Result*. In the *Project Manager* some of them can be used alone and later linked to other tools. Workbench allows the integration of different CAD files done with *CatiaV5*, *SolidWorks* or *OneSpaceDesigner* to name a few. This gives the opportunity of working with a more sophisticated CAD environment but still being able to use the same model for FEM or CFD. *ANSYS* comes with its own modelling application called *DesignModeler*. It is also the application used to built the geometry for this research.

*ANSYS Workbench* is able to perform different types of analysis:

- Fluid Flow
- Harmonic Response
- Static Structural
- Magnetostatic
- Thermal
- Modal
- Transient Structural
- Etc.

Material properties are defined using the component *Engineering Data*. The user has access to a data base containing commonly used materials, solid and fluid. Properties which can't be set via analysis tool are defined in this component. After importing or creating the geometry one can proceed with the mesh and further constraints for the model in *Mechanical Application*. *Mechanical Application* provides the actual environment for FEM. Here the analysis and the simulation are prepared. This setup consists of the mesh, calculation and the way the results are displayed. [53]

The method and refinement of the mesh can be set in the analysis tool. For the definition of the refinement here *Edge*, *Face* and *Body Sizing* are used. *Mapped Face Meshing* can be used by defining the mesh on one face of the body and sweeping it through the body to the other side. For more complex or composite models one can use *MultiZone* for enabling meshing of different methods in one body. This facilitates the combination of different types of elements. Using a rigid meshing method from the beginning can cause improper or poorly distributed element form and sizing. The model and the mesh can be seen in Figure 12 and Figure 13. Figure 13 also shows the piezoceramic body (blue disc) attached to the Macor carrier (grey body). The fluid body, in which the standing wave develops, is depicted as a broad green block.

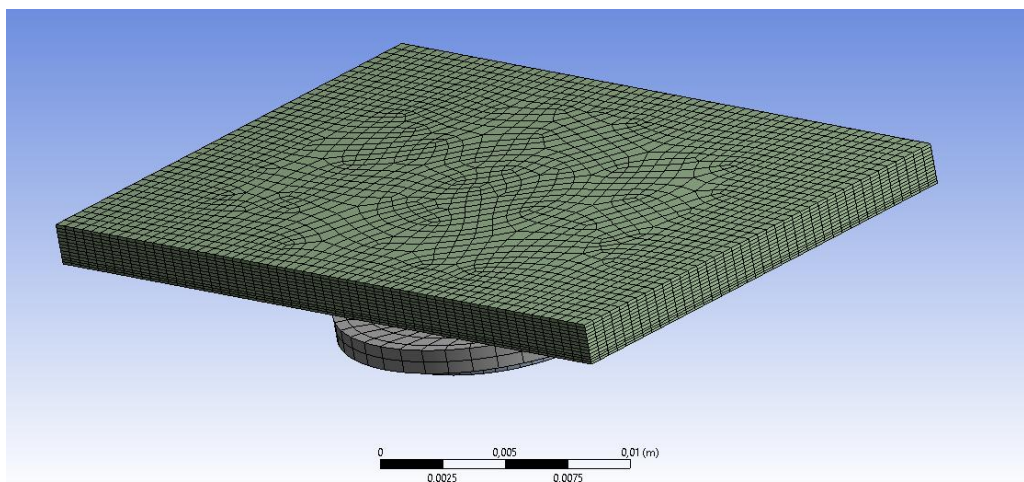


**Figure 12: Top view mesh for harmonic analysis of testing probe prototype**

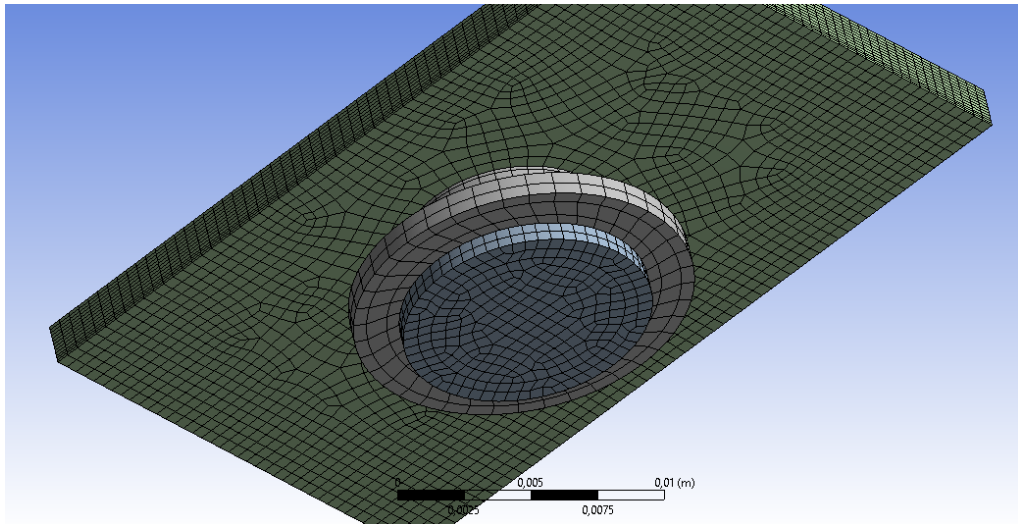


**Figure 13: Bottom view mesh for harmonic analysis of testing probe prototype**

After the solving process is completed details about the results and the solving process itself are found in *Solver Files Directory*. Information about the solution and equations solved as well as error messages can be checked. In case of using *APDL* commands for creating specific files for exceptional results, these exact files are saved to this directory. For post-processing, results can also be exported to *Excel*.

For this work modal and harmonic analysis were performed in *ANSYS Workbench*. Modal analysis were used to find natural frequencies and appendent modes of a structure. For acoustic applications this tool can be used to display patterns of standing waves formed in acoustic mediums. Harmonic analysis allow the calculation of the response of a structure to harmonically acting loads. The results are functions of frequency depicting a chosen response quantity. Again in both tools fluid-structure interaction can be considered. [41]

#### **4.4 Piezoceramic elements**

The piezoceramic discs used for this research are produced by PI Ceramic GmbH, Lederhose, Germany. The three test objects Sample 1, Sample 2 and Sample 3 are made from the same piezoceramic material - PIC181. PIC181 is a ferroelectrically hard lead zirconate titanate (PZT) material which can withstand high electric and mechanical stresses. [54]

For the simulation different material and piezoelectric properties had to be defined. This includes density  $\rho$ , anisotropic elasticity  $c^E$  (matrix in Figure 14 at constant electric field), permittivity constant (fixed), piezoelectric matrix relating stress/electric field  $e$  and relative permittivity  $\epsilon^S$  (constant deformation) as seen in Figure 15. Appropriate parameters were set for the model following data sheets (see appendix) provided by PI Ceramic:

### Engineering Data

$$\text{Density } \rho = 7850 \frac{\text{kg}}{\text{m}^3}$$

Table of Properties Row 3: Anisotropic Elasticity						
	A	B	C	D	E	F
1	(Pa)	(Pa)	(Pa)	(Pa)	(Pa)	(Pa)
2	1,523E+11					
3	8,909E+10	1,523E+11				
4	8,547E+10	8,547E+10	1,341E+11			
5	0	0	0	3,161E+10		
6	0	0	0	0	2,83E+10	
7	0	0	0	0	0	2,83E+10

Figure 14: Anisotropic Elasticity Matrix for PIC181

### Modal Analysis and Harmonic Response

Details of "Piezoelectric Body"	
<b>Scope</b>	
Scoping Method	Geometry Selection
Geometry	1 Body
<b>Definition</b>	
Polarization Axis	Z
Permittivity Constant	8.854E-12 [A A sec sec sec sec kg <sup>-1</sup> m <sup>-1</sup> m <sup>-1</sup> m <sup>-1</sup> ]
PIEZ e31	-4.5 [A sec m <sup>-1</sup> m <sup>-1</sup> ]
PIEZ e33	14.7 [A sec m <sup>-1</sup> m <sup>-1</sup> ]
PIEZ e15	11 [A sec m <sup>-1</sup> m <sup>-1</sup> ]
DPER ep11	740
DPER ep33	624
RSVX	0 [kg m m m A <sup>-1</sup> A <sup>-1</sup> sec <sup>-1</sup> sec <sup>-1</sup> sec <sup>-1</sup> ]
RSVY	0 [kg m m m A <sup>-1</sup> A <sup>-1</sup> sec <sup>-1</sup> sec <sup>-1</sup> sec <sup>-1</sup> ]
RSVZ	0 [kg m m m A <sup>-1</sup> A <sup>-1</sup> sec <sup>-1</sup> sec <sup>-1</sup> sec <sup>-1</sup> ]

Figure 15: Parameter setting for Piezoelectric Body, PIC181

One needs to pay attention to the notation as there are two standards coming together when working with *ANSYS Workbench*. The widely used IEEE standard differs from the *ANSYS* notation in some cases.

For this the *Help-Function* of *ANSYS Mechanical* is useful for searching the exact definition of the input parameters which are required in Piezoelectric Body. Another helpful guidance tool is the publication by Imaoka [49] dealing exactly with this problem.

## 4.5 Testing probe prototype

The prototype of the testing probe was built for several analysis and for its application in different experiments as for the measurement of complex electric admittance described in Chapter 5.3.1. The manufacturing process is called stereolithography which is a popular method of 3D printing for rapid prototyping purposes. The term stereolithography covers all processes based on the solidification of liquid materials by photo polymerisation. A solid polymer is obtained from an uncured monomer by irradiating the monomer with a laser beam or UV light. [55] The prototype is made from a resin with a temperature stability of up to 65°C. The reflector used for the measurements in Chapter 5.3.1 is a piece which was cut from a calcium fluoride plate. This material will not be used on a regular base for future experiments. For this reason the reflector in the simulation model in Chapter 5.3.2 was defined as an acoustically hard material with an absorption factor set to 0 to create general preconditions for future calculations. The actual testing probe works with an ATR element made from zinc selenide and diamond.



**Figure 16: Prototype of the testing probe**

The piezoceramic transducer embedded in the prototype comes from the same batch as the transducers used for the vibrometer measurements described in the Chapters 5.1.1 and 5.2.1. The little white body seen on the right side in the gateway of the testing probe in Figure 16 is the Macor carrier for the piezoceramic transducer.

The piezoceramic transducer was glued onto the Macor carrier which transmits the sound waves to the fluid using a 2K epoxy resin glue.

The blue part in Figure 17 shows the arrangement of the Macor and the piezoceramic body. Through the gateway between Macor carrier and the top half of the probe flows the process medium carrying dispersed particles. The reflector is mounted vis-à-vis to the top face of the Macor carrier, which immerses into the fluid.

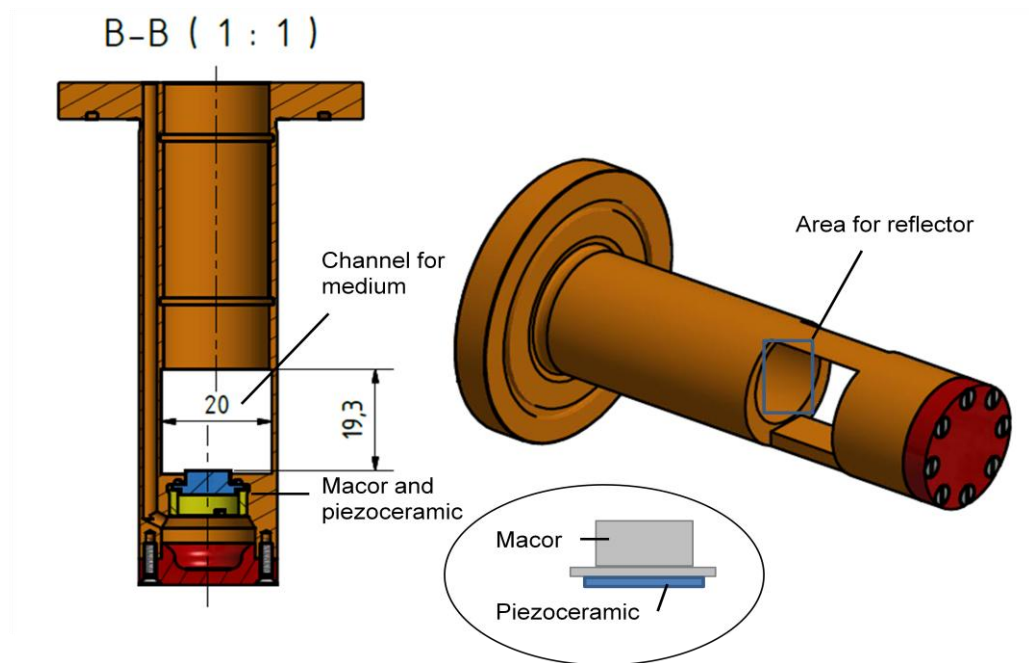


**Figure 17: Detail from engineering drawing of the testing probe prototype, by Stefan Tauber, Vienna University of Technology, blue...Macor and piezoceramic body**

Macor is a glass-ceramic material which can withstand high pressure and high temperatures. It can be machined easily using metal working tools and holds no porosity. This material can also be soldered with itself and other materials which makes it useful for various purposes.

[56]

## 5 Experimental

### 5.1 Modal analysis of a single piezoceramic disc

In this chapter the oscillation modes and the natural frequencies of the piezoceramic discs are explored. The modal analysis performed in *ANSYS Workbench* provides the natural frequencies of the piezoceramic disc model. At these frequencies the oscillation of the disc was observed and compared to the information obtained from the measurement. The results show similarities between the oscillation modes obtained by the vibrometer and calculated in *ANSYS Workbench*.

#### 5.1.1 Measurement

The measurement has been done using the Polytec Scanning Vibrometer (PSV) as described above (see Chapter 4.1). Three piezoceramic discs - Sample 1, Sample 2 and Sample 3 - have been examined. On each one of them the measurements were done on sections (snap-shots taken by the vibrometer) in a row from the centre of the disc to the edge. Every row contains 10 Shots. The three rows on each disc are separated from each other by an angle from 70 to 90 degrees.

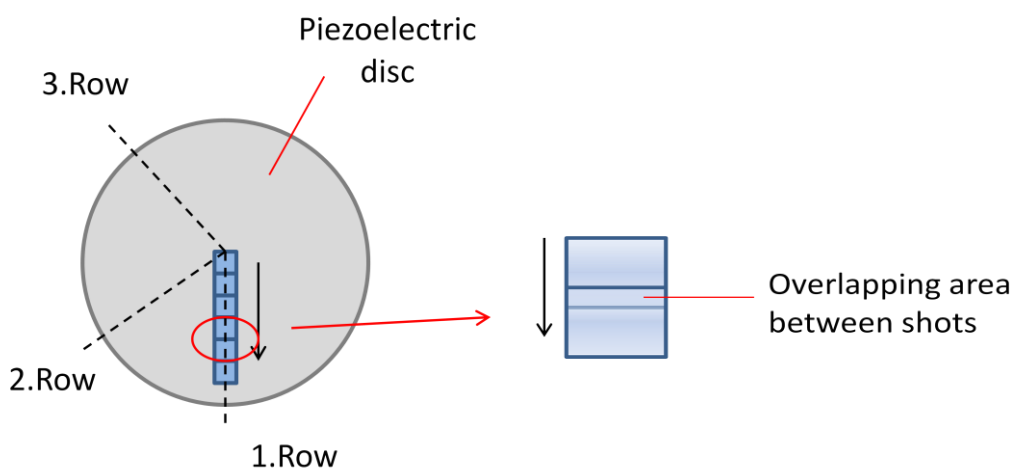
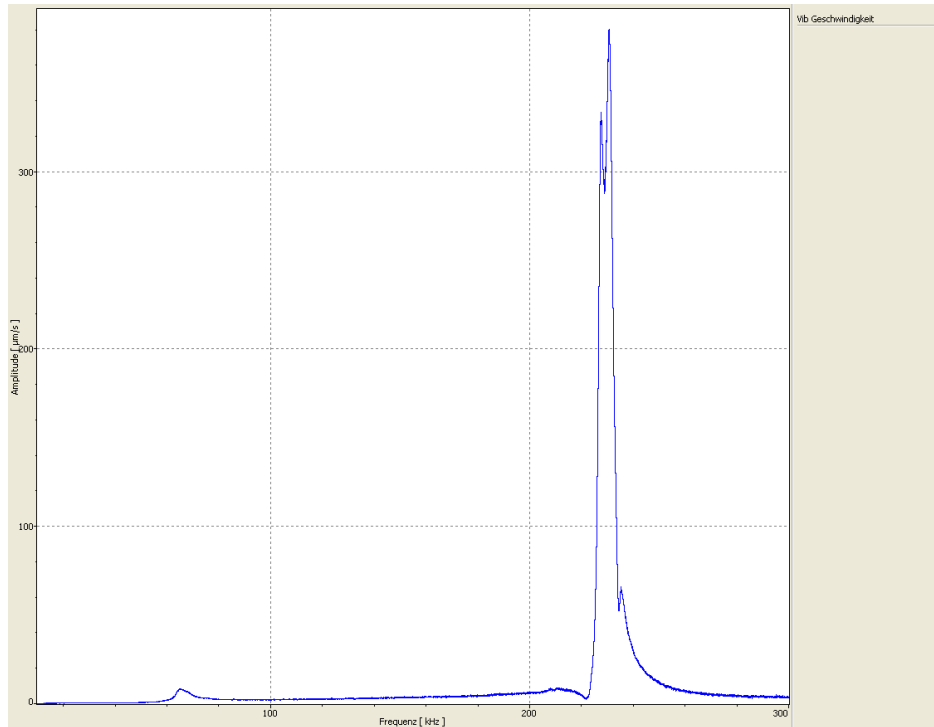


Figure 18: Procedure for measurement with PSV

The discs had to be fixed at several spots and faces in order to receive straight values in vertical direction. For this purpose a stand was built including the pins for voltage transfer. The constraints for the measurements are the same as listed in Chapter 4.1.

As a result for each Shot one receives a frequency band (Figure 19) in which the natural frequencies appear as peaks. At first the frequency bands were compared and the repeating natural frequencies are found. The tables showing the frequencies are added to the appendix of this work.



**Figure 19: Frequency band for Sample 1, 227 kHz, Row 1**

As seen in the tables (appendix) for Sample 1 the frequencies around 227 kHz and 231 kHz, for Sample 2 around 234 kHz and for Sample 3 around 229 kHz and 234 kHz were chosen. The means of these frequencies are as follows:

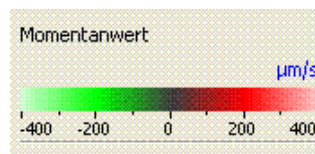
**Table 3: Means of the repeating frequencies [kHz]**

Sample 1	227,27	230,69	
Sample 2			233,99
Sample 3	229,05		234,29
Combined	228	230	234

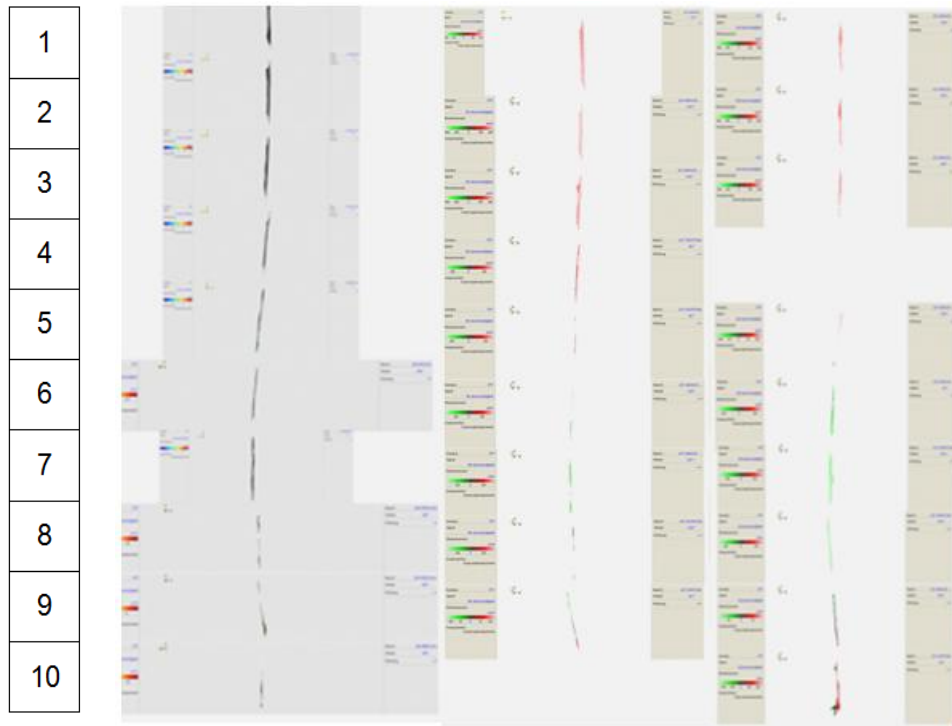
To make the oscillation visible with the aid of the PSV software by Polytec for every Shot animations of the oscillations at these three frequencies were generated showing the oscillation in all three spatial directions with corresponding scale and display of the phase angle. They show the movement of the disc's surface in form of a thin oscillating sheet.

The animations of the side views were scanned for demonstrative movements beginning with the deflection at the centre. When strung together the discs' oscillations from the centre to the edge can be seen for every disc combined in one image (from Figure 21 to Figure 25). Some spaces are left blank because of missing peaks at these frequencies in Table 3- for example in Figure 21, Row 2, last image.

In Figure 21 as in the following figures we see three rows of Shots taken during the measurement done with the vibrometer. The aligned snap-shots in each row show the maximum vertical deflection recorded from the side view of an animation of the oscillating surface. The range of the coloured scales is not the same in every image. The green side of the scale represents the positive direction of deflection with the red side being the negative one. These figures shall show torsions and other deformations of the surface during the oscillation without comparing the instantaneous values. These deformations are characteristic for the regarding oscillation mode and used for comparison to the modal analysis results in Chapter 5.1.2. Figure 20 shows an example for the colour scheme which applies to the scales in the following figures. The range of the scales differs from Shot to Shot but the colour distribution stays the same.

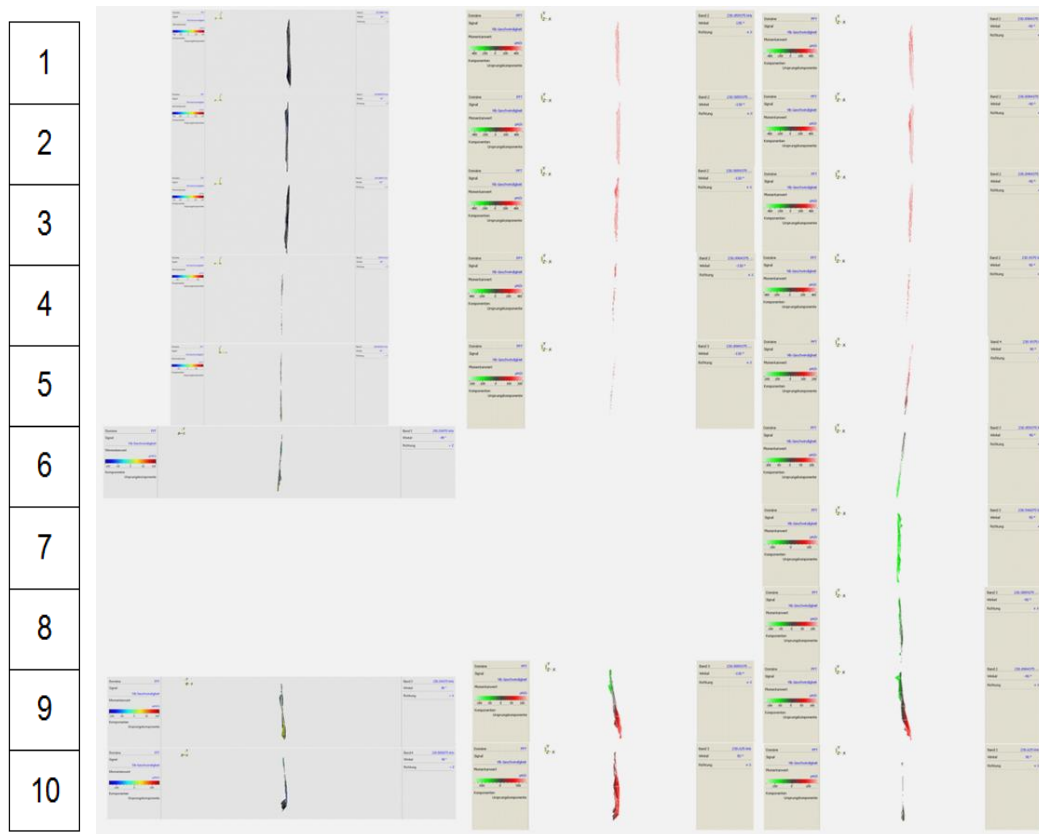


**Figure 20: Scale of instantaneous value (Momentanwert) for surface deflection in  $\mu\text{m/s}$**



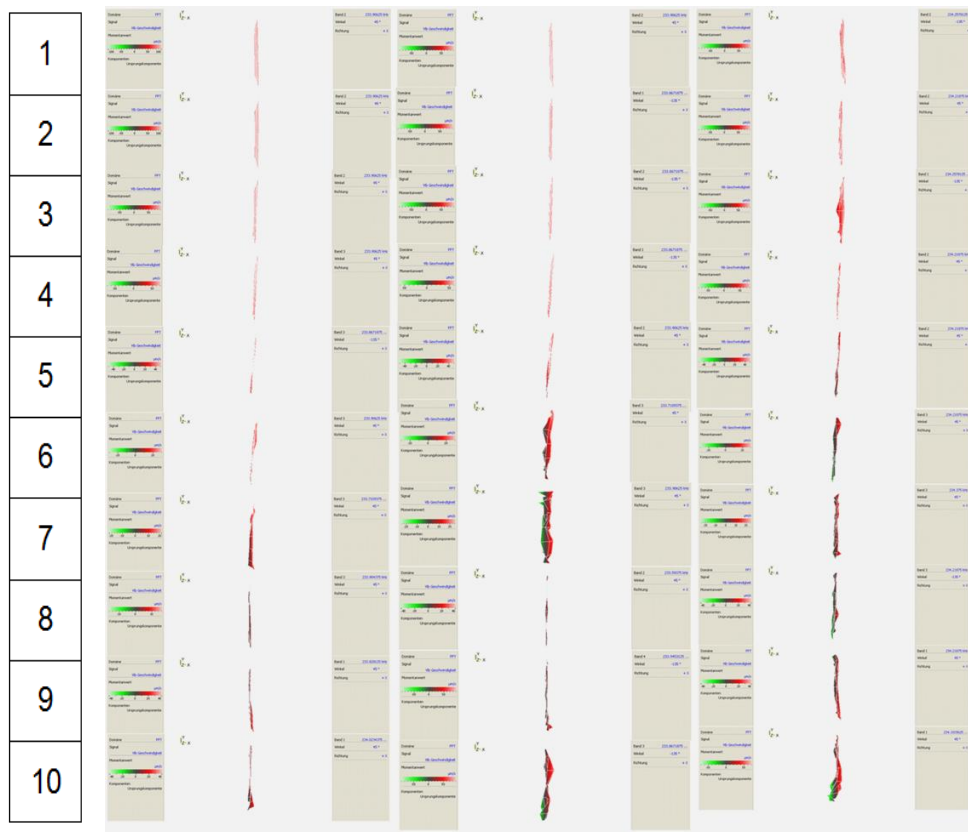
**Figure 21: Sample 1 at 228 kHz side view oscillation- from left to right: Row 1, Row 2, Row 3**

Figure 21 shows the oscillation of Sample 1 at approximately 228 kHz. Following the Shots from the top down to the bottom we see the trend of the deformation of the surface from the centre to the edge. In the centre the surface depicted as a plain moves parallel from one side to the other. This behaviour can be seen in each one of the three rows. In the fourth Shot in Row 1 on the left an inclination to the left starts to develop. In the other two rows the angle of the inclination is lower than in Row 1. In the lower middle section of the rows (Shot 7) the angle changes back to a plane oscillation. From Shot 7 to 10 the inclination develops back to the right so that a bulge is formed. This tendency can also be seen in Row 2 and 3 but not as distinctively as in Row 1. Here the inclination is lower and changes faster into a plane vibration.



**Figure 22: Sample 1 at 230 kHz side view oscillation- from left to right: Row 1, Row 2, Row 3**

In Figure 22 we see the oscillation trend of Sample 1 from the centre to the edge at approximately 230 kHz. Here the Shots 7 and 8 in Row 1 and the Shots 6 to 8 in Row 2 are left blank because the frequency bands do not show outstanding peaks for these areas. As in Figure 21 an inclination is recognisable. In Row 3 one can see its start in Shot 4 and 5 and ending in the last one. Here the oscillation is plain again as in the centre of the disc. The bulge seen in Row 3 is similar to the one in Figure 21. In Row 1 and 2 the last Shots at the edge of the disc show a more sloping position than the last one in Row 3. Since the colour gradient in both Shots 9 in Row 2 and 3 changes from the positive green side area into the negative red area in one image one can assume a bend crossing the zero line during the vibration. Same can be seen in Shot 6 in Row 3 running in the positive direction. Therefore a part of the bulge lies in the positive deflection area. Basically Figure 21 and Figure 22 show similar results for the deflection trend at 228 kHz and 230 kHz for Sample 1.



**Figure 23: Sample 2 at 234 kHz side view oscillation- from left to right: Row 1, Row 2, Row 3**

For Sample 2 every frequency band contains an outstanding peak at 234 kHz. Therefore the rows in Figure 23 are complete. Here we see the oscillation trend for Sample 2 at 234 kHz. Again three rows of snap-shots - measured  $70^\circ$  to  $90^\circ$  apart from each other- are compared. The Shots in the three rows do not show a noticeable deformation. There is a small inclination angle in Row 2 and Row 3 in Shot 10. As seen in Figure 22 the colour gradient of the plain shows a bend crossing the zero line. Apart from that the three rows of Sample 2 show minor similarities to Sample 1 as the bulge in direction of positive deflection is not as distinctive.

Figure 24 and Figure 25 show the oscillation trend for Sample 3 at approximately 228 kHz and 234 kHz. In Figure 24 again two Shots are missing- Shot 9 in Row 1 and Row 2. Here all three rows show similar occurrences. Starting in the centre of the sample the surface moves parallel from one to the other position. At Shot 4 the inclination in positive direction starts to develop. After a plane oscillation the trends again lead to a inclination in negative direction. This way a bulge is formed again similar to the one in Figure 21 and Figure 22. The trends seen in Figure 24 in Row 1, Row 2 and Row 3 at 228 kHz resemble each other the most in comparison to the other figures.

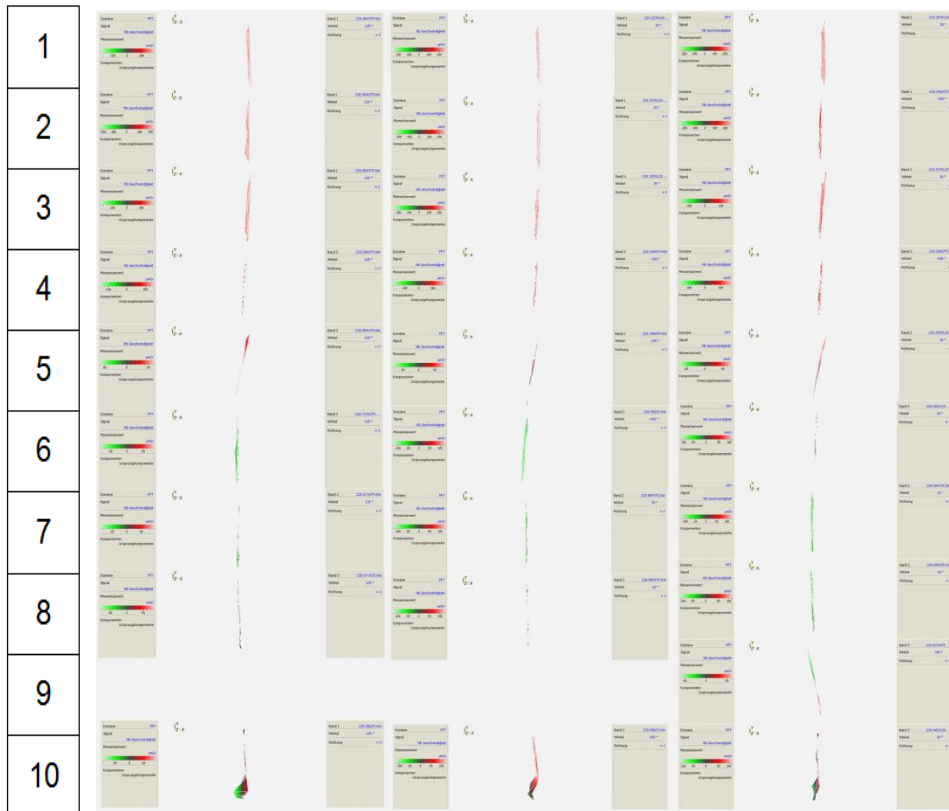


Figure 24: Sample 3 at 228 kHz side view oscillation- from left to right: Row 1, Row 2, Row 3

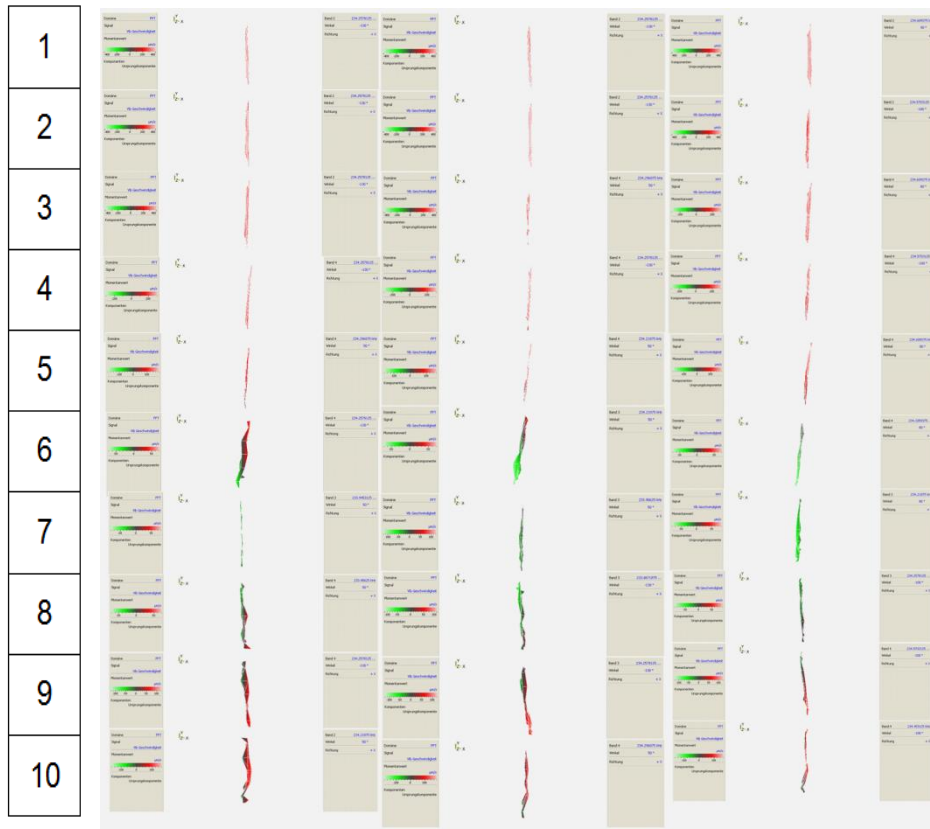


Figure 25: Sample 3 at 234 kHz side view oscillation- from left to right: Row 1, Row 2, Row 3

In Figure 25 all three rows are complete. Row 2 sticks out due to a more distinctive bulge in the second section. Row 1 and Row 3 show more parallel deflections. Basically Figure 24 and Figure 25 show a similar trend in the respective rows. The bulge in Row 1 and 3 is a little more shallower than in Row 2. Apart from that the deflection in the centre of Sample 3 stays plain until Shot 4 or 5 as seen in the figures before.

As the frequencies listed in Table 3 are located closer together the discs show similar oscillation behaviour around this area which can be seen in the form and position of the bulge. Tendencies are recognisable. All three discs share similar oscillation gradients. The inner part of the surface is plain and flat while proceeding to the edge of the disc a wave is seen forming a bulge in the second half of the radius. The previous figures are compared to the results obtained from the modal analysis done in *ANSYS Workbench*.

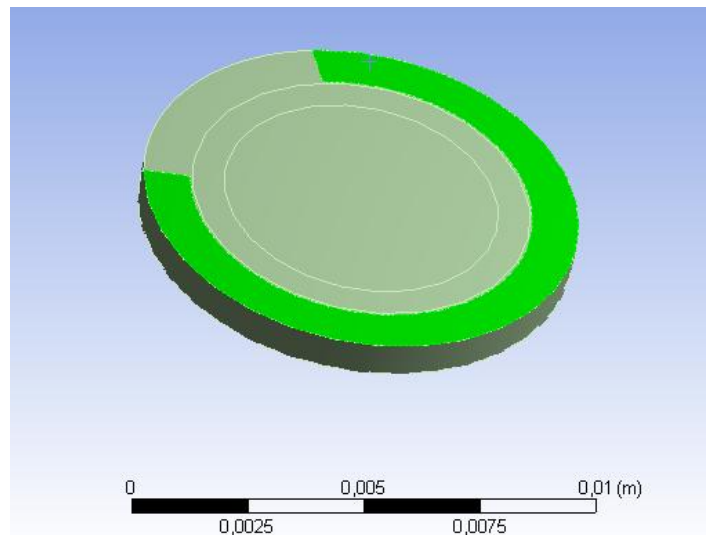
### 5.1.2 FEM simulation of the piezoelectric ceramic

The simulation done in *ANSYS Workbench* is a modal analysis. The model used is a simple disc with the measures of the real samples. In reality the discs are enclosed almost entirely with silver electrodes of 10  $\mu\text{m}$  thickness. In the simulation the electrodes were imprinted on the surface of the disc setting the pattern. There is no definition of additional material on the surface. Previous tests showed that the vibration modes are highly influenced by the way the disc is supported. During the measurement the discs have been clamped at the rim omitting a small segment of about 77°. As discussed before, the discs had to be held down in order to apply voltage on the electrodes. For the simulation the contact area on which the fixation grips needed to be imprinted on the surface as well (Figure 26). On the top it takes the form of a discontinuous ring, on the bottom the circle in the centre serves as a marking. During the measurement the fixation would not be absolutely rigid in any direction (for this constraint *Fixed Support* would be the tool of choice). For the model one can only try to find an approach to measuring conditions in reality. Therefore the tool *Remote Displacement* was used. Here the displacement of a certain area or point can be indicated for up to six degrees of freedom in a limited flexible way. During the tests there were no rotations or displacements in horizontal direction. Only in vertical direction the displacement was set to 0 m. All other parameters were left to free movement.

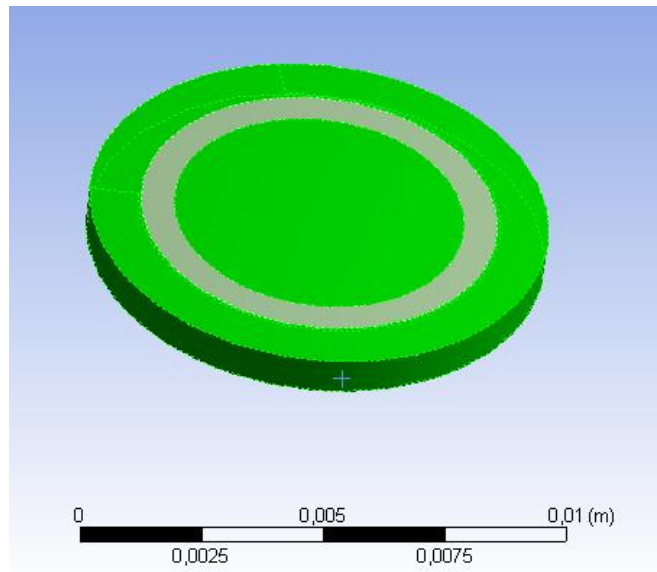
In *Analysis Settings* the general requirements for the simulation can be set. The range between 0 kHz and 300 kHz was chosen. After several calculations changing and adapting the number of modes as for the measurement it was clear that there would be about 30 noticeably different modes the software could find. In some cases they only differ by their orientation. Due to the fixation for some modes the results are asymmetrical.

To include the influence of the voltage applied during the real measurement the tool *Voltage* was used twice in this model, each representing the potential applied to an electrode for a defined face. The bigger electrode on top of the disc enclosing the lateral face was set approximately to 1,36 V (same value used for measurement), the other electrode was set to 0 V.

Finally the last conditions for the piezoelectric body were defined. Using a tool of the same name which is only available by installing the *Piezo-Extension* parameters like the polarisation axis, permittivity constant, piezoelectric matrix relating stress/electric field, relative permittivity, anisotropic permittivity matrix and piezoelectric matrix. Density and anisotropic elasticity have been defined in *Engineering Data* as mentioned above (Chapter 4.4). After running the simulation one can choose to see the individual modes by selecting the found natural frequencies in the diagram, right click and choosing *Create Mode Shape Results*. For every natural frequency a *Total Deformation* unit appears in the project tree. By solving them the vibration modes are calculated. In Figure 26 we see the model of the piezoceramic disc used for the simulation. The highlighted green area marks the position of the vertical fixation. This serves as the pendant to the clamping performed by the top plastic sheet (third sheet) shown in Figure 9.



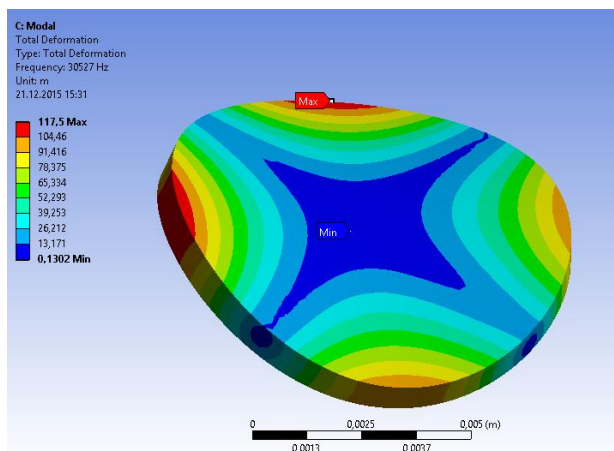
**Figure 26: Model of the disc for simulation and position**



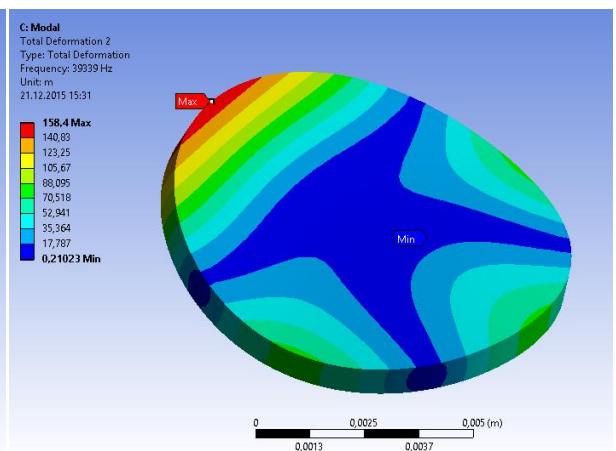
**Figure 27: Electrodes (green) separated by an annular omission (grey)**

Figure 27 shows the form of the two electrodes on the piezoceramic samples. The smaller electrode lies in the centre of the discs and is separated from the larger electrode by an annular omission. The larger electrode also fully covers the bottom of the disc.

Below the different mode shapes found by *Modal Analysis* in *ANSYS Workbench* are listed and discussed. Their spatial orientation correlates with the orientation in Figure 26 and Figure 27. The area which is not fixed vertically during the measurement lies in the top left corner of the following figures. The coloured scales in the figures show exaggerated values to visualise the minimal deformation. The minimum and the maximum value of the scales are written in the labelling of the figures.



**Figure 28: Mode 1 - 30,53 kHz (Min 0,1302 m; Max 117,5 m )**



**Figure 29: Mode 2 - 39,34 kHz (Min 0,210 m; Max 158,4 m )**

Figure 28 and Figure 29 show two similar modes at 30,53 kHz and 39,34 kHz. The mode in Figure 29 is a rotated version of the mode in Figure 28. The maximum deflection in Figure 29 lies at the front side of the disc, where no vertical fixation is placed.

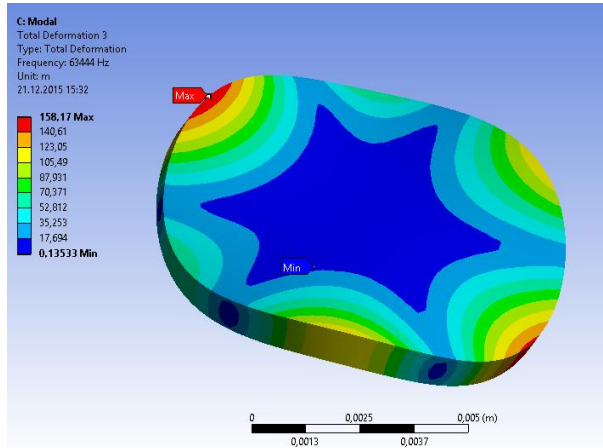


**Figure 30: Mode 3 - 63,44 kHz (Min 0,135 m; Max 158,2 m )**

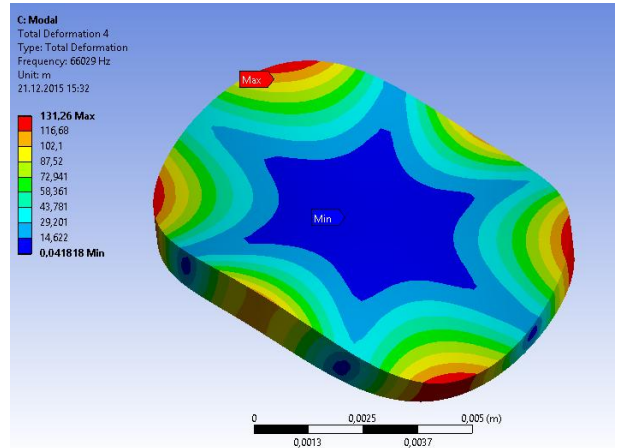


**Figure 31: Mode 4 - 66,03 kHz (Min 0,042 m; Max 131,3 m )**

Again Figure 30 and Figure 31 show similar mode shapes differing by a small rotation. The two frequencies at 63,44 kHz and 66,03 kHz lie close together. In both figures we see 6 maxima of deflection at the edge of the disc.

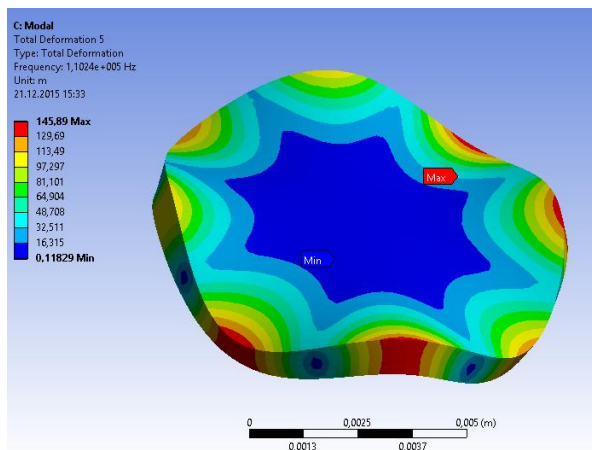


**Figure 32: Mode 5 - 110,24 kHz (Min 0,118 m; Max 145,9 m )**

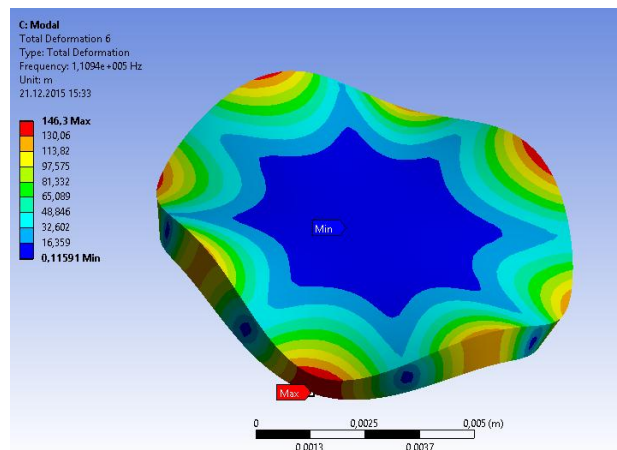


**Figure 33: Mode 6 - 110,94 kHz (Min 0,116 m; Max 146,3 m )**

The frequencies of the modes in Figure 32 and Figure 33 lie close together at 110,24 kHz and 110,94 kHz as well as the minima and maxima of the scales. Again the only difference is the spatial orientation.

The brimming of the egde is more noticeable than in the last pair of modes.

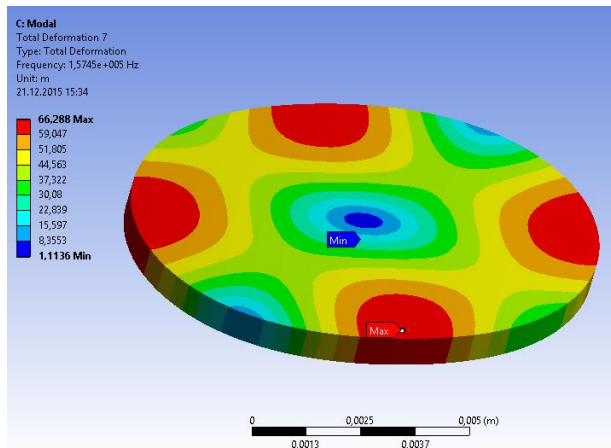


**Figure 34: Mode 7 - 157,45 kHz (Min 1,11 m; Max 66,29 m )**

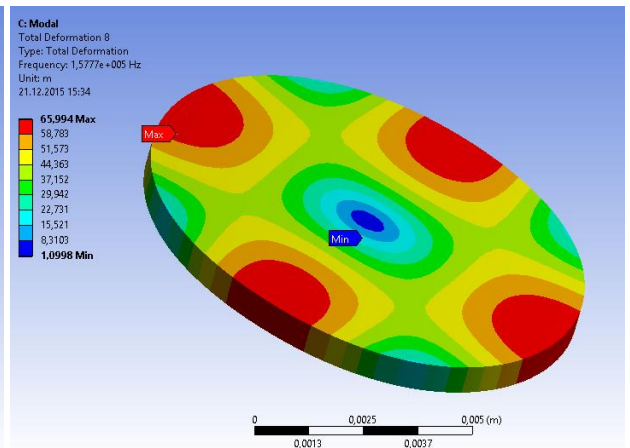


**Figure 35: Mode 8 - 157,78 kHz (Min 1,10 m; Max 66,10 m )**

For the modes in Figure 34 and Figure 35 the same description as for the last two applies. Both modes lie close together at 157,45 kHz and 157,78 kHz and show a similar shape. This time the modes are both flat with smaller deflections in the centre and at the edge of the disc. During oscillation deflections occur mostly in horizontal direction in both cases. This is also reflected in the magnitude of both minima and maxima of deflection at around 1,1 m and 66 m (exaggerated values) in comparison to the others at around 0,05 m and 140 m.

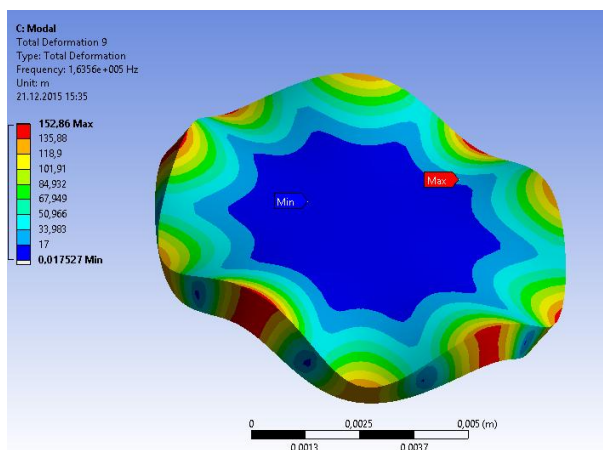


**Figure 36: Mode 9 - 163,56 kHz (Min 0,018 m; Max 152,86 m )**

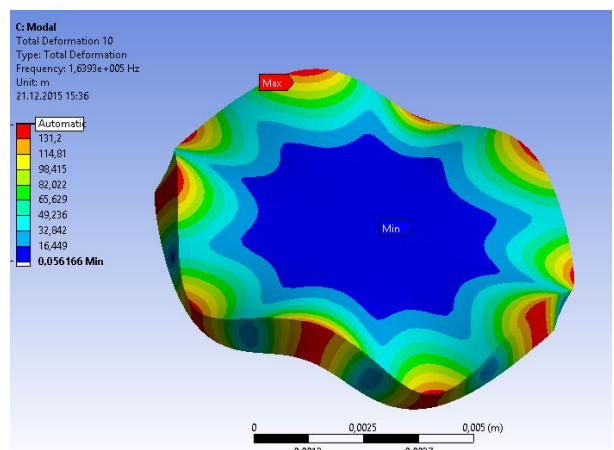


**Figure 37: Mode 10 - 163,93 kHz (Min 0,06 m; Max 131,2 m )**

In Figure 36 and Figure 37 Modes 9 and 10 show similar shapes and more maxima of deflection at the edge than in Figure 32 and Figure 33. Again the frequencies are almost identical.

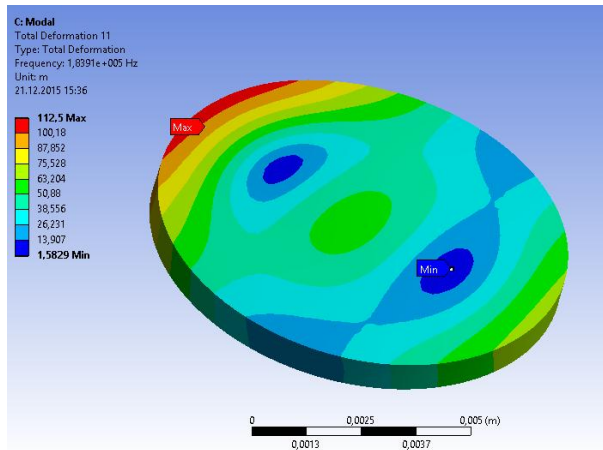


Figure 38: Mode 11 - 183,91 kHz (Min 1,58 m; Max 112,5 m )

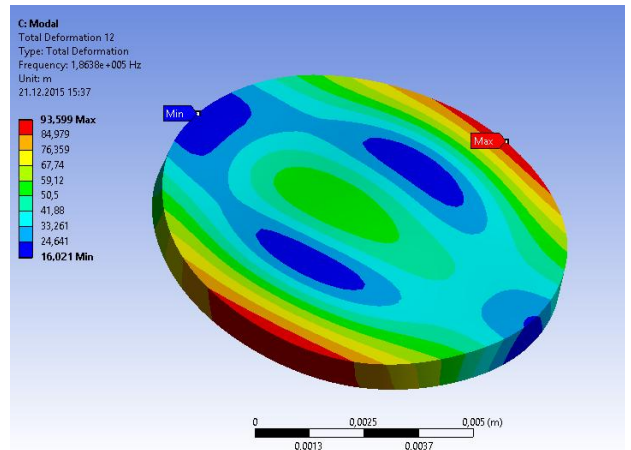


Figure 39: Mode 12 - 186,38 kHz (Min 16,02 m; Max 93,6 m )

As in Figure 34 and Figure 35 we see a plane mode shape in both Figure 38 and Figure 39. The position of the deflection maxima differs by a rotation of about 90°. In Figure 38 the maximum deflection lies at the front of the disc, when no clamping is applied. In Figure 39 the minimum lies at this point. So far the minima were always situated in the centre of the disc. Here the locations of minimum and maximum deflection lie symmetrically distributed around one axis leading towards the area of the disc where no clamping is applied. Around this axis in Figure 38 and Figure 39 we only have two minima and one maximum of deflection around the centre.

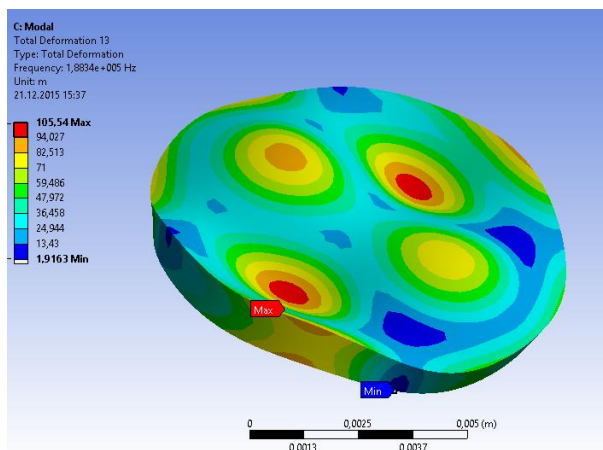


Figure 40: Mode 13 - 188,34 kHz (Min 1,92 m; Max 105,54 m )

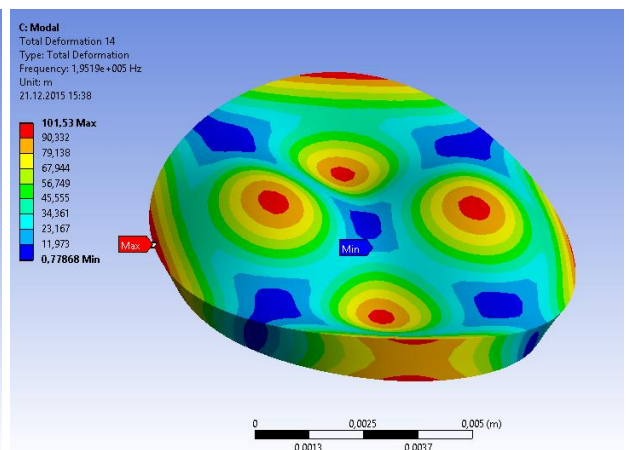
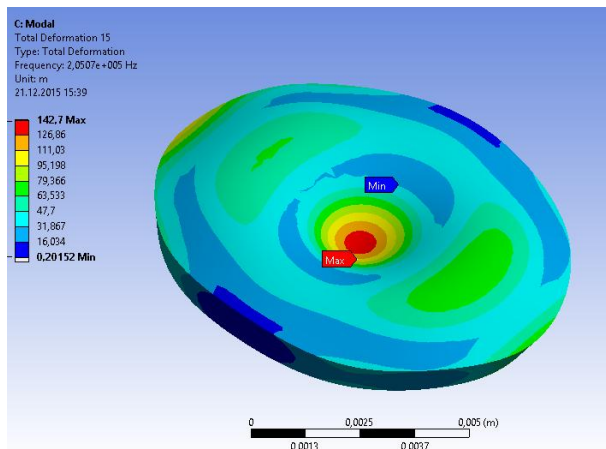


Figure 41: Mode 14 - 195,19 kHz (Min 0,78 m; Max 101,5 m )

The mode shapes in Figure 40 and Figure 41 can be described equally to Mode 11 and 12 in Figure 38 and Figure 39. Similar to these two here one can see a distribution of deflection minima and maxima symmetrically around an axis leading to the clamping-free area.

In contrast to the last two figures here the mode shapes show two minima and maxima in the centre.



**Figure 42: Mode 15 - 205,07 kHz (Min 0,20 m; Max 142,7 m )**

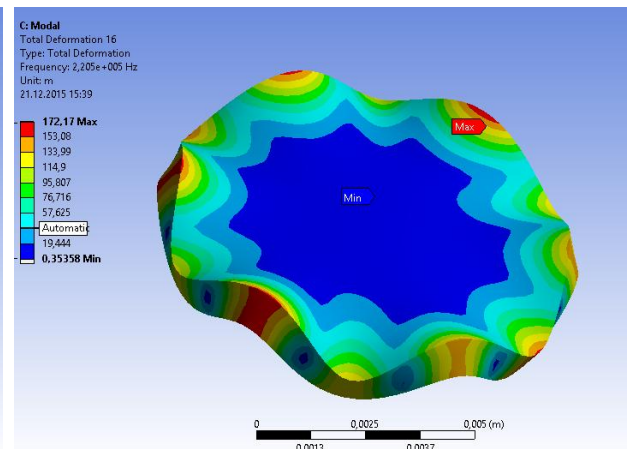


**Figure 43: Mode 16 - 220,50 kHz (Min 0,35 m; Max 172,17 m )**

Mode 15 in Figure 42 is the first one to show a pointed deflection maximum in the centre of the disc. Again symmetry around an axis can be seen.

Mode 16 in Figure 43 shows similarities to Mode 17 in Figure 44. The brimming of the edge is caused by alternating maxima and minima of deflection. These two modes are the nearest to the results of the measurements done with the vibrometer. Later Mode 17 is examined more in detail for comparison with the measurement results.

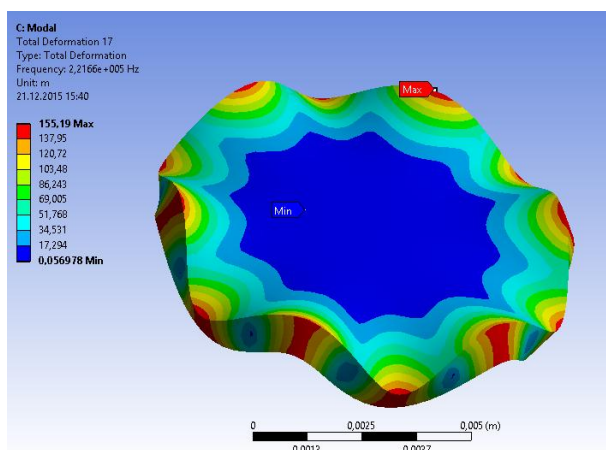


**Figure 44: Mode 17 - 221,66 kHz (Min 0,06 m; Max 155,2 m )**

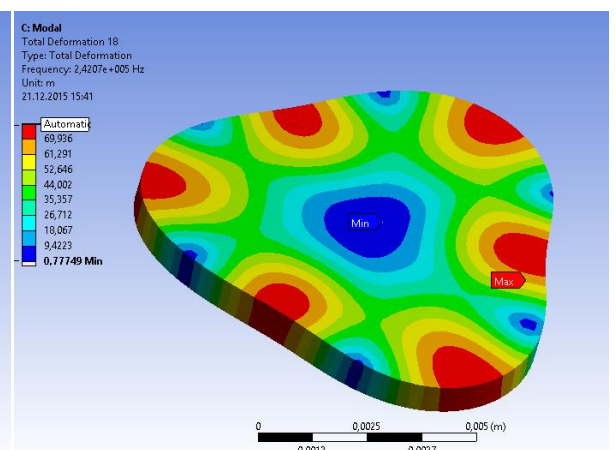


**Figure 45: Mode 18 - 242,07 kHz (Min 0,78 m; Max 69,94 m )**

Figure 45 and Figure 46 again show plane mode shapes as seen in Figure 34 and Figure 35 with 6 instead of 4 maxima and minima of deflection at the rim of the disc. Again both frequencies lie very close together. As for Mode 7 and 8 deflections occur mostly in horizontal direction.

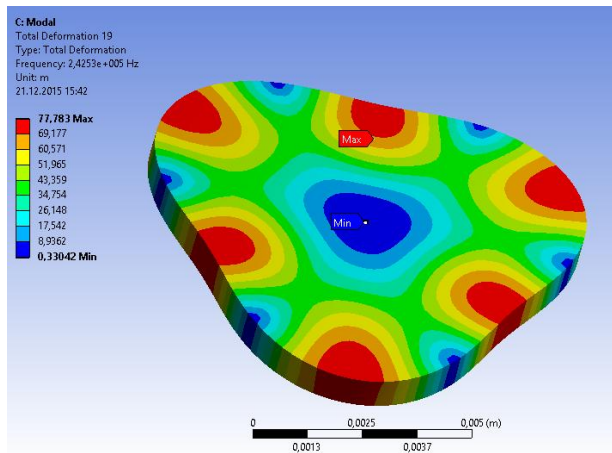


**Figure 46: Mode 19 - 242,53 kHz (Min 0,33 m; Max 77,78 m)**

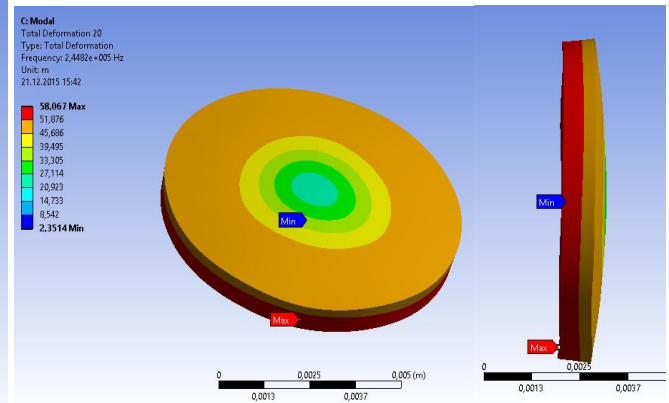


**Figure 47: Mode 20 - 244,82 kHz (Min 2,35 m; Max 58,07 m)**

Figure 47 shows a similar oscillation mode as in Figure 42. Here the minimum deflection lies in the centre of the disc, the maximum at the outer rim.

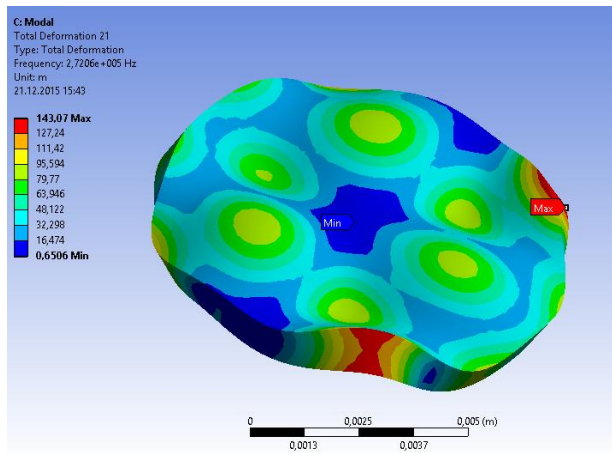


**Figure 48: Mode 21 - 272,06 kHz (Min 0,65 m; Max 143,07 m)**

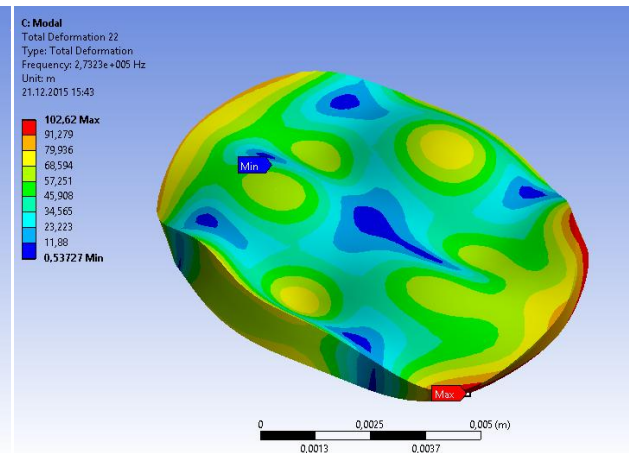


**Figure 49: Mode 22 - 273,23 kHz (Min 0,54 m; Max 102,62 m)**

Modes 21, 22 and 23 in Figure 48 to Figure 50 lie close together regarding their frequencies at 272 kHz, 273 kHz and 276 kHz. They show similar positions of maxima and minima with contrary characteristics.

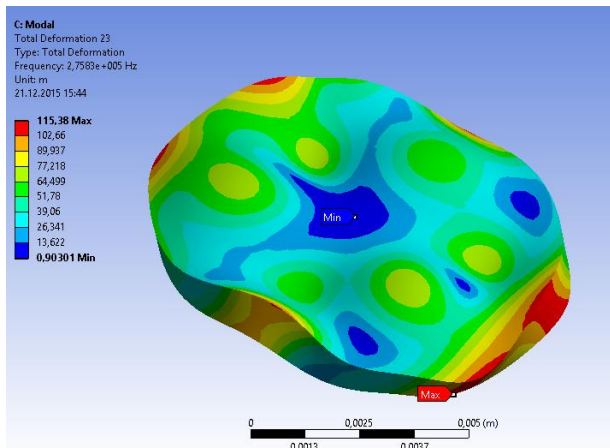


Figure 50: Mode 23 - 275,83 kHz (Min 0,90 m; Max 115,38 m )

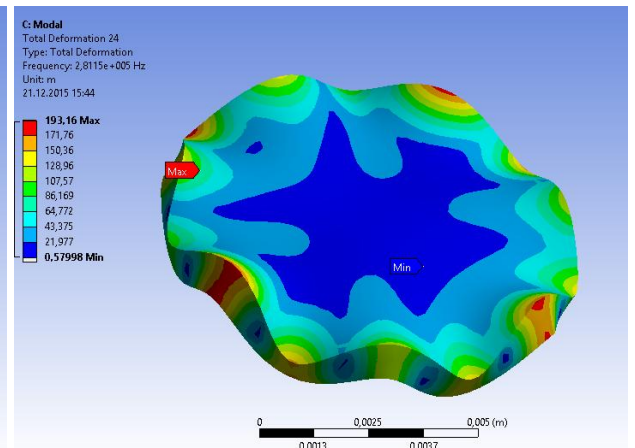


Figure 51: Mode 24 - 281,15 kHz (Min 0,58 m; Max 193,16 m )

Looking at Figure 51 and Figure 52 we see similar mode shapes and frequencies. Mode 24 in Figure 51 has higher values for minimum and maximum deflection than Mode 25 in Figure 52. Both show symmetrically distribution around an axis leading to the front of the disc where no clamping is applied.

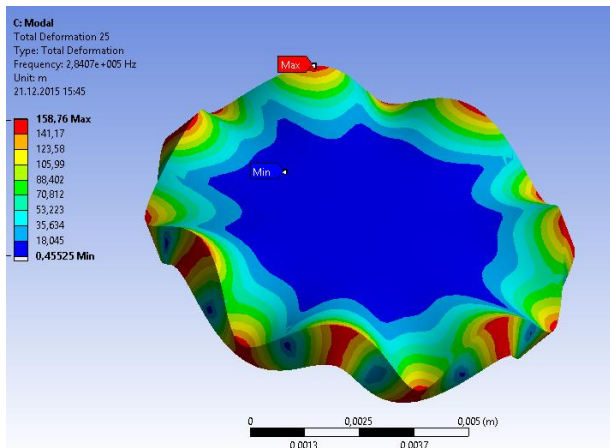


Figure 52: Mode 25 - 284,07 kHz (Min 0,455 m; Max 158,76 m )

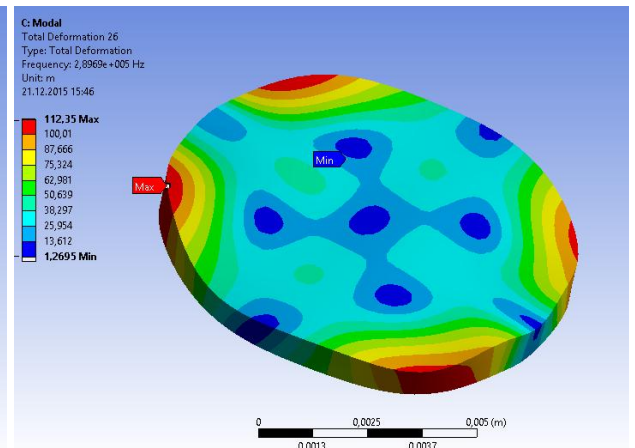


Figure 53: Mode 26 - 289,69 kHz (Min 1,27 m; Max 112,35 m )

Figure 53 shows an almost plane mode shape as seen in Figure 34 and Figure 35 as well as in Figure 45 and Figure 46 and symmetrical distribution of the maxima and minima. Here in the centre we find 5 minima and 4 maxima positions.

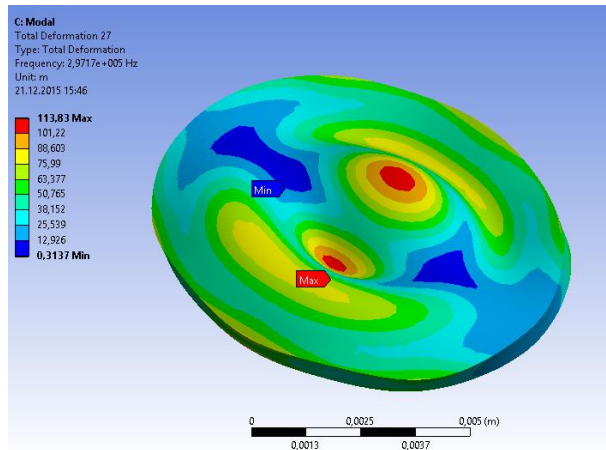


Figure 54: Mode 27 - 297,17 kHz (Min 0,314 m; Max 113,83 m )

Figure 54 shows the last mode found by *Modal Analysis* in *ANSYS Workbench* at 297 kHz. In the centre of the disc two maxima of deflection expanding in opposite directions and two elongate minima are found. Regarding its shape this mode is unique in this simulation.

### 5.1.3 Comparison of the experimental results and FEM simulation of the modal analysis of a single piezoelectric disc

PI Ceramic GmbH provides information also regarding the oscillation behaviour of their products. A document by PI Ceramic GmbH [57] (see Figure 55) describes which resonance frequencies are to be found (with  $N_p$  being the frequency coefficient of the planar oscillation of a round disk and  $N_t$  being the frequency coefficient of the thickness oscillation of a thin disk polarised in the thickness direction).

Shape	Oscillations	
	Type	Mechanical deformation
<b>Thin disk</b> 	radial	
	thickness	

Series resonance frequency	Electrically induced displacement (small signal)	Mechanically induced voltage (small signal)
$f_s = \frac{N_p}{OD}$	$\Delta OD = \frac{d_{31} OD}{TH} U$	
$f_s = \frac{N_t}{TH}$	$\Delta TH = d_{33} U$	$U = -\frac{4g_{33} TH}{\pi OD^2} F_3$

Figure 55: Detail oscillation specifications for thin disc piezoceramic elements [57]

Using the equations for  $f_s$  for radial and thickness mode one receives the following results:

#### Values for PIC181

$$N_p = 2270 \text{ Hz} * m$$

$$N_t = 2110 \text{ Hz} * m$$

$$OD = 9,5 \text{ mm}$$

$$TH = 0,8 \text{ mm}$$

$$f_s = \frac{N_p}{OD} = \frac{2270 \text{ Hz} * m}{9,5 \text{ mm}} = 238,95 \text{ kHz} \quad (26)$$

$$f_s = \frac{N_t}{TH} = \frac{2110 \text{ Hz} * m}{0,8 \text{ mm}} = 2637,5 \text{ kHz} \approx 2,64 \text{ MHz} \quad (27)$$

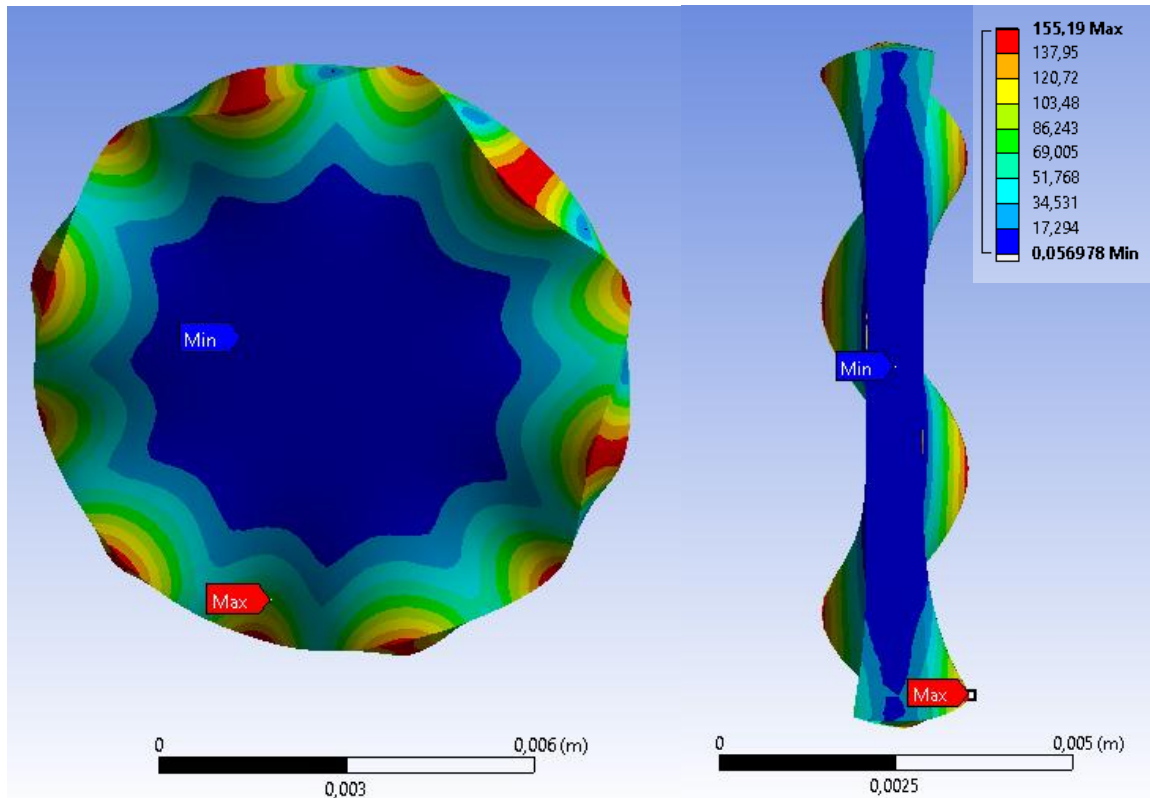
The analysis done with the vibrometer only lie in a range between 0 and 300 kHz. The resonance frequency for radial oscillation can be compared to the results given by measurement and simulation.

Table 4: Overlapping results of measurement and simulation for natural frequencies

Measurement [kHz]	Simulation [kHz]	Crossover [kHz]
	30,527	
	39,339	
	63,444	
65	66,029	65
75	110,24	
	110,94	
	157,45	
130	157,77	
	163,56	
	163,93	
	183,91	
185	186,38	185
190	188,34	190
200	195,19	
205	205,07	205
210	220,5	
220	221,66	220
228	242,07	240
230	242,53	
234	244,82	245
240	272,06	
245	273,23	
248	275,83	
280	281,15	280
285	284,07	285
	289,69	
	297,17	

The last column in Table 4 shows the equal results of measurement and simulation. The value 238,95 kHz which one receives from the equation for  $f_s$  for radial oscillation also falls in this domain as it lies near to 240 kHz. Most of the natural frequencies found by the vibrometer appear as a result of the simulation.

As shown in Table 4 for the most current frequencies received through measurement (228 kHz, 230 kHz and 234 kHz) no equal value is found. According to Cadfem Support Service [58] in *Modal Analysis* the frequencies can be dislocated tolerably but have to show similar mode shapes for compliance. For evaluation the shapes of the modes at the three frequencies as well as around 220 kHz are compared.



**Figure 56: Mode 17, 222 kHz, top view and cross section at min. deflection**

In Figure 56 and Figure 57 we see Mode 17 of the modal analysis done in ANSYS. The centre is flat compared to the outer rim of the disc similar to the trend seen in Figure 21 to Figure 25. Also the corrugation at the rim forms deformations on the surface, which can be seen in Shots taken during the measurement. Another similarity appears at the last third of the radius- deformation starts at the beginning of the last third and changes to a flat trend at to the edge. This tilt at the edge can be compared to the deformation depicted as a bulge in the figures above (Figure 21 to Figure 25).

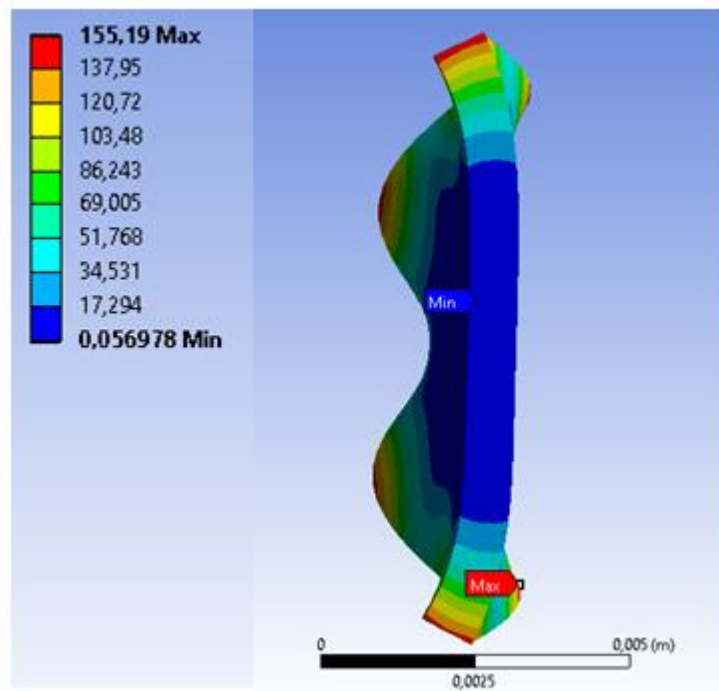


Figure 57: Mode 17, 222 kHz, cross section at max. deflection and exaggerated scale in [m]

As seen in Figure 21 to Figure 25 around the 7th to 10th Shot a displacement in vertical (in the figures its horizontal) direction can be seen. In Figure 22, Figure 23 and Figure 25 there is also a tilt at the end of the rows, in Figure 23 and Figure 25 already beginning at Shot number 7. Looking at Shot 10, Row 2 in Figure 25 (Detail view in Figure 58) it is possible to see how the surface of the disc (Sample 3) tilts at about 234 kHz resulting in a slope back in the negative direction.

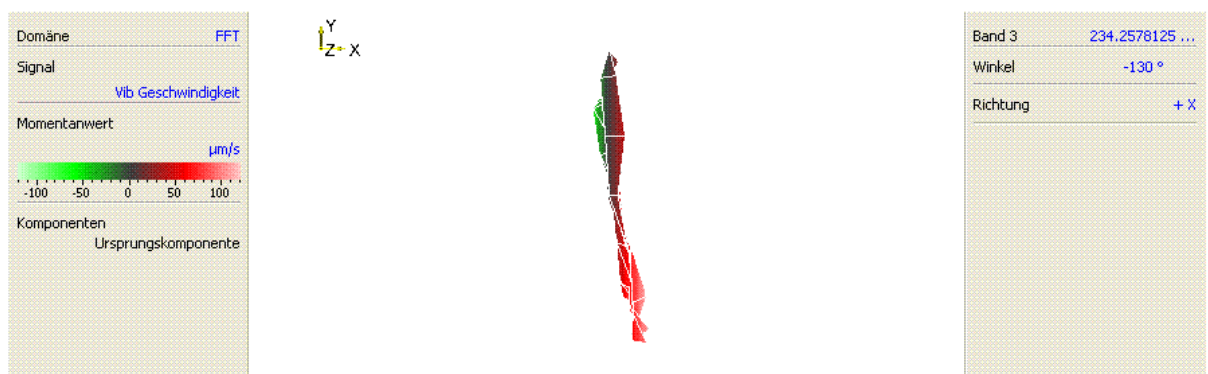


Figure 58: Sample 3 at 234 kHz, Row 2 (90°), Shot 10

There is a difference regarding the inclination of the surface at the edge of the disc. In Figure 57 unlike the results of the measurements the simulation shows no back slope at the end of the bulge. During the measurements this slope could have been caused by lateral restraints due to the plastic sheets holding the samples. The restraints may have resulted in a slight compression counteracting the horizontal expansion of the discs. For the simulation only horizontal constraints for displacement have been considered.

## 5.2 Instantaneous values at individual surface points of a single piezoceramic disc

The self-imposed grid provides instruction for the measurement sequence. It is possible to read the instantaneous values from selected surface points lying at the grid nodes obtained from the same measurements as in Chapter 5.1. The grid was taken into the simulation model for each section with the result that the values can be compared directly at the same position. As the three samples come from the same batch, it is expected that their parameters lie close together. Therefore there was only one model built which will be used for comparison with the three real piezoceramic discs.

### 5.2.1 Measurement

Following the findings of the previous chapter the results are narrowed down to the three natural frequencies in Table 3 from the previous chapter. For an accurate comparison of instantaneous values a grid is defined for the execution of the analysis. The grid applied for the vibrometer measurements is shown in Figure 59.

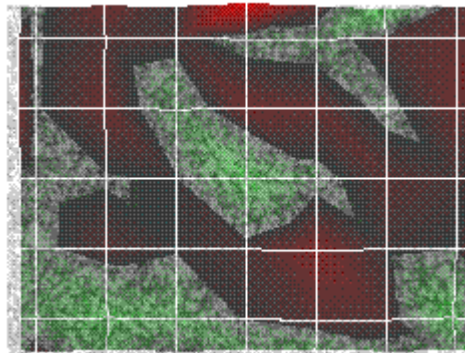


Figure 59: Grid for measurement (Sample 3, 234 kHz, Row 2, Shot 8)

It contains 35 measuring points set at the nodes serving as instruction for the PSV. The values have been read at eight phase angles in an interval of  $45^\circ$ , equally divided in a full oscillation. From this data pool the maximum deflection of the measurement is determined. With eight deflection values  $x_i$  and the corresponding phase angles  $\alpha$  the following Equations 28 to 30 are used to calculate the phase shifts  $\Delta\alpha$  and later the instantaneous values A.

$$x_i = A * \sin(\alpha_i + \Delta\alpha) \quad (28)$$

$$\frac{x_1}{x_2} = \frac{\sin(\alpha_1 + \Delta\alpha)}{\sin(\alpha_2 + \Delta\alpha)} = \chi \quad (29)$$

$$\Delta\alpha = -\arccos \left[ \frac{\cos(\alpha_1) - \chi \cos(\alpha_2)}{\sqrt{-2\chi \sin(\alpha_1) \sin(\alpha_2) - 2\chi \cos(\alpha_1) \cos(\alpha_2) + \sin^2(\alpha_1) + \cos^2(\alpha_1) + \chi^2 \sin^2(\alpha_2) + \chi^2 \cos^2(\alpha_2)}} \right] \quad (30)$$

With the calculated phase shifts the actual instantaneous values are found by using Equation 30. For each disc the results from the three rows are compared. The fluctuation between the results - aside from software-specific influences - indicates the acceptable range in which the simulation results may lie. According to their customer support service [59], PI Ceramic GmbH in Lederhose, Germany, had gained experience on simulation of their products. The results showed that the simulation model comes very close to reality if the results lie in a range of  $\pm 30\%$  to the measured values. As the single discs partially share some of the natural frequencies the following results are opposed to each other:

- Sample 1 and Sample 3 at approx. 228 kHz
- Sample 2 and Sample 3 at approx. 234 kHz
- Sample 1 at approx. 230 kHz

## 5.2.2 Simulation

The geometry has been adapted in order to be able to analyse the instantaneous values exact to the point. The grid pattern used for the vibrometer was also applied for the simulation to mark the relevant spots on the surface of the disc. The dimensions were derived from the proportion of the grid in the pictures. Imprinted on the top face the grid was placed from the centre of the disc to the rim (see Figure 60). In Figure 60 and Figure 61 we see the model used for the simulation in this chapter. The defined grid ranges from the centre of disc to the edge showing the same pattern used for the measurements. The form and the definition of the electrodes stays the same as described in the previous Chapter 5.1.2. The region at which the clamping was applied during measurements is marked as yellow area. A detailed depiction of the grid can be seen in Figure 61. Here the grey area is the free surface of the sample.

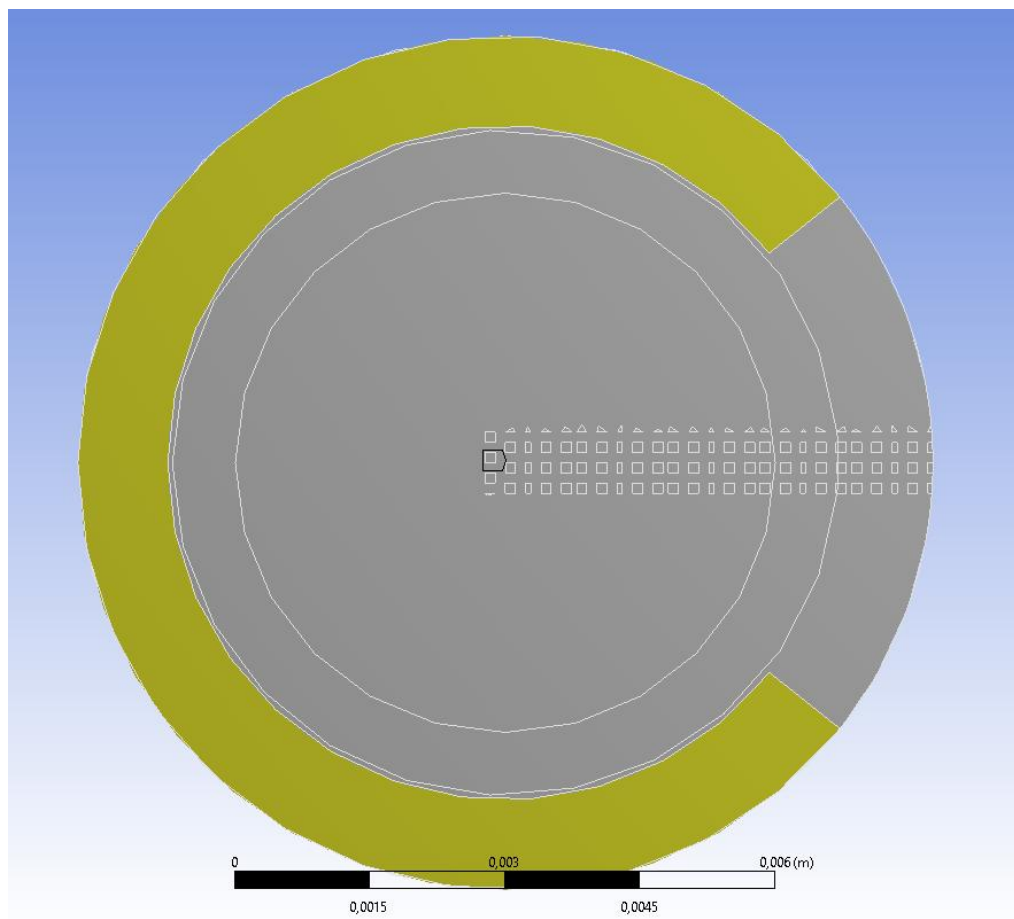
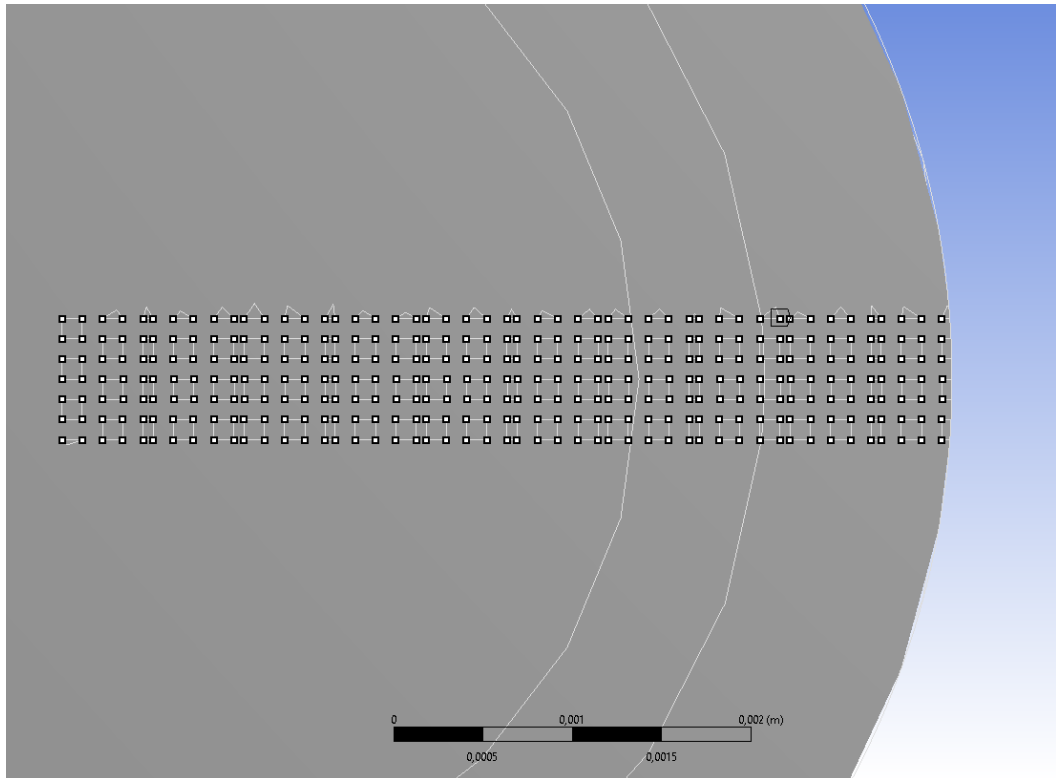


Figure 60: Disc with clamped area (yellow) and grid



**Figure 61: Closer view on grid - Named Selection at vertices**

First working with *Modal Analysis* the mesh was generated with specifications regarding the measures of the grid. It is finer near to the grid area due to the extraction settings used to imprint the grid. An alternative to the extraction tool would be using sketches and lines in the *DesignModeler* to create virtual topologies in *Modal Analysis*. The chosen method was to create *Named Selections* at the vertices, which one can select as geometry reference for the calculation. The nodes in the grid were traversed following the sequence repeating in each Shot as seen in Table 5:

**Table 5: Scanning sequence for nodes defined for vibrometer measurements**

1	2	11	16	21	26	31
4	3	12	17	22	27	32
6	5	13	18	23	28	33
8	7	14	19	24	29	34
10	9	15	20	25	30	35

The tool *Harmonic Response* enables harmonic analysis by stimulating a structure with a harmonic oscillation and setting similar constraints as in *Modal Analysis*. A modal analysis always precedes a harmonic analysis as the second one uses results of the first.

In *Harmonic Response* one can choose to analyse the oscillation either at the natural frequencies found by *Modal Analysis* or at self-declared frequencies. Also the shape of the harmonic oscillation can be analysed as the instantaneous value and phase angle are provided.

Here the same conditions as in Chapter 5 were set for *Remote Displacement*, *Voltage* and *Piezoelectric Body*. The frequency range was shortened to 50 kHz - 300 kHz. In the field *Solution Method Full* was chosen and *Constant Damping Ratio* was set to 0,15. Following the advice given by Cadfem Support Service [58] a damping ratio up to 0,15 would not affect the results in a negative way. It rather helps creating a setting for the simulation as close to reality as possible.

After calculation the instantaneous value could be displayed by using *Amplitude Frequency Response* in the *Solution* section of the project branch. Here geometry parts can be selected and scanned for the respective instantaneous values. Further one can define the frequency range for the analysis. In this work the exact frequencies are 228 kHz, 230 kHz and 234 kHz.

### 5.2.3 Results

The following figures show the similarities between the measured and simulated instantaneous values. Regarding the results described in the previous chapter the test objects are compared at similar frequencies shown in their respective frequency bands: Sample 1 and Sample 3 at 228 kHz, Sample 1 at 230 kHz and Sample 2 and Sample 3 at 234 kHz. The horizontal scale shows the number of the current Shot and the sequence number of the grid nodes.

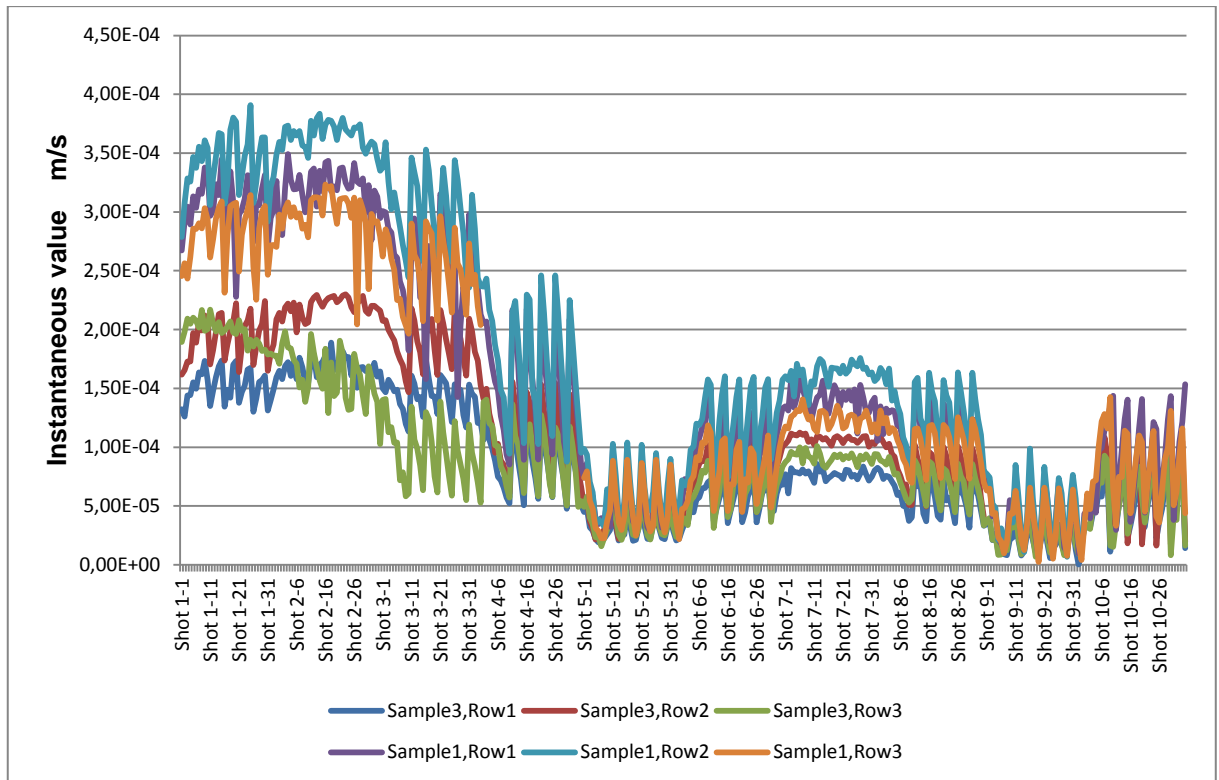


**Figure 62: Sample 1 and Sample 3 228 kHz**

Figure 62 shows the instantaneous values of Sample 1 and Sample 3 at 228 kHz. The trends of the three rows at about  $0^\circ$ ,  $90^\circ$  and  $180^\circ$  lie close together looking at a single disc. As there is a noticeable difference to the first 3 Shots, the trends converge at the end. Sample 1 at 230 kHz cannot be compared to another disc as too few peaks are found nowhere near enough to 230 kHz in Sample 2 and Sample 3. Here the trends for the first row at  $0^\circ$  and the second one at  $90^\circ$  are missing from Shot 6 to 8. In the first Shots again the proximity of the three series belonging to one disc can be seen but also higher instantaneous values at 230 kHz.

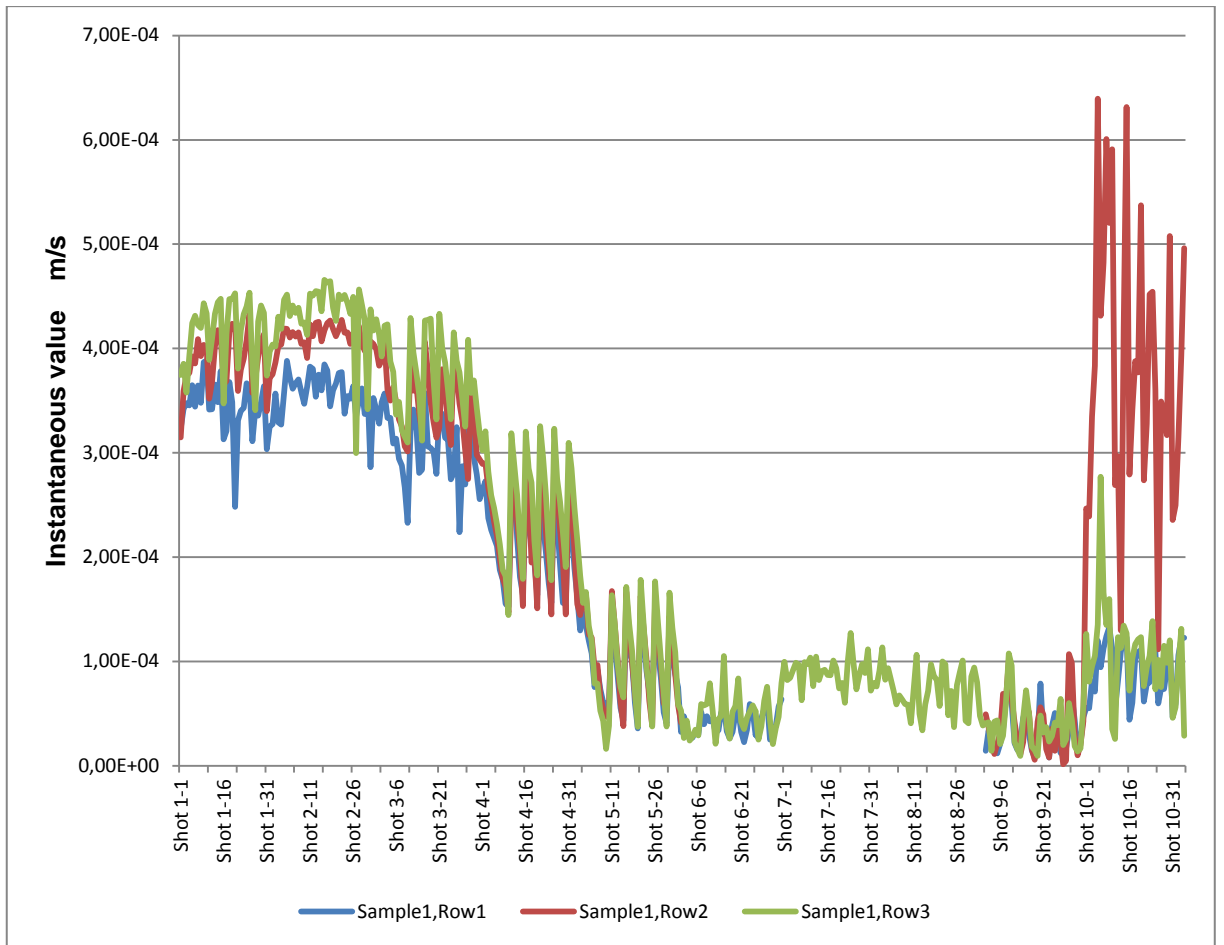
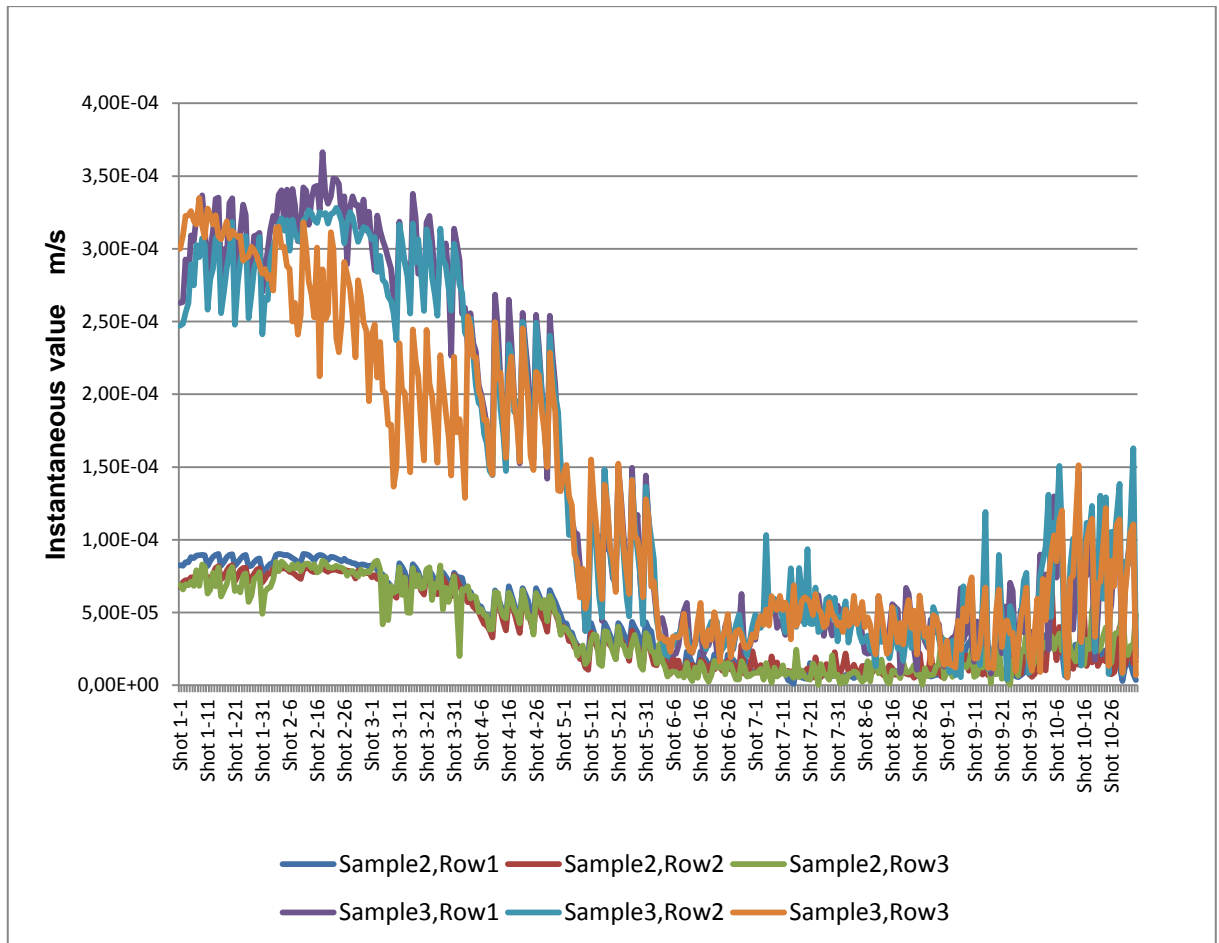


Figure 63: Sample 1 230 kHz



**Figure 64: Sample 2 and Sample 3 234 kHz**

Looking at Figure 64 the trends for Sample 2 and Sample 3 likewise greatly differ by a factor of 3 in the beginning. For Sample 3 there is also a deviation between the first/second and the third row in the second and third Shot.

Going into detail the measurements done under similar but not identical conditions feature resemblance in the shape of the trends but also in some places significant differences in value. Following the advice of the Cadfem Support Service [58] and PI Ceramic Customer Support Service [59] a range of  $\pm 30\%$  of the measurement results is defined for comparison with simulation results. For this purpose the highest and lowest instantaneous values for each of the three frequencies above are taken to calculate the limitation.

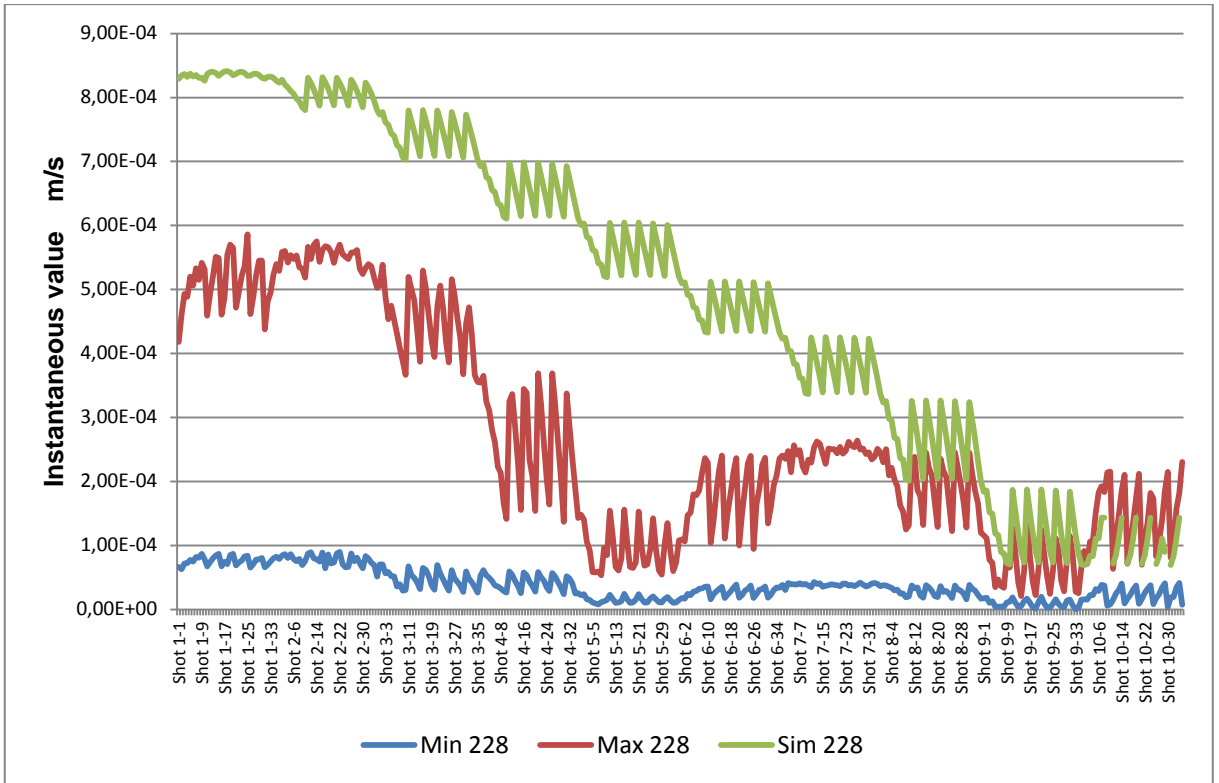


Figure 65: Measurement and Simulation 228 kHz, Sample 1 and 3

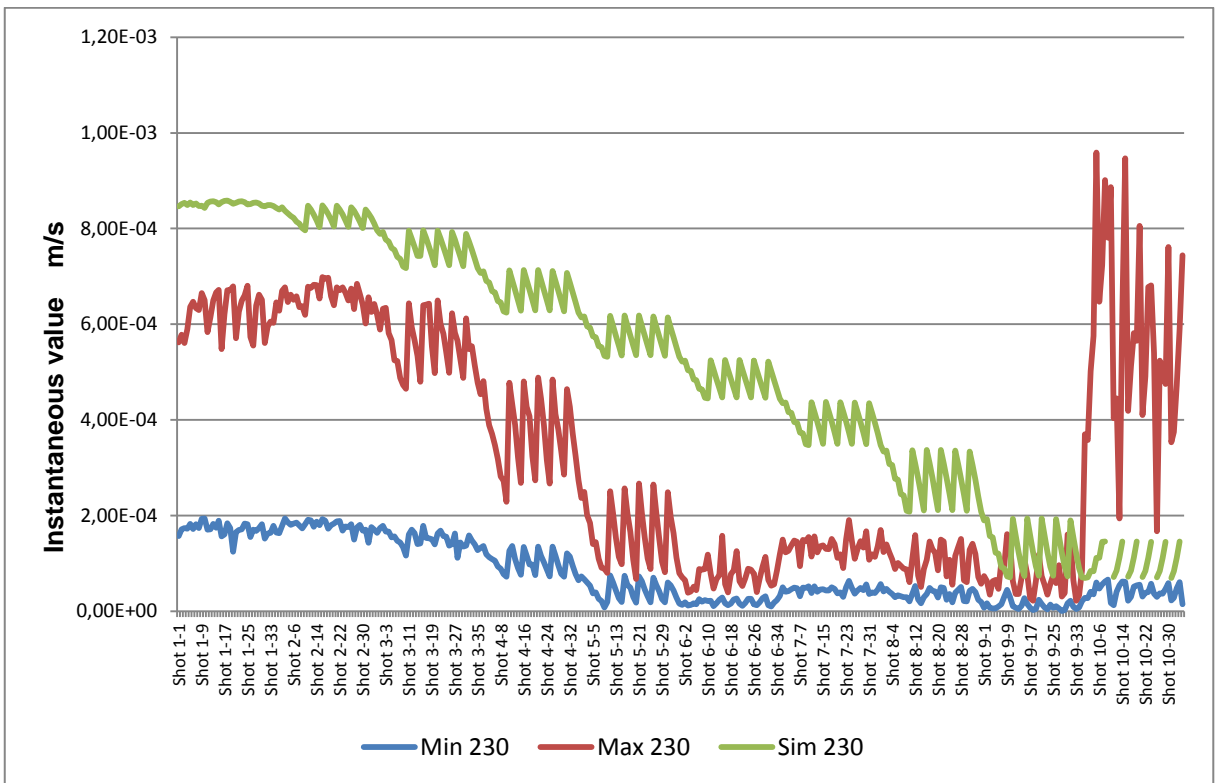


Figure 66: Measurement and Simulation 230 kHz, Sample 1

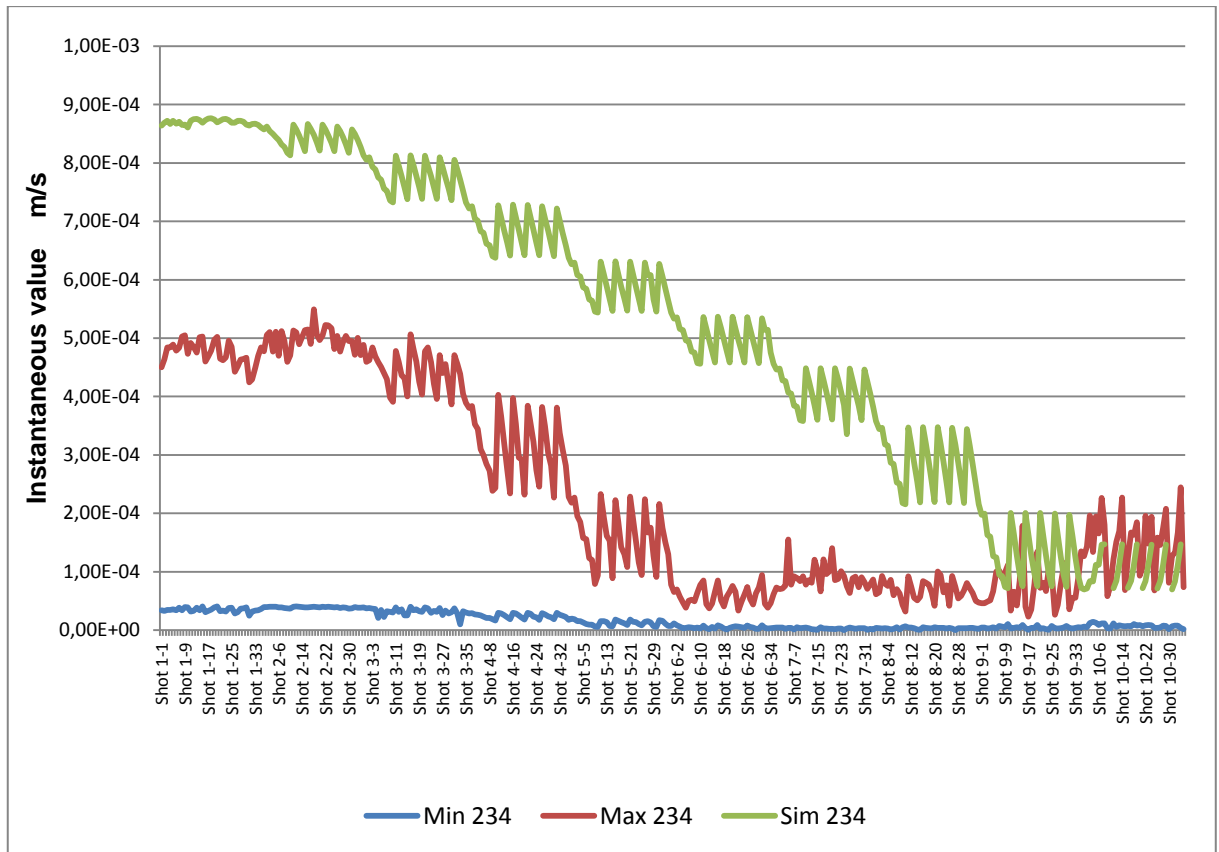


Figure 67: Measurement and Simulation 234 kHz, Sample 2 and 3

In Figure 65 to Figure 67 the maxima and minima of the instantaneous values for each frequency are shown in red and blue. The green trends show the simulation results. All three figures show a steadily decreasing green course lying above the limits set by the  $\pm 30\%$  of the measurement values. Only at Shot 9 and 10 (in Figure 65 beginning at Shot 8) the simulation approaches the measurement at the top boundary. The values partially differ by the factor 2 to 5. According to Cadferm Support Service [58] and PI Ceramic Customer Support Service [59] the results found by a model very close to reality would lie inside the  $\pm 30\%$ -limitation. The simulation comes close to the measurement but it is not ideal as the results show. Also adjusting the settings for *Remote Displacement* as parameter for the mounting pushed the values away from the maximum tolerable values.

The biggest deviation of instantaneous values is located in the centre of the discs and converges leading to the edge, where they meet. To reach better results the support in the centre needs to be defined more accurately. In the simulation the smaller electrode on the downside of the discs is used as defining geometry for *Remote Displacement*. Here only one degree of freedom in z-direction was limited. Apart from that this face does not move or rotate. In reality the discs rested on the contact spring for the smaller electrode. The deviation could be minimised by changing from *Remote Displacement* to a support condition which rather corresponds to reality.

### 5.3 Possible ways for evaluation of a significant FEM model of the testing probe

This chapter provides suggestions for evaluation of future simulations regarding an assembled testing probe under real conditions. Again results from the measurement described in this chapter should be compared to simulation results and the other way around. The relation between acoustic and electric admittance could be determined and applied for further comparison. This chapter shall present two different possibilities to enable comparison between the testing probe model and reality which need to be completed. To approve the results of future simulations the measurement of complex electric admittance is presented. Finding a way to calculate the complex electric admittance in the FEM program provides one way to approve the model. Another way for revision is to build a partial model of the testing probe according to the design of a prototype in *ANSYS Workbench*. Here the acoustic admittance can be calculated as described in the section below. Results of this simulation can also be compared to results of future measurements and researches.

The model of the testing probe contains the piezoceramic disc (transducer), a supporting intermediate element (Macor carrier) and a fluid element (water-ethanol mixture). The design of the fluid element is given by the short section of the housing through which the fluid is flowing. Further in the simulation the case is not considered to save additional computing time. The piezoceramic disc transmits sound waves through the Macor carrier to the fluid. There a standing wave is formed. The complex acoustic admittance is calculated as a quotient of velocity and pressure gradient on each node of the Macor - water boundary layer. Here additional measurements need to be done to verify the model. The importance of the model and its quality are based on the chance to calculate and display the sound pressure distribution across the gap between Macor and reflector shown in Figure 68. In Figure 69 we see the pressure distribution on top of the water-ethanol body. On this position the reflector for the acoustic waves is mounted in the testing probe. For this purpose the top layer of the fluid body is defined as acoustically hard boundary. In the centre of the pressure distribution lies the maximum pressure. The pressure waves propagate radially towards the edge and lose power.

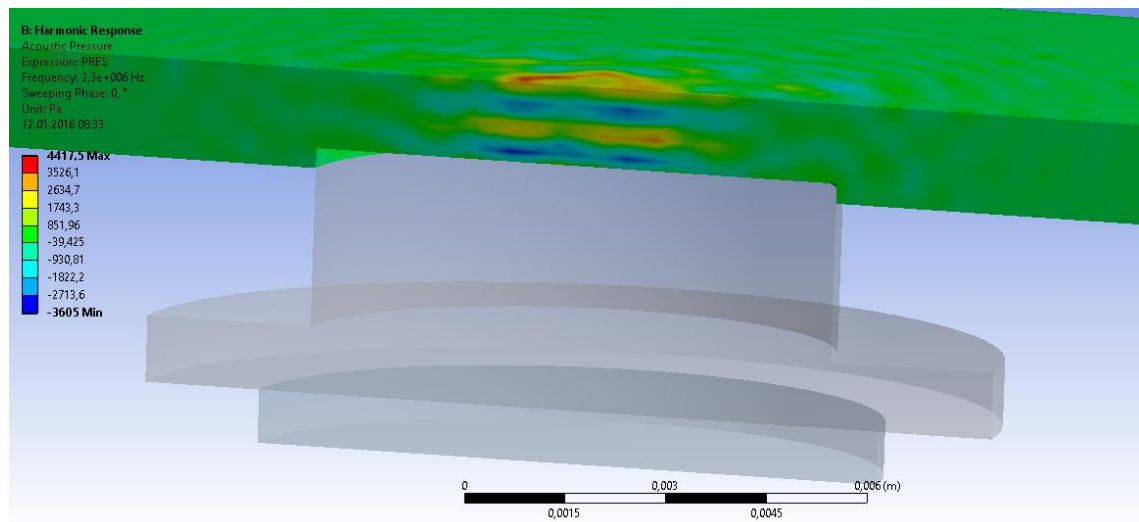


Figure 68: Sound pressure distribution in 50% EtOH at 2,3 MHz, gap of 1,2 mm

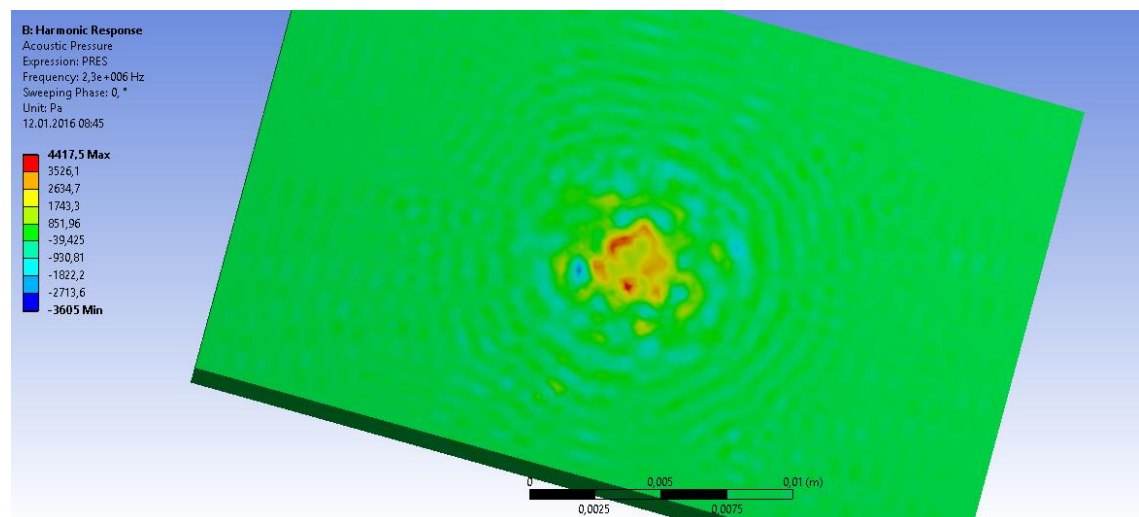
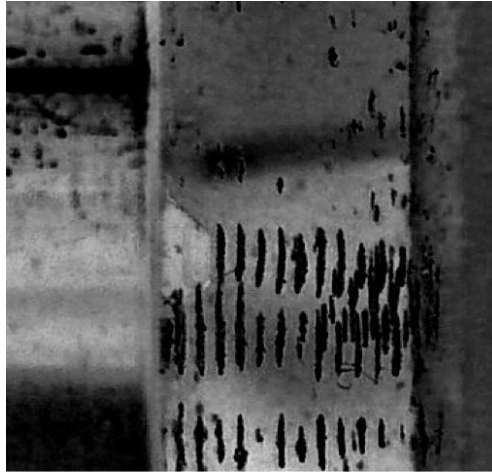


Figure 69: Pressure distribution at reflector, 2.3MHz, gap of 1,2 mm

Both analysis are performed in 9 different variations- 3 different widths of the passage for the fluid flow with 3 different compositions of a water-ethanol mixture.

### 5.3.1 Proposal for measurement

To be able to evaluate the simulation model in future researches real tests have to be done using a fully working testing probe prototype. It has already been tested on polymer particles dispersed in water. The prototype emits sound waves which form a standing wave. The particles in Figure 70 got caught in the nodal planes of the ultrasonic wave and could be photographed.

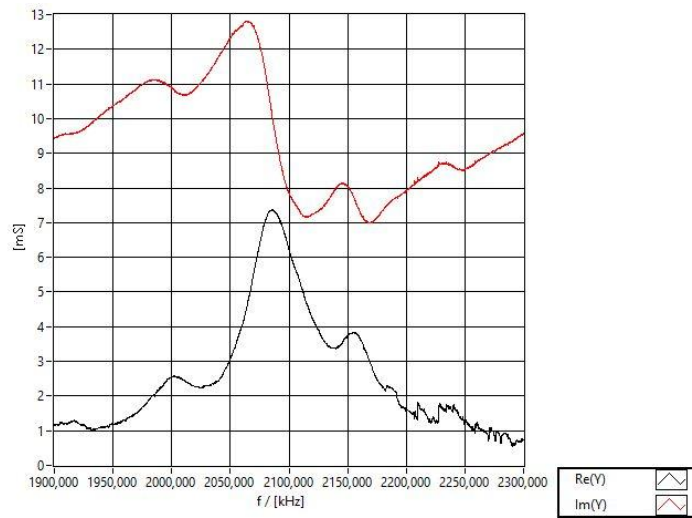


**Figure 70: Particles caught by standing wave at 1,85 MHz, provided by Dr. Stefan Radel, University of Technology Vienna**

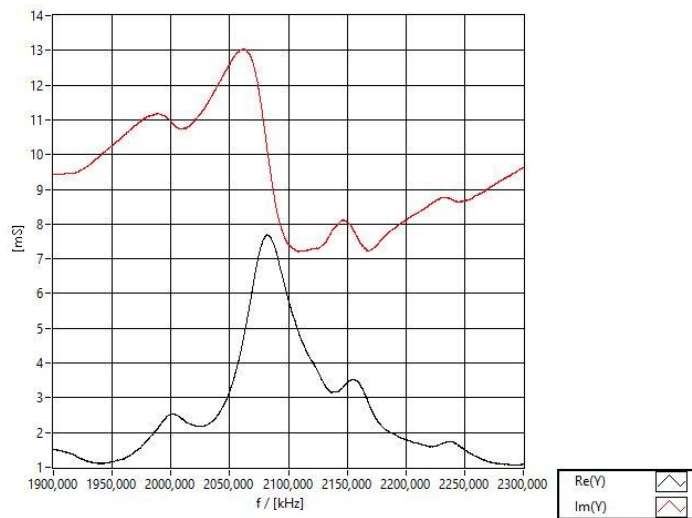
For the described purpose the complex electric admittance of the complete system including piezoceramic, Macor and water at different frequencies was measured. The complex electric admittance has been detected using an Impedance Analyzer by SinePhase Instruments GmbH, Mödling, Austria, and the corresponding analysing software. Three different mixtures of ethanol and water, each with three different distances (Table 6) between Macor and reflector in the prototype, have been examined. The reflector in the prototype was cut from a sample carrier for microscopes. Below the graphs of complex admittance are plotted over the frequencies in a range of 1,9 - 2,3 MHz. This range is also the working range of the testing probe for practical applications.

**Table 6: Variation of parameters for complex admittance**

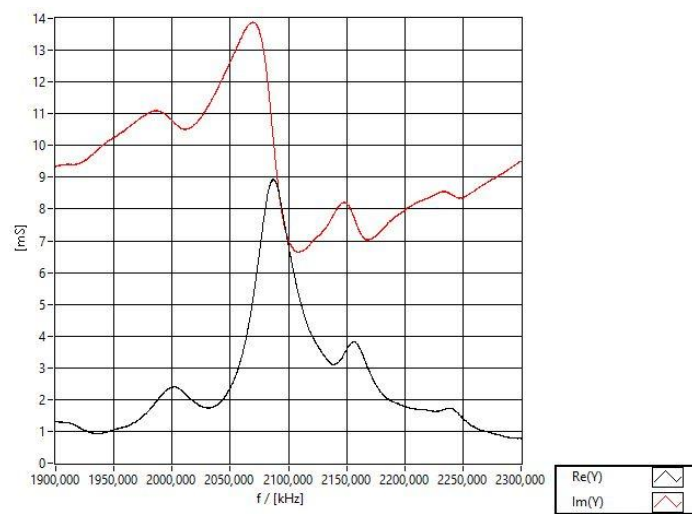
<b>Distance [mm]</b>	1,2	1,4	1,6
<b>Ethanol [vol%]</b>	5	20	50



**Figure 71: Electric admittance, 5% EtOH and 1,2 mm**



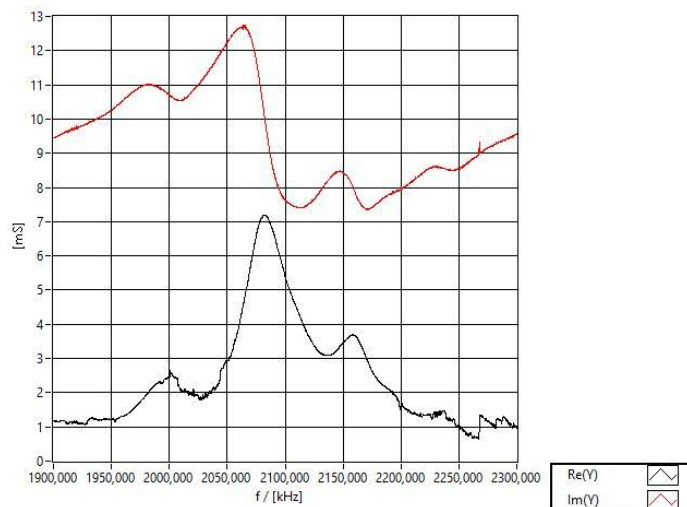
**Figure 72: Electric admittance, 5% EtOH and 1,4 mm**



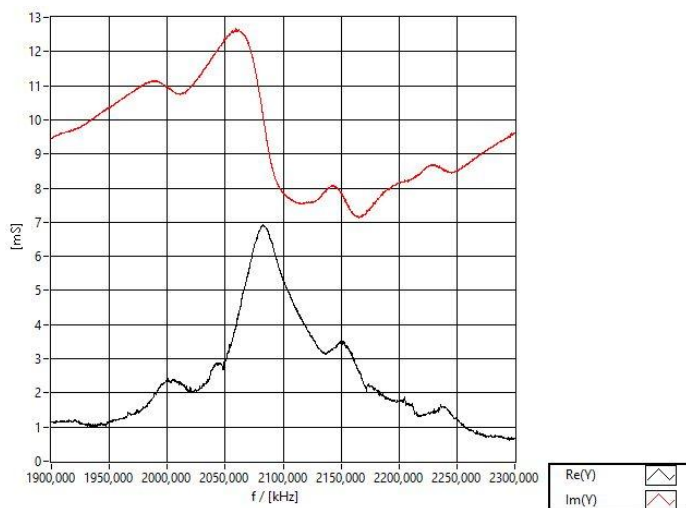
**Figure 73: Electric admittance, 5% EtOH and 1,6 mm**

Figure 71 to Figure 73 present the graphs of complex admittance in a system including the piezoceramic, the Macor carrier and the water-ethanol mixture. Here the proportion of ethanol in the mixture is 5%. As for the graphs below the width of the gap between Macor and reflector varies between 1,2 mm, 1,4 mm and 1,6 mm. In Figure 71 to Figure 73 the graphs are very similar in valuation and form. In the beginning from 1,9 MHz to 2,05 MHz both graphs of conductance  $G_e$  (real part - black) and susceptance  $B_e$  (imaginary part - red) show a rise to the point of the peaks.

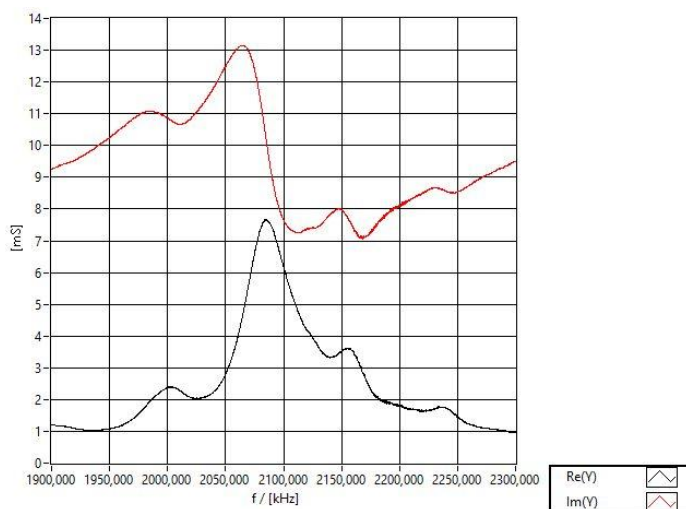
The maximum susceptance is found earlier shortly after 2,02 MHz. The maximum conductance lies approx. at 2,08 MHz. Figure 71 with a gap width of 1,2 mm and Figure 72 with 1,4 mm differ hardly. A noticeable difference can be seen at the peak of conductance in Figure 73 which touches the lower graph of conductance. After reaching the maxima the graph of susceptance rises again to an equal value it had at the start. The graph of conductance also falls to a similar value as the starting point.



**Figure 74: Electric admittance, 20% EtOH and 1,2 mm**



**Figure 75: Electric admittance, 20% EtOH and 1,4 mm**



**76: Electric admittance, 20% EtOH and 1,6 mm**

Figure 74 to 76 again show similar graphs regarding form and range of values. These three figures show the complex admittance for the same setting with a new ethanol proportion of 20 % in the mixture. The peaks of conductance (black graph) are lower than the peaks in Figure 71 to Figure 73. This can be seen especially in 76 in which the point of the peak lies too low to touch the susceptance graph (red). As seen in the figures before we have similar trends at the beginning and the end of the graphs. This also applies to the similarity between start and end values. Additionally, the peaks lie at the same frequencies as before. The variation of proportion of ethanol in the mixture and the width of the gap do not cause remarkable deviations in these results.

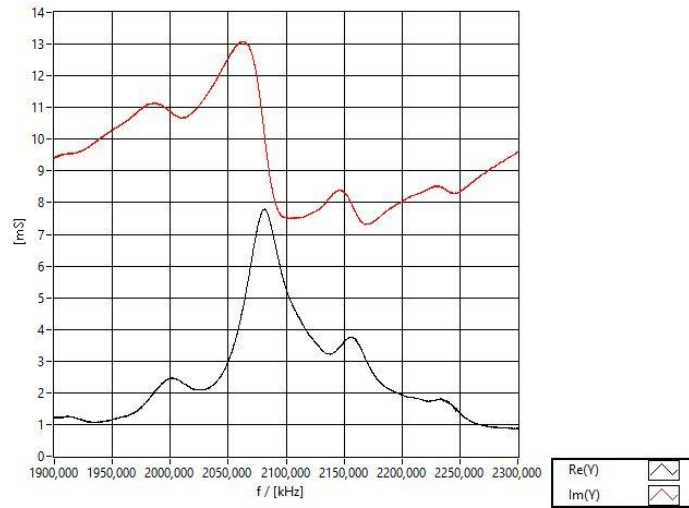


**Figure 77: Electric admittance, 50% EtOH and 1,2 mm**

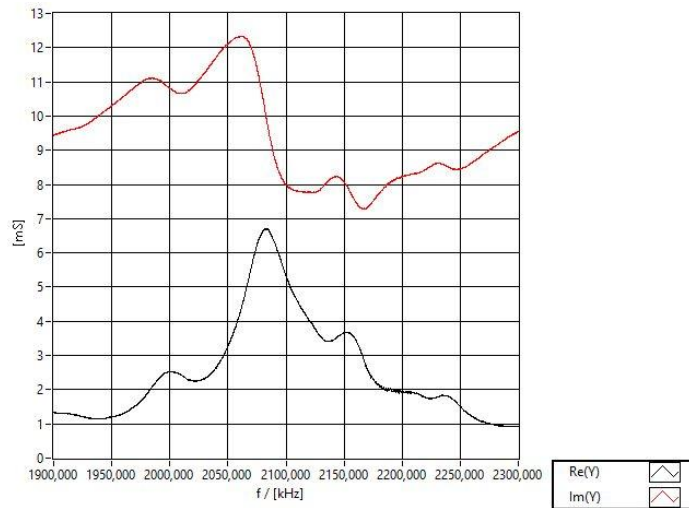


**Figure 78: Electric admittance, 50% EtOH and 1,4 mm**

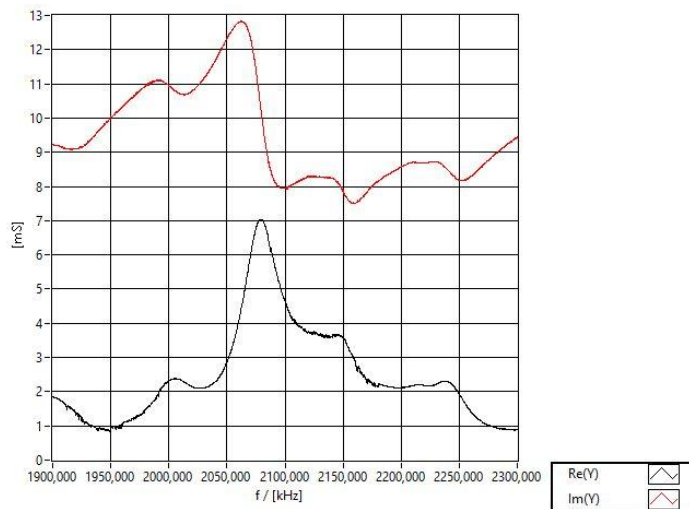


**Figure 79: Electric admittance, 50% EtOH and 1,6 mm**

In Figure 77 to Figure 79 the complex admittance graphs for a mixture with 50 % of ethanol in water can be seen. Here the variation of mixing ratio and gap width doesn't show remarkable changes in value range or form of the graphs. The peak of susceptance (red) for 5 % of ethanol in Figure 72 is the only one of the three graphs at a gap size of 1,4 mm which reaches up to 13 mS. In Figure 73 the susceptance peak for 5 % reaches 13,8 mS, being the only one of the three susceptance peaks for 1,6 mm to reach this value. The peaks of conductance graphs (black) in these three figures also fall more and more from 9 mS for 5 % (Figure 73) over 7,5 mS for 20% (76) to 7,5 mS for 50% (Figure 79). In contrast in Figure 71, Figure 74 and Figure 77 one sees the rise of the conductance peaks for a gap size of 1,2 mm from approximately 7,2 mS to 7,8 mS. A remarkable change of admittance due to variation of mixing ratio can be seen in Figure 77. Here both peaks of conductance and susceptance for 50 % ethanol in water and a gap width of 1,2 mm reach higher than their pendants at 5% and 20% ethanol.

### 5.3.2 Proposal for simulation

For the piezoceramic in this part the same material settings were used as in the previous chapters. The composition of the water-ethanol mixture was given by the corresponding density and speed of sound by using the tool *Acoustic Body* for the fluid. In this case the fixation of the Macor needed to be defined. To match the mounting in the testing probe *Fixed Support* was applied to limit movements. The sound waves are transmitted from the piezoceramic through the Macor into the fluid body. The interface between Macor and fluid was defined as *Acoustic FSI (Fluid Structure Interface)* and *Acoustic Port (network port)*. The boundary conditions for the sound waves were defined by *Acoustic Radiation Boundary* which confined the propagation of sound. The reflector integrated in the prototype was not determined. The last material used was glass from a sample carrier. In the simulation the reflecting surface was defined as *Acoustic Absorption Surface* with *Absorption Coefficient* set to 0. The complex acoustic admittance is defined as the inverse of the acoustic impedance.

The following graphs show the complex acoustic admittance in m/s.Pa plotted over the same frequency range used for the measurements of electric admittance between 1,9 MHz and 2,3 MHz.

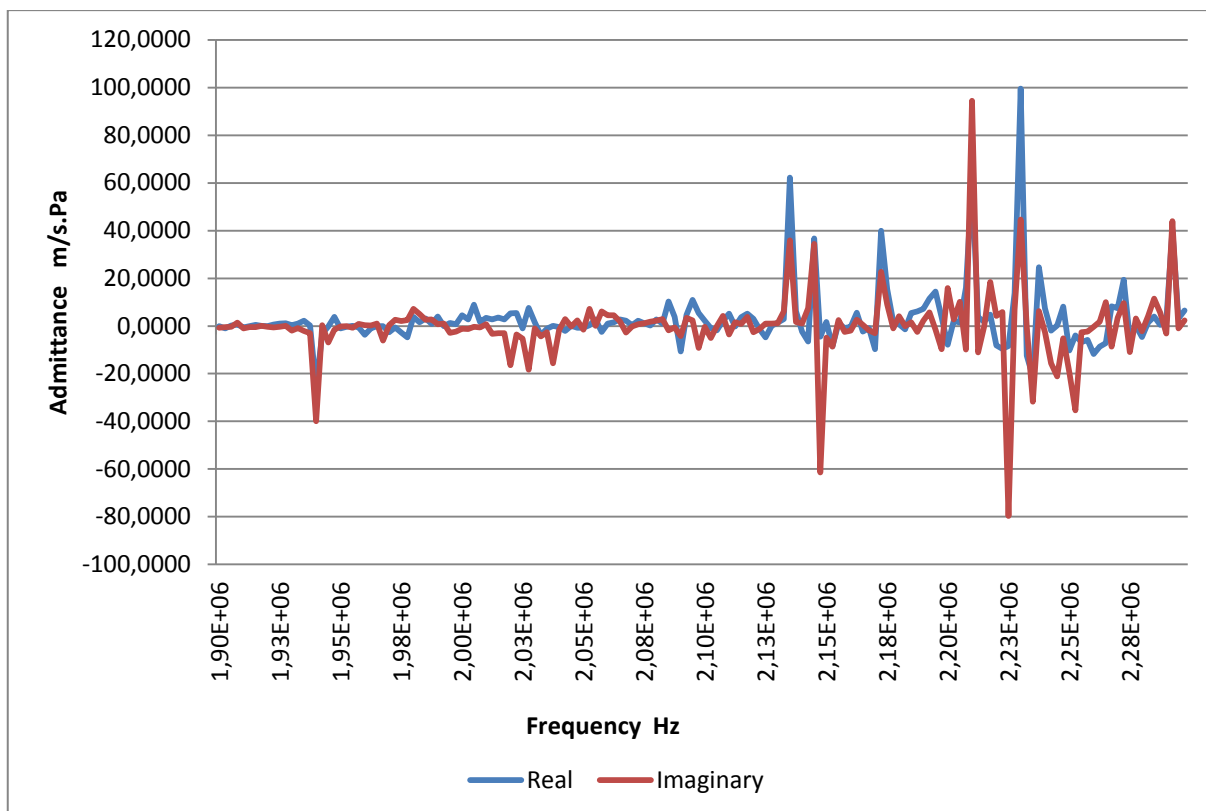


Figure 80: Acoustic admittance, 1,2 mm, 5% EtOH

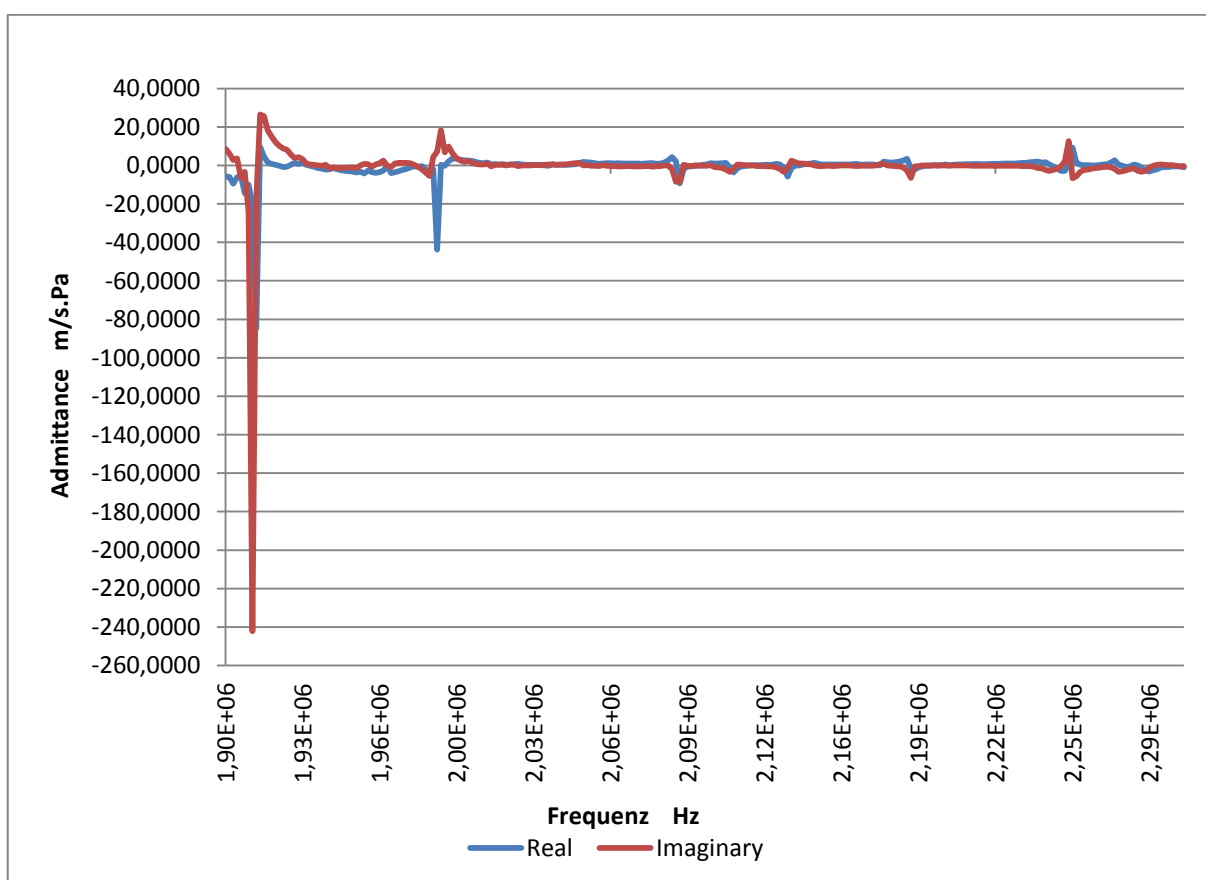
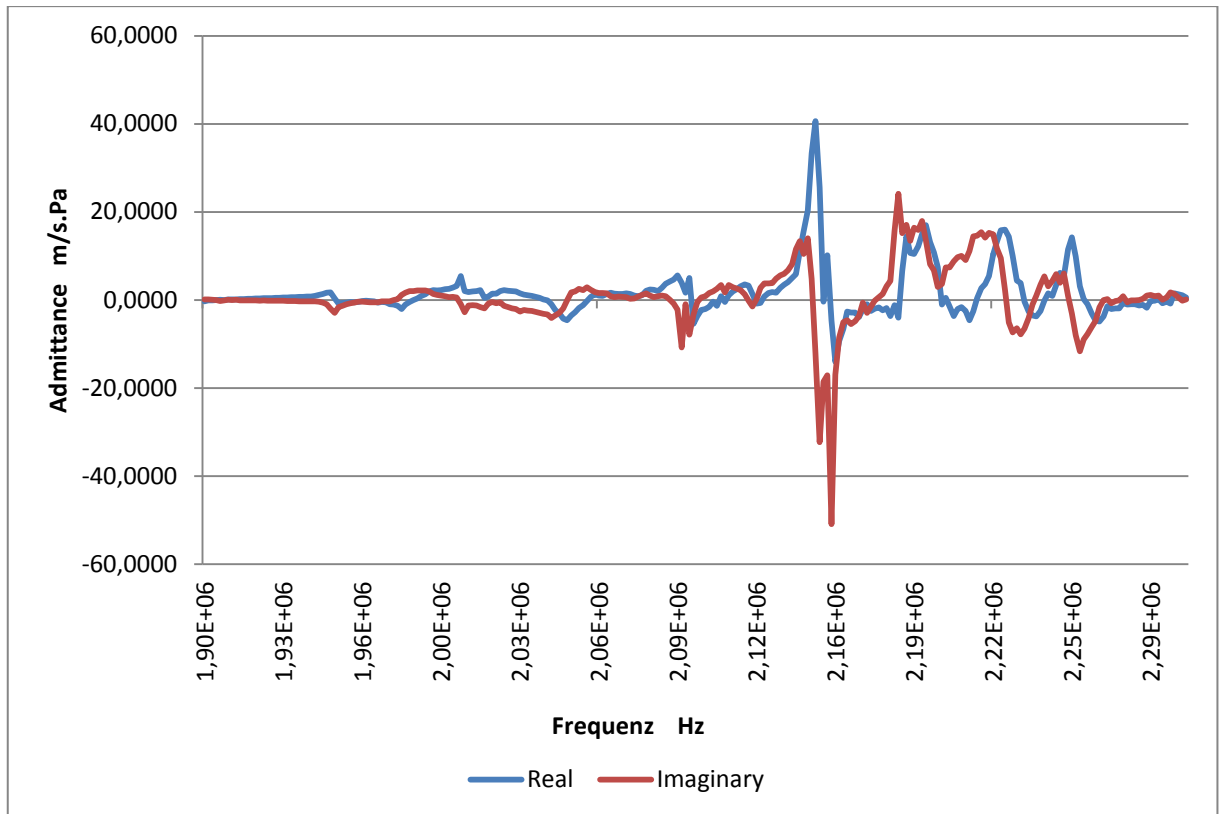


Figure 81: Acoustic admittance, 1,4 mm, 5% EtOH



**Figure 82: Acoustic admittance, 1,6 mm, 5% EtOH**

Figure 80 to Figure 82 show the graphs of acoustic admittance for 5% ethanol in water and the gap sizes 1,2 mm, 1,4 mm and 1,6 mm. Since the acoustic admittance is a complex quantity we see two graphs, one for the conductance (real part- blue) and one for the susceptance (imaginary part - red). The form and value range of the graphs in these figures show more significant differences than the graphs for electric admittance. The graphs for conductance and susceptance do not differ as much. Their forms and trends are similar and their peaks lie close together regarding the frequencies. Figure 80 and Figure 82 show peaks beginning at approximately 2,14 MHz. The peaks in Figure 80 reach higher values above 80 m/s.Pa. Peaks in Figure 82 only reach up to 40 m/s.Pa. The graphs in Figure 81 show a completely different trend. The maximum peak at 1,92 MHz for susceptance extends in negative direction. The variation of the gap size shows here more distinctively than in the measurements of electric admittance.

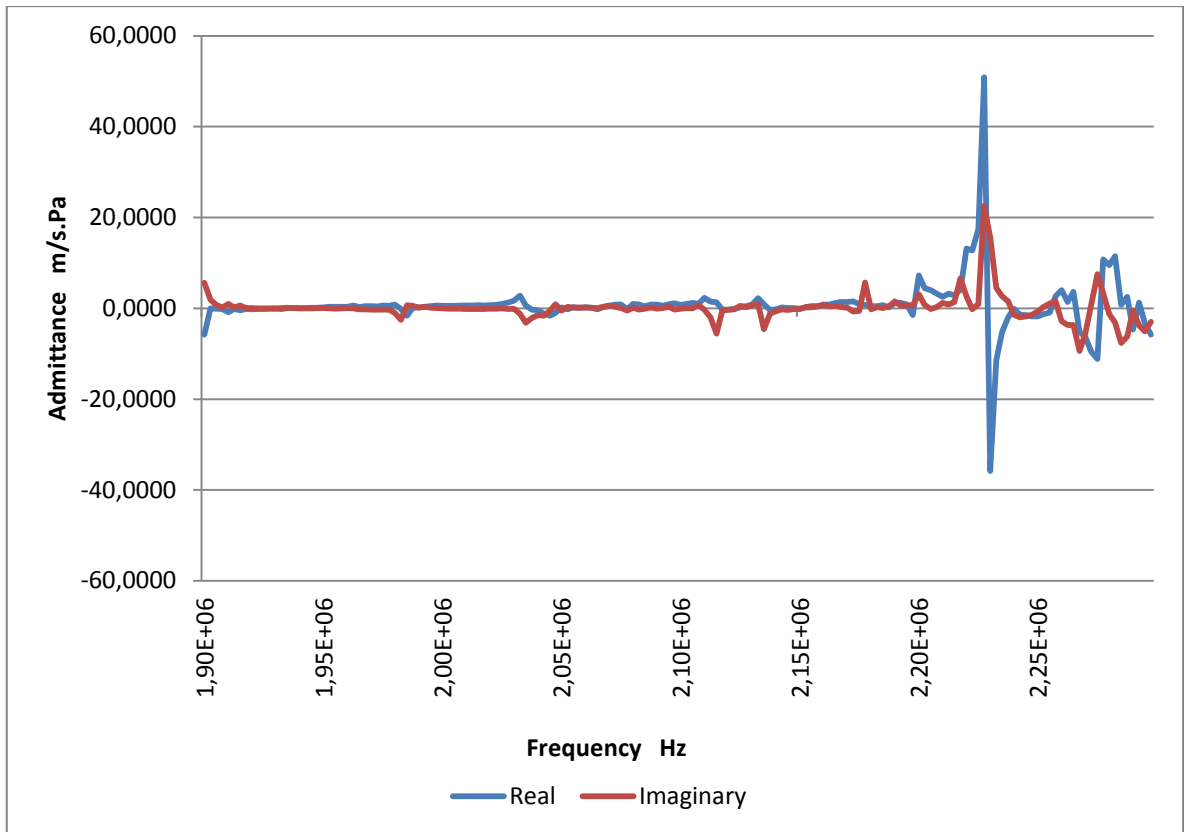


Figure 83: Acoustic admittance, 1,2 mm, 20% EtOH

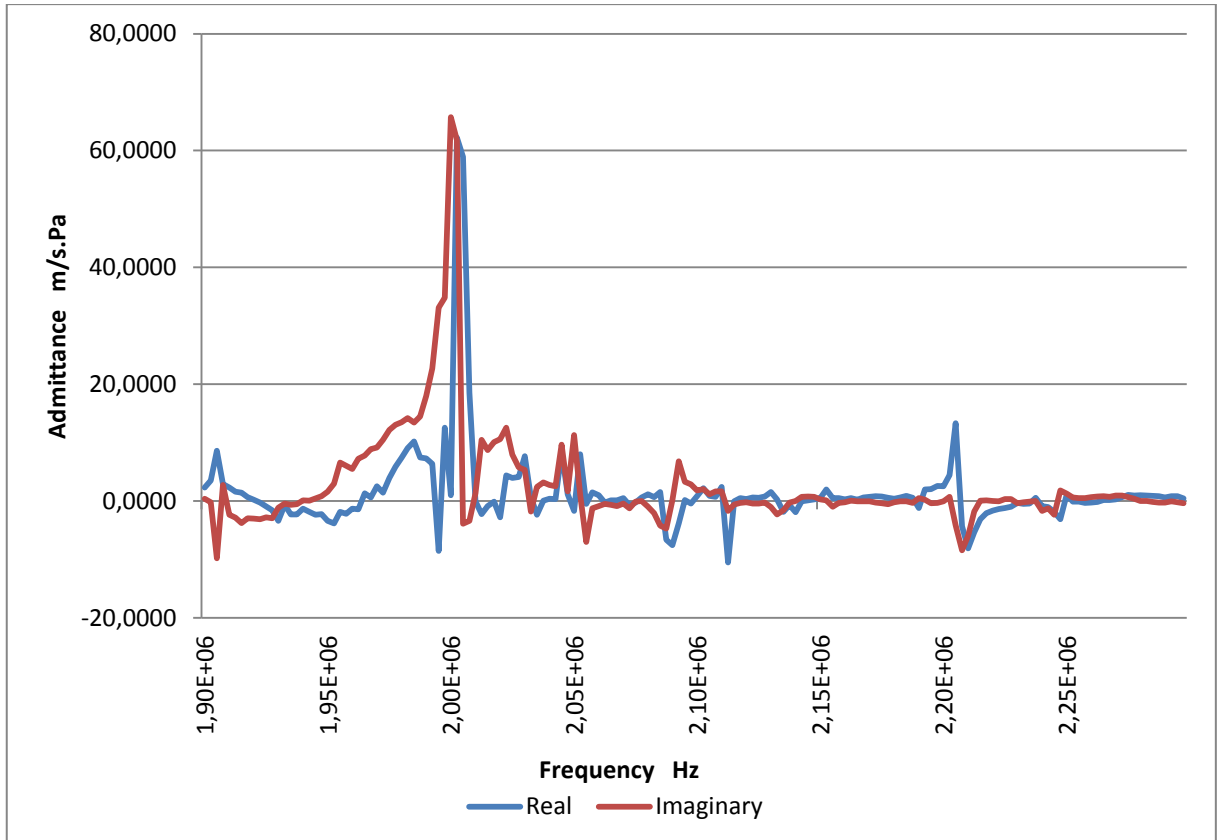
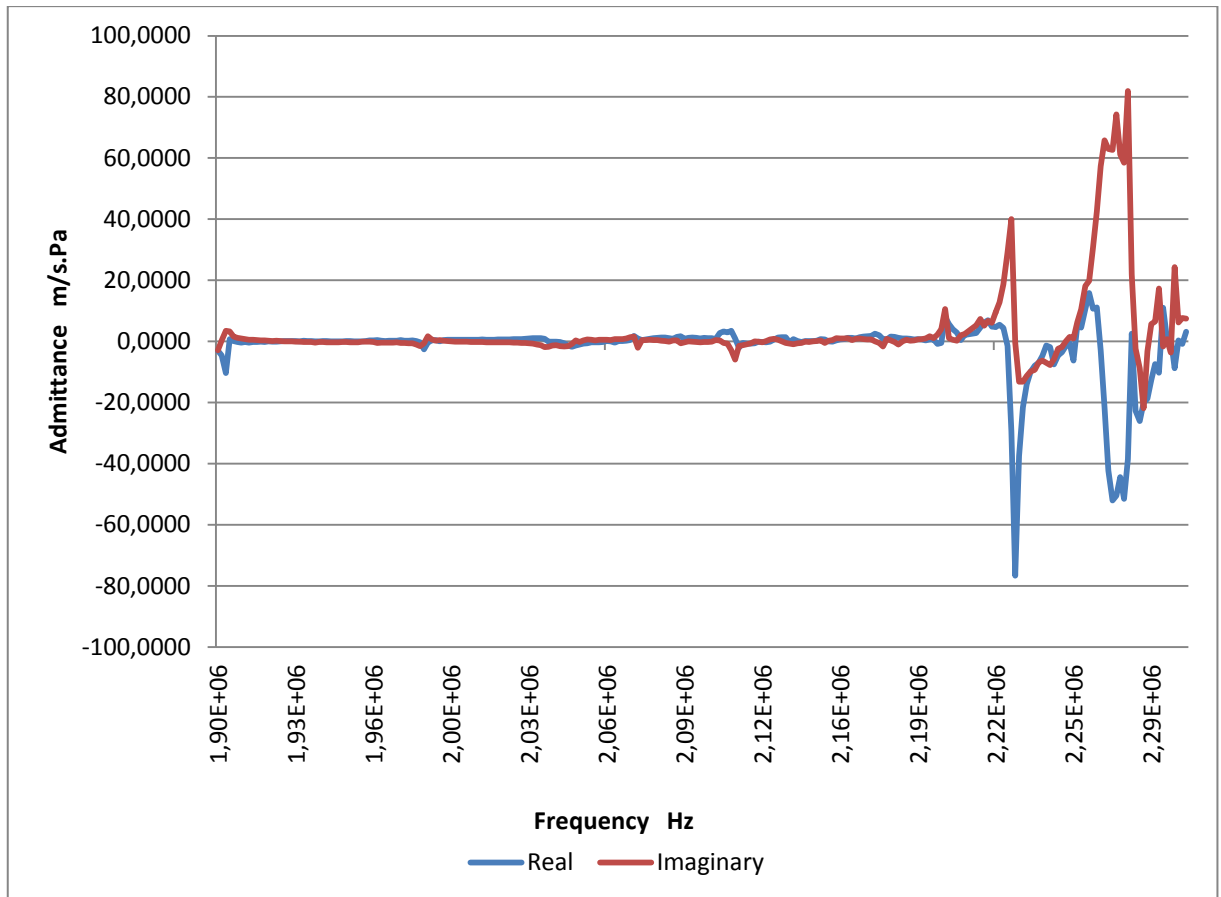


Figure 84: Acoustic admittance, 1,4 mm, 20% EtOH



**Figure 85: Acoustic admittance, 1,6 mm, 20% EtOH**

The graphs in Figure 83 to Figure 85 and the graphs in Figure 80 to Figure 82 have similarities but do not match completely in several characteristics. The most striking difference is visible in Figure 84. Here the maximum peak for susceptance extends in positive direction in contrast to the graph in Figure 81. Also the conductance peak is larger at this frequency than its pendant. The trends in Figure 83 and Figure 85 are similar to the trends for 5% ethanol in water. The graphs in Figure 80 and Figure 82 feature more peaks at the end of the frequency range and not as distinctive conductance peaks in the negative section. Looking at the following graphs for 50% ethanol in water we can see that the results for 20% are generally distinct from the others.

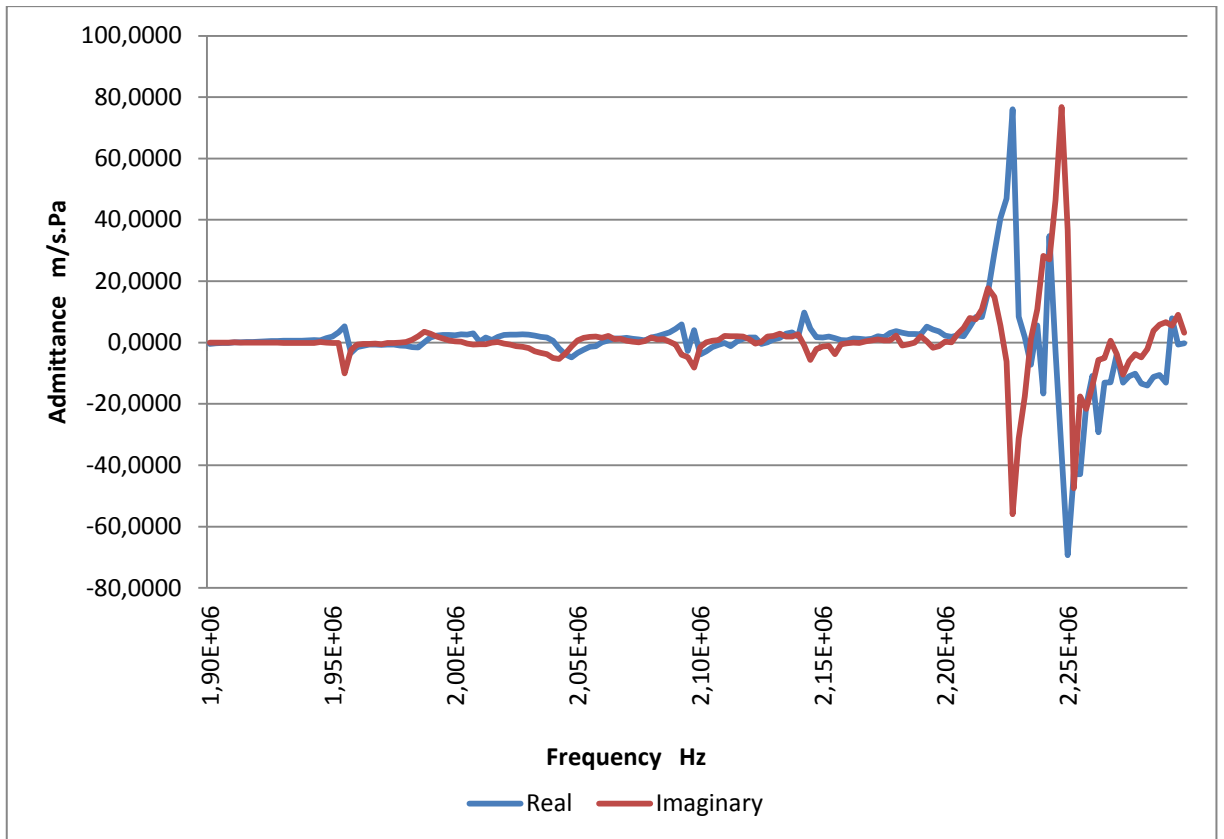


Figure 86: Acoustic admittance, 1,2 mm, 50% EtOH

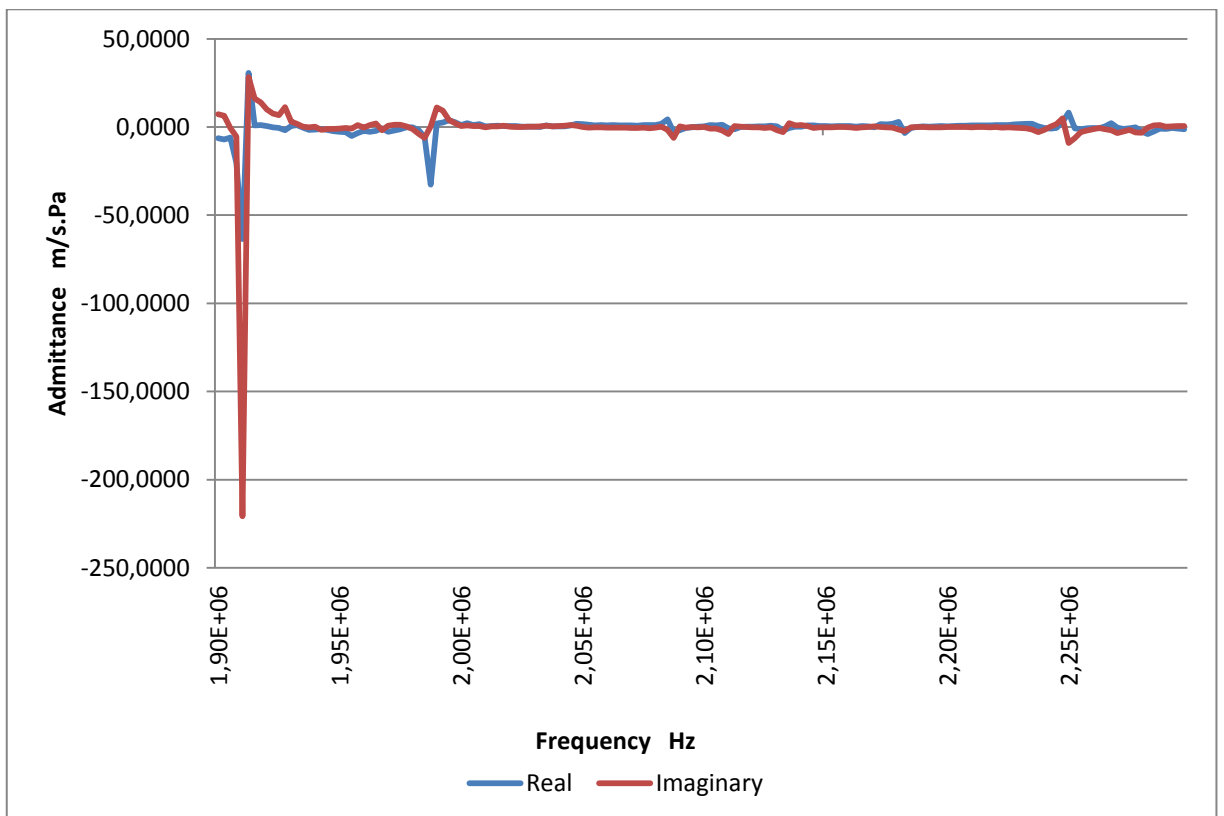
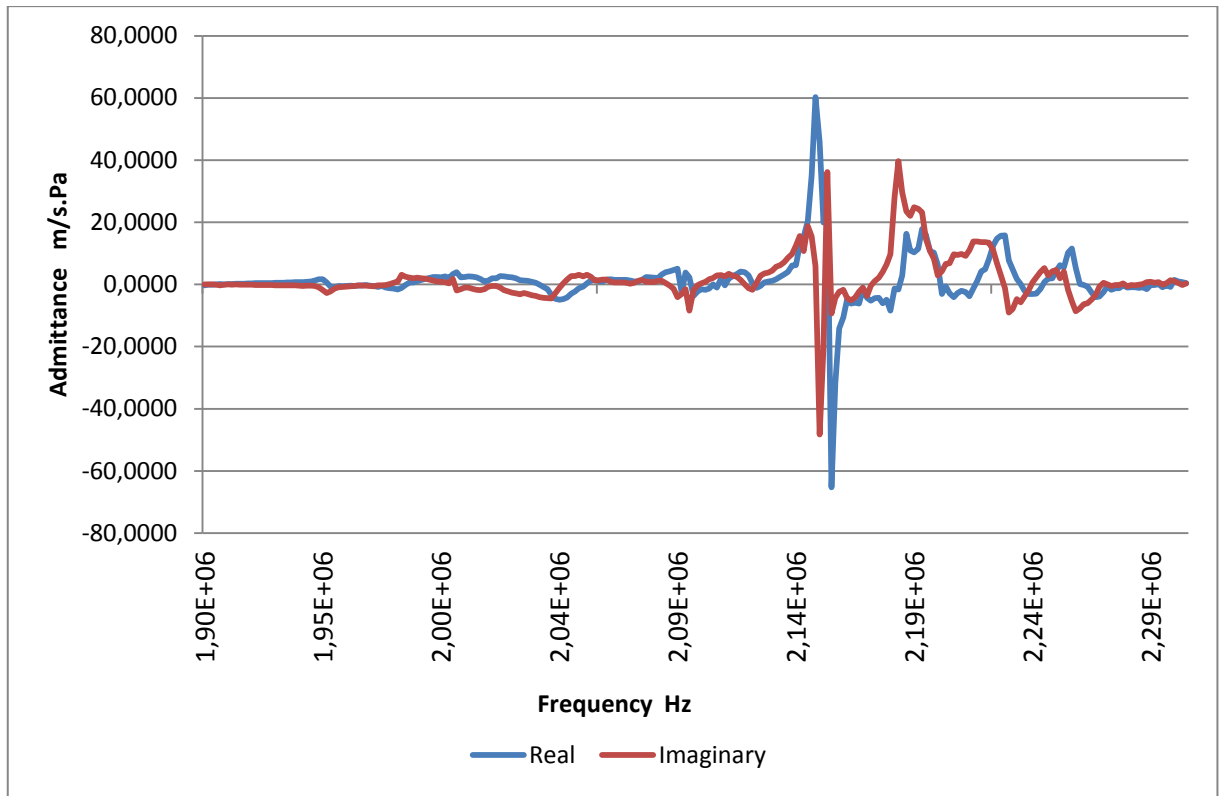


Figure 87: Acoustic admittance, 1,4mm, 50% EtOH



**Figure 88: Acoustic admittance, 1,6 mm, 50% EtOH**

Figure 86 to Figure 88 show similar value ranges and trends as the graphs in Figure 80 to Figure 82. In Figure 87 again we see a susceptance peak extended in negative direction at 1,92 MHz. The graphs in Figure 82 and Figure 88 for a gap width of 1,6 mm hardly differ as their peaks lie at the same frequencies. The only significant difference is that the conductance peaks in Figure 88 at 2,14 MHz and 2,16 MHz reach up to 60 m/s.Pa and down to -60 m/s.Pa, where the peaks in Figure 82 stop at  $\pm 40$  m/s.Pa. Looking at a gap size of 1,2 mm the graphs for 5% ethanol in Figure 80 show more peaks than the graphs for 50% in Figure 86. Again Figure 80 features more peaks starting at 2,14 MHz than Figure 86 starting at 2,22 MHz.

## 6 Summary and Conclusion

The goal of this thesis is to provide a FEM model for predicting the behaviour of an ATR testing probe, regarding the ultrasonic transducers, before and after modifications are performed during further researches. In Chapters 5.1 and 5.2 the model of a single piezoceramic disc is presented and discussed. At first the natural frequencies of the disc were measured using a vibrometer and later compared to modal analysis results obtained from simulations done in *ANSYS Workbench*. Measurement and simulation show several compliances but also a shift at some frequencies.

For the model of the piezoceramic body material data coming from the manufacturer and the dimensions of the real objects were used. That also applies to the second part of the thesis in which the instantaneous values of the discs' surface are examined. The simulation results lie above the acceptable maximum range of  $\pm 30\%$  for an ideal simulation model. The instantaneous values differ by the factor of 2 to 5 which provides a good base for improvement. In both cases deviations can be due to changing or unfavourable measuring conditions caused by the hand-made stand which atop the discs were fixed. The side load caused by the outer clamping varies along with the tightening of the screws holding the top grip plate. In addition, most of the measurements have been performed during summer in a laboratory exposed to sunlight. The temperatures changed noticeably from day to day. The reproducibility of the measurements has suffered noticeably under varying environmental conditions.

Compliances between the measurement and the simulation results have been found. Looking at certain findings it can be seen that further detailing is needed. In future works the model can be improved regarding the settings for extrinsic forces due to fixation. Displacement settings in *ANSYS Workbench* can only provide a minor representation of the real fixation forces and loads, but still more practically than a rigid displacement setting without any degree of freedom. There are also speculations about the effect of different electrode patterns on the vibration behaviour. In the simulations the electrodes were constructed as imprinted faces (infinite thin layer) on the surface of the discs. They were used to define the area for the voltage applied to generate displacement according to the piezoelectric effect. The results of changing the electrodes' form are not evaluated and need to be part of further researches.

The last part of the thesis presents options for further analysis and initial results to be able to evaluate a significant simulation model of the testing probe and compare it to a prototype. These options could be pursued by performing additional calculations and measurements. The FEM model of the testing probe consists of the piezoelectric actuator, the Macor carrier and the fluid body. For the validation of the FEM simulation measurements need to be performed. Their results are compared to the results found in the simulation. For this purpose the electric admittance has been measured under laboratory conditions. Here a fitting FEM simulation needs to be calculated. Respectively the acoustic admittance has been calculated in *ANSYS Workbench*. To evaluate the results additional measurements of the acoustic admittance using a prototype of the testing probe need to be done. This way the significance of the FEM model and its relation to reality can be determined.

## 7 Perspective

For the further development of the ATR testing probe a useful FEM model would be of great value. The technical progress would expedite as modifications and their consequences can already be examined in the simulation model. This way the time and resources consuming process of constructing a new prototype every time can be prevented. Building and approving such a model is the goal of this thesis. Yet some parts stay unexplored. For the usage of the assembled testing probe in combination with fluids a significant FEM model should be built and provided with practical boundary conditions and parameters. In practice the prototype is able to emit ultrasonic waves which are forming a standing wave. Under laboratory conditions PVC particles have been captured in the nodal planes of the sound wave. Using a magnetic stirrer the liquid and therefore the particles have been actuated to direct them into the operating area of the wave. They accumulated into a single-layer package. After a short time the package reached a size big enough for the particles at the outer rim to begin to get carried away by the flow. These tests have shown that a working prototype is already available. As fluid flow will be also appear during real life applications of the probe it is reasonable to include it in future simulations.

First of all the model of the testing probe used for the third part in this thesis needs to be evaluated. For this purpose, on the one hand, the experimental results for electric admittance can be compared to a simulation done in *ANSYS Workbench*. On the other hand the simulation results for acoustic admittance can be used for comparison with measurement results. This way a first tool for validation of the significant testing probe model is provided. In the course of further research the *ANSYS Workbench* model built in *Harmonic Response* during this thesis can be expand with *ANSYS Fluent*. For this purpose the link between these two tools for analysis must be accomplished by *System Coupling* or by other means enabling *ANSYS Fluent* to use results found by *Harmonic Response*. The implementation of piezoceramic elements in *ANSYS Fluent* could turn out to be difficult and time consuming. To avoid complicated adjustments the source of sound waves would no longer be the piezoceramic disc. Instead the distribution of sound pressure across the Macor surface could be used as boundary condition. The calculation of sound pressure is possible using *Harmonic Response* and the *Acoustics Extension*. Prior to applying this method the quality of the results should be analysed by measuring the sound pressure distribution through the gap between the Macor carrier and the reflector and comparing the values to the simulation.

After defining the sound source this way, particles need to be added to the medium. For this settings multiphase flow would be used in *ANSYS Fluent* depending on the percentage of particles in the fluid (e.g. mixture multiphase). Finally boundary conditions and parameters for the flow in particular are done and matched as close to reality as possible.

This part of the project needs more detailed implementation of the model and further processing of the previous results. The new model could provide interesting insights regarding the effect of the fluid's composition and flow rate. Changing the sound parameters for different tests would still be possible by adapting the sound pressure serving as boundary condition.

## References

- [1] C. Koch, M. Brandstetter, P. Wechselberger, B. Lorantfy, M. R. Plata, S. Radel, C. Herwig, and B. Lendl, "Ultrasound-Enhanced Attenuated Total Reflection Mid-infrared Spectroscopy In-Line Probe: Acquisition of Cell Spectra in a Bioreactor," *Anal. Chem*, vol. 87, no. 4, pp. 2314–2320, 2015.
- [2] S. Radel and M. Brandstetter, "Ultrasound enhanced Vibrational Spectroscopy Probe" WO 2010/078612 A1.
- [3] C. Leonelli and T. J. Mason, "Microwave and ultrasonic processing: Now a realistic option for industry," *Chemical Engineering and Processing: Process Intensification*, vol. 49, no. 9, pp. 885–900, 2010.
- [4] U. Hempel, S. Wöckel, and J. Auge, "Ultraschallbasierte Informationsgewinnung in der Verfahrenstechnik," *Chemie Ingenieur Technik*, vol. 82, no. 4, pp. 491–502, 2010.
- [5] M. Cai, S. Zhao, and H. Liang, "Mechanisms for the enhancement of ultrafiltration and membrane cleaning by different ultrasonic frequencies," *Desalination*, vol. 263, no. 1-3, pp. 133–138, 2010.
- [6] T. J. Mason and D. Peters, *Practical sonochemistry: Uses and applications of ultrasound*, 2nd ed. Chichester: Horwood, 2002.
- [7] L. Liu, Z. Ding, L. Chang, R. Ma, and Z. Yang, "Ultrasonic enhancement of membrane-based deoxygenation and simultaneous influence on polymeric hollow fiber membrane," *Separation and Purification Technology*, vol. 56, no. 2, pp. 133–142, 2007.
- [8] H. C. Kuhlmann, *Strömungsmechanik*. München: Pearson Education, 2007, pp.16.
- [9] C. E. Brennen, *Cavitation and bubble dynamics*. New York, NY: Cambridge Univ. Press, 2014.
- [10] J. Chen, Y.-C. Yang, and J.-Y. Huang, "On-line monitoring and diagnosis of membrane fouling using ultrasonic techniques," *Chemometrics and Intelligent Laboratory Systems*, vol. 127, pp. 147–157, 2013.
- [11] R. Sanderson, J. Li, L. J. Koen, and L. Lorenzen, "Ultrasonic time-domain reflectometry as a non-destructive instrumental visualization technique to monitor inorganic fouling and cleaning on reverse osmosis membranes," *Journal of Membrane Science*, vol. 207, no. 1, pp. 105–117, 2002.
- [12] D. Chen, L. Weavers, H. Walker, and J. Lenhart, "Ultrasonic control of ceramic membrane fouling caused by natural organic matter and silica particles," *Journal of Membrane Science*, vol. 276, no. 1-2, pp. 135–144, 2006.
- [13] A. Mirzaie and T. Mohammadi, "Effect of ultrasonic waves on flux enhancement in microfiltration of milk," *Journal of Food Engineering*, vol. 108, no. 1, pp. 77–86, 2012.
- [14] D. Veerasamy, A. Supurmaniam, and Z. Nor, "Evaluating the use of in-situ ultrasonication to reduce fouling during natural rubber skim latex (waste latex) recovery by ultrafiltration," vol. 236, no. 1, pp. 202–207, 2009.
- [15] A. Maskooki, S. A. Mortazavi, and A. Maskooki, "Cleaning of spiralwound ultrafiltration membranes using ultrasound and alkaline solution of EDTA," *Desalination*, vol. 264, no. 1-2, pp. 63–69, 2010.
- [16] J. Li, "Ultrasonic cleaning of nylon microfiltration membranes fouled by Kraft paper mill effluent," *Journal of Membrane Science*, vol. 205, no. 1-2, pp. 247–257, 2002.

- [17] C. Loderer, D. Pawelka, W. Vazier, P. Hasal, and W. Fuchs, "Dynamic filtration – Ultrasonic cleaning in a continuous operated filtration process under submerged conditions," *Separation and Purification Technology*, vol. 119, pp. 72–81, 2013.
- [18] J. K. Krinks, M. Qiu, I. A. Mergos, L. K. Weavers, P. J. Mouser, and H. Verweij, "Piezoceramic membrane with built-in ultrasonic defouling," *Journal of Membrane Science*, vol. 494, pp. 130–135, 2015.
- [19] S. R. Shirsath, S. H. Sonawane, and P. R. Gogate, "Intensification of extraction of natural products using ultrasonic irradiations—A review of current status," *Chemical Engineering and Processing: Process Intensification*, vol. 53, pp. 10–23, 2012.
- [20] J. Dodds, F. Espitalier, O. Louisnard, R. Grossier, R. David, M. Hassoun, F. Baillon, C. Gatamel, and N. Lyczko, "The Effect of Ultrasound on Crystallisation-Precipitation Processes: Some Examples and a New Segregation Model," *Part. Part. Syst. Charact*, vol. 24, no. 1, pp. 18–28, 2007.
- [21] M. Louhikultanen, M. Karjalainen, J. Rantanen, M. Huhtanen, and J. Kallas, "Crystallization of glycine with ultrasound," *International Journal of Pharmaceutics*, vol. 320, no. 1-2, pp. 23–29, 2006.
- [22] O. Narducci, A. G. Jones, and E. Kougoulos, "Continuous crystallization of adipic acid with ultrasound," *Chemical Engineering Science*, vol. 66, no. 6, pp. 1069–1076, 2011.
- [23] M. Mracek and J. Wallaschek, "A system for powder transport based on piezoelectrically excited ultrasonic progressive waves," *Materials Chemistry and Physics*, vol. 90, no. 2-3, pp. 378–380, 2005.
- [24] P. Glynne-Jones, M. Hill, N. R. Harris, R. J. Townsend, and S. K. Ravula, "The design and modeling of a lateral acoustic particle manipulator exhibiting quarter-wave operation," *J. Acoust. Soc. Am*, vol. 123, no. 5, pp. 5988–5990, 2008.
- [25] T. Kozuka, K. Yasui, S.-i. Hatanaka, T. Tuziuti, K. Suzuki, and A. Towata, "Manipulation of Particles in a Microchannel with Various Geometric Spaces Using Ultrasound," *Jpn. J. Appl. Phys*, vol. 50, no. 7, pp. 07HE27: 1-4, 2011.
- [26] E. Benes, M. Gröschl, H. Nowotny, F. Trampler, T. Keijzer, H. Böhm, S. Radel, L. Gherardini, J. J. Hawkes, R. König, and C. and Delouvroy, *Ultrasonic Separation of suspended Particles*. Available: [https://www.researchgate.net/publication/3941396\\_Ultrasonic\\_separation\\_of\\_suspended\\_particles](https://www.researchgate.net/publication/3941396_Ultrasonic_separation_of_suspended_particles) (2016, Feb. 16).
- [27] C. Koch, "Bio-suspensions in the ultrasonic h-shape filter," Diploma thesis, Institut für Allgemeine Physik, Vienna University of Technology, Vienna, 2009.
- [28] C. B. Singh and D. S. Jayas, "Optical sensors and online spectroscopy for automated quality and safety inspection of food products," *Robotics and automation in the food industry, Chap. 5*, pp. 111–129, 2013.
- [29] A. Hashimoto and T. Kameoka, "Applications of Infrared Spectroscopy to Biochemical, Food, and Agricultural Processes," *Applied Spectroscopy Reviews*, vol. 43, no. 5, pp. 416–451, 2008.
- [30] S. D. Silva, R. P. Feliciano, L. V. Boas, and M. R. Bronze, "Application of FTIR-ATR to Moscatel dessert wines for prediction of total phenolic and flavonoid contents and antioxidant capacity," *Food Chemistry*, vol. 150, pp. 489–493, 2014.
- [31] M. Kyraleou, C. Pappas, E. Voskidi, Y. Kotseridis, M. Basalekou, P. A. Tarantilis, and S. Kallithraka, "Diffuse reflectance Fourier transform infrared spectroscopy for simultaneous quantification of total phenolics and condensed tannins contained in grape seeds," *Industrial Crops and Products*, vol. 74, pp. 784–791, 2015.

- [32] D. McMullin, B. Mizaikoff, and R. Krska, "Advancements in IR spectroscopic approaches for the determination of fungal derived contaminations in food crops," *Anal Bioanal Chem*, vol. 407, no. 3, pp. 653–660, 2015.
- [33] M. W. P. Petryk, "Promising Spectroscopic Techniques for the Portable Detection of Condensed-Phase Contaminants on Surfaces," *Applied Spectroscopy Reviews*, vol. 42, no. 3, pp. 287–343, 2007.
- [34] J. Andanson and A. Baiker, "Exploring catalytic solid/liquid interfaces by in situ attenuated total reflection infrared spectroscopy," *Chem. Soc. Rev*, vol. 39, no. 12, pp. 4571–4575, 2010.
- [35] G. Clemens, J. R. Hands, K. M. Dorling, and M. J. Baker, "Vibrational spectroscopic methods for cytology and cellular research," *Analyst*, vol. 139, no. 18, pp. 4411–4444, 2014.
- [36] R. Lerch, G. Sessler, and D. Wolf, *Technische Akustik: Grundlagen und Anwendungen*. Berlin, Heidelberg: Springer Berlin Heidelberg, 2009, pp.1-50.
- [37] S.W. Rienstra and A. Hirschberg, "An Introduction to Acoustics," Eindhoven University of Technology, 2015.
- [38] S. Radel, "2014 Ultrasonic Particle Manipulation," Lecture script, Vienna University of Technology, Institute of General Physics, Workgroup Sensors and Ultrasonics, Vienna.
- [39] G. R. Sinambari, S. Sentpali, and F. Kunz, *Ingenieurakustik: Physikalische Grundlagen und Anwendungsbeispiele*, 5th ed. Wiesbaden: Springer Vieweg, 2014, pp.7-111.
- [40] S. Radel, "2014 Physics fundamentals," Lecture script, Vienna University of Technology, Institute of General Physics, Workgroup Sensors and Ultrasonics of General Physics, Vienna.
- [41] D. Roche, "'Accuracy, Productivity and Performance in Structural Mechanics" Reduction and Acceleration Techniques for Solving Large Models: Introduction in Acoustics," Acoustics ACTx R145
- [42] *Susceptance and Admittance : Reactance And Impedance -- R, L, And C - Electronics Textbook*. Available: <http://www.allaboutcircuits.com/textbook/alternating-current/chpt-5/susceptance-and-admittance/> (2016, Jan. 24).
- [43] Halgard Staesche, "Versuch 7 FTIR-Spektroskopie: Apparatives Praktikum," Lecture script, Westfälische Wilhelms-Universität Münster, Münster.
- [44] Physik Instrumente (PI) GmbH & Co. KG, *Fundamentals of Piezo Technology*. Available: [http://www.piceramic.com/piezo-technology/fundamentals.html?\\_ga=1.14759222.1257913155.1440082610](http://www.piceramic.com/piezo-technology/fundamentals.html?_ga=1.14759222.1257913155.1440082610) (2015, Sep. 15).
- [45] D. Popovici, F. Constantinescu, M. Maricar, F. I. Hantila, M. Nitescu, and Gheorghe A, "Modeling and Simulation of Piezoelectric Devices," Politehnica University of Bucharest, Romania, Romania.
- [46] M. W. Nygren, "Finite Element Modeling of Piezoelectric Ultrasonic Transducers," Master thesis, Department of Electronics and Telecommunications, Norwegian University of Science and Technology, 2011.
- [47] *First-principles study of piezoelectricity in PZT - MSE 5320*. Available: <http://electronicstructure.wikidot.com/first-principles-study-of-piezoelectricity-in-pzt> (2015, Sep. 01).
- [48] B. A. Auld, "Wave propagation and resonance in piezoelectric materials," *The Journal of the Acoustical Society of America*, no. 70 (6), pp. 1577–1585, 1981.
- [49] S. Imaoka, "Conversion of Piezoelectric Material Data: ANSYS Tip of the Week," *Collaborative Solutions Inc*, 1999.
- [50] P. Fröhlich, *FEM-Anwendungspraxis: Einstieg in die Finite Elemente Analyse Zweisprachige Ausgabe Deutsch/Englisch*, 2005, pp.12-98.

- [51] T. Westermann, *Modellbildung und Simulation: Mit einer Einführung in ANSYS*, 2010, pp.1-134.
- [52] D. Roche, ““Accuracy, Productivity and Performance in Structural Mechanics” Reduction and Acceleration Techniques for Solving Large Models: Piezoelectric exposure in ANSYS WorkBench using ACT,” Piezo ACTx V6
- [53] C. Gebhardt, *Praxisbuch FEM mit ANSYS Workbench: Einführung in die lineare und nichtlineare Mechanik*. München: Hanser, 2011.
- [54] Physik Instrumente (PI) GmbH & Co. KG, *Piezoelectric Materials Made of PZT from PI Ceramic*. Available: <http://www.piceramic.com/products/piezoelectric-materials.html> (2015, Dec. 21).
- [55] A. Risse, *Fertigungsverfahren der Mechatronik, Feinwerk- und Präzisionsgerätetechnik*. Wiesbaden: Imprint Vieweg+Teubner Verlag, 2012, pp. 11-101.
- [56] *MACOR | Advanced Optics | Corning.com*. Available: <http://www.corning.com/emea/de/products/advanced-optics/product-materials/specialty-glass-and-glass-ceramics/glass-ceramics/macor.html> (2016, Jan. 25).
- [57] PI Ceramic GmbH, *14\_0097\_Tab\_DynamischesVerhalten\_D\_E.indd*. Available: <http://www.piceramic.com/> (2015, Sep. 15).
- [58] CADFEM Support Service, Private communication, 2015.
- [59] PI Ceramic Customer Service, Private communication, 2015.

## Appendix

### SAMPLE 1

Row 1 (0°)					
Shot 1		227,70	230,86		
Shot 2		227,70	230,59	235,31	
Shot 3		227,70	230,59	233,87	
Shot 4		227,73	230,90	235,31	
Shot 5	208,09	227,42	230,90		285,43
Shot 6	208,09	227,38		234,84	285,31
Shot 7	208,05	227,38		234,92	285,43
Shot 8	208,09	227,42		235,23	285,43
Shot 9		227,34	230,59		
Shot 10	207,81		230,63	248,09	285,20
Row 2 (90°)					
Shot 1		227,70	230,90		
Shot 2		227,70	230,90		
Shot 3		227,70	230,90		
Shot 4			230,94		
Shot 5	207,89	227,70	230,94		
Shot 6	207,89	227,07	230,86		
Shot 7	207,85	227,11	230,55		
Shot 8		227,11	230,59		
Shot 9		227,38	230,90	246,45	
Shot 10		227,34	230,63		
Row 3 (180°)					
Shot 1		227,07	230,55		
Shot 2		227,07	230,59		
Shot 3		227,07	230,55	235,27	
Shot 4		227,07	230,63		
Shot 5	207,85	226,84	230,82		
Shot 6	208,09	226,72	230,23	233,01	285,08
Shot 7	207,93	226,76		234,96	285,12
Shot 8	207,85	226,76		235,08	285,00
Shot 9	64,30	226,76	230,23	245,78	285,00
Shot 10	70,20	207,77	226,80	230,59	285,08

**SAMPLE 2**

Row 1 (0°)					
Shot 1		218,32	233,91		
Shot 2		218,28	233,91		
Shot 3		218,24	233,91		
Shot 4	201,95	218,24	233,91		
Shot 5	201,95	218,71	233,87		
Shot 6	201,91	218,79	233,91		
Shot 7	201,91	218,87	233,71		
Shot 8	201,99	218,75	233,98		
Shot 9			233,83		
Shot 10			234,02		
Row 2 (90°)					
Shot 1		218,98	233,91	241,68	
Shot 2			233,87	241,25	
Shot 3		218,91	233,87		
Shot 4			233,87		
Shot 5	205,63		233,91		280,12
Shot 6	202,62	220,86	233,71	240,39	280,16
Shot 7			233,91	240,16	280,27
Shot 8			233,59	241,17	280,31
Shot 9			233,95	240,20	
Shot 10			233,87		
Row 3 (180°)					
Shot 1	204,96		234,26		
Shot 2	205,94		234,22		
Shot 3			234,26		
Shot 4	205,59		234,22		
Shot 5	205,04		234,22		
Shot 6	205,31		234,22		280,39
Shot 7	205,08		234,38		280,35
Shot 8			234,22		280,20
Shot 9			234,22		
Shot 10			234,10		

**SAMPLE 3**

Row 1 (0°)					
Shot 1		228,98	234,26	238,95	
Shot 2		228,98	234,26	239,26	
Shot 3		228,98	234,26	238,91	
Shot 4		229,30	234,26	238,95	
Shot 5	210,12	228,98	234,30		286,84
Shot 6	210,86	228,71	234,26	237,93	286,76
Shot 7		228,67	233,95	238,13	286,99
Shot 8	210,08	228,67	233,91	238,20	
Shot 9			234,26	248,98	
Shot 10		228,91	234,22	248,67	
Row 2 (90°)					
Shot 1		229,26	234,26	239,69	
Shot 2		229,26	234,26	239,61	
Shot 3	211,37	229,26	234,30	239,65	
Shot 4	210,86	229,30	234,26	239,65	
Shot 5	210,90	229,30	234,22		287,19
Shot 6	211,09	228,91	234,22	237,70	286,99
Shot 7	211,09	228,98	233,91	238,24	286,80
Shot 8	210,90	228,98	233,87	238,16	286,84
Shot 9	210,86		234,26	248,36	286,88
Shot 10	210,55	228,91	234,30		286,41
Row 3 (180°)					
Shot 1		229,26	234,61		
Shot 2		229,30	234,57		
Shot 3	210,98	229,26	234,61		
Shot 4	210,66	229,30	234,57		
Shot 5	210,78	229,26	234,61		287,66
Shot 6	210,70	228,95	234,34		287,15
Shot 7	210,82	228,98	234,22	238,13	287,23
Shot 8	210,94	228,98	234,26	238,16	287,19
Shot 9	211,17	229,02	234,57		286,95
Shot 10	209,96	228,95	234,45		286,60